Kinetic Theory of Strongly Magnetized Plasmas

by

Louis Jose

A dissertation submitted in partial fulfillment
of the requirements for the degree of
Doctor of Philosophy
(Applied Physics)
in The University of Michigan
2023

Doctoral Committee:

Associate Professor Scott D. Baalrud, Chair
Associate Professor Carolyn C. Kuranz
Professor Mark Kushner
Associate Professor Ryan D. McBride
Professor Alexander G. R. Thomas

Louis Jose

louijos@umich.edu

ORCID iD: 0000-0002-8495-5095

To Amma and Nila

ACKNOWLEDGEMENTS

I sincerely thank Prof. Baalrud for his unwavering support, guidance, and patience throughout my Ph.D. journey. His guidance has enabled me to grow both as a researcher and a person. I am particularly grateful for his patience in explaining difficult concepts during our long research meetings, which sometimes went well beyond the scheduled hour. His ability to break down complex ideas and present them in a way I could understand has been a tremendous asset to my Ph.D. journey.

I also wish to thank my past and present group members, whose camaraderie made this experience enjoyable and rewarding. Lucas Beving, David Bernstein, Keith Vidal, Nathaniel Shaffer, Brett Scheiner, Shane Rightley, Julia Marshall, Marco Acciarri, James Welch, Julian Kinney, Lucas Babati, and Moises Enriquez provided many constructive feedbacks and inspiring ideas. I am fortunate to have had such an exceptional group of peers to work with.

I am grateful to my committee members, Prof. Kushner, Prof. Kuranz, Prof. Thomas, and Prof. McBride, for their insightful feedback and thoughtful suggestions that have contributed significantly to the quality of my research. I am deeply appreciative of their time and effort in reviewing my work.

I would like to extend my heartfelt thanks to the Applied Physics program for making my transfer to the University of Michigan from the University of Iowa an easy and seamless process. I am also thankful to the physics department at the University of Iowa for the resources, opportunities, and excellent physics courses provided during my first 3.5 years of graduate studies there.

I would also like to express my gratitude to the National Science Foundation (#PHY-1453736, #PHY-150018, #PHY-2205506), Department of Energy (#DE-SC0016159, #DE-SC0022202), Air Force Office of Scientific Research (#FA9550-16-1-0221) and Rackham (Rackham International Student Fellowship, 2021-2022) for providing the funding that has supported my research throughout my Ph.D. journey.

Finally, I thank my family and friends for their unwavering support and encouragement throughout my academic journey. Their belief in me has been a constant source of motivation and strength, and I am grateful for their love and support.

Thank you all for your invaluable contributions to my Ph.D. journey.

TABLE OF CONTENTS

LIST OF FIGURES

Figure

LIST OF TABLES

Table

ABSTRACT

Coulomb collisions in plasmas are typically modeled using the Boltzmann collision operator or its variants. These apply to weakly magnetized plasmas in which the typical gyroradius of particles significantly exceeds the Debye length. Conversely, O'Neil has developed a kinetic theory to treat plasmas that are so strongly magnetized that the typical gyroradius of particles is much smaller than the distance of closest approach in a binary collision. This dissertation presents a generalized collision operator that applies across the full range of magnetization strength and which asymptotes to the traditional Boltzmann collision operator in the weakly magnetized limit and O'Neil's theory in the extremely magnetized limit. The theory also spans the weak to strong Coulomb coupling regimes by incorporating the mean force kinetic theory concept. To demonstrate novel physics associated with strong magnetization, it is used to compute the friction force on a massive test charge and the ion-electron temperature relaxation rate.

Recent works studying weakly coupled plasmas have shown that strong magnetization leads to a transverse component of the friction force that is perpendicular to both the Lorentz force and velocity of the test charge, in addition to the stopping power component. Recent molecular dynamics simulations have also shown that strong Coulomb coupling, in addition to strong magnetization, gives rise to a third "gyrofriction" component of the friction force in the direction of the Lorentz force. The generalized kinetic theory captures these effects and agrees well with the molecu-

lar dynamics simulations over a broad range of Coulomb coupling and magnetization strengths. The transverse force strongly influences the average motion of a test charge by changing the gyroradius, and the gyrofriction force is found to slightly change the gyrofrequncy of the test charge resulting in a phase shift.

Strong magnetization is also shown to break a fundamental symmetry of independence of the collision rate on the sign of the charges of the interacting particles, commonly known as the "Barkas effect". It is found that the friction force changes dramatically depending on the sign of the interacting charges. The magnitude of the Bragg peak of the stopping power component for oppositely-charged particles decreases in magnitude compared with like-charged particles, and the perpendicular components increase in magnitude. Moreover, the difference between the two cases increases with increasing magnetization strength. On computing the electrical resistivity from the friction force, it is found that strong magnetization in conjunction with oppositely-charged interactions significantly decreases the parallel resistivity and increases the perpendicular resistivity.

Ion-electron temperature relaxation in strongly magnetized plasma is also found to exhibit novel properties. Strong magnetization is generally found to increase the temperature relaxation rate perpendicular to the magnetic field and to cause the temperatures parallel and perpendicular to the magnetic field to not relax at equal rates. This, in turn, causes a temperature anisotropy to develop during the equilibration. The temperature relaxation rate is also found to depend strongly on the sign of the charge of the interacting particles. It is found that the combination of oppositely charged interaction and strong magnetization causes the ion-electron parallel temperature relaxation rate to be significantly suppressed, scaling inversely proportional to the magnetic field strength.

CHAPTER I

Introduction

Plasma kinetic theory describes the evolution of plasmas that are displaced from equilibrium. The nonequilibrium state of a plasma may occur due to nonuniformity of the density, hydrodynamic velocity, or temperature throughout the plasma. These non-uniformities are smoothed out during the approach of the plasma to the equilibrium. This is done by the transport of mass, momentum, and energy from one part of the plasma to another. These processes are known as transport processes. The objective of kinetic theory is to explain the transport processes in terms of the properties of microscopic interactions between the particles.

The foundations of plasma kinetic theory are based on the Boltzmann equation of gases. Many assumptions used in the gas kinetic theory also carry over to the plasma kinetic theory. These assumptions include that the particles are weakly coupled in the sense that the average kinetic energy of the particles is much larger than the average potential energy: $\Gamma \ll 1$, where $\Gamma = (e^2/a)/(k_B T)$ is the Coulomb coupling parameter and $a = [3/(4\pi n)]^{1/3}$ is the Wigner-Seitz radius. However, there are many plasmas that are so dense or cold that the average potential energy exceeds the thermal energy. These plasmas are called strongly coupled plasmas and occur in many systems such as non-neutral plasmas [1], ultra-cold neutral plasmas [2], anti-matter traps [3], dusty plasmas [4, 5] and neutron star atmospheres [6].

In addition to weak coupling, traditional plasma kinetic theory assumes that the plasma is weakly magnetized in the sense that the gyroradius ($r_c = \sqrt{k_B T m}\, c/eB$) of particles is much larger than the Debye length ($\lambda_D = \sqrt{k_B T/4\pi e^2 n}$). This implies that $\beta = \lambda_D/r_c = \omega_c/\omega_p \ll 1$, where $\omega_c = eB/mc$ is the electron gyrofrequency and $\omega_p = \sqrt{4\pi e^2 n/m}$ is the electron plasma frequency. Most plasmas are weakly magnetized with the gyrofrequency smaller than the plasma frequency (or equivalently the gyroradius larger than the Debye length) ($\beta < 1$). In these plasmas, the magnetic field is not strong enough to influence the trajectories at the microscopic length scales at which Coulomb collisions occur (within a Debye length). However, there are many plasmas in which the magnetic field is so strong that it influences the trajectories of the particles during Coulomb collisions. These plasmas are called strongly magnetized ($\beta > 1$) and occur in many experiments, such as magnetic confinement fusion [7], nonneutral plasmas [1], ultracold neutral plasmas [8], magnetized dusty plasmas [9], pulsed power devices [10], electron cooling devices [11], trapped antimatter [3] and naturally occurring plasmas in planetary magnetospheres [12] and neutron star atmospheres [6]. Table 1.1 shows the magnetization strength for some of these systems.

Fundamentals of transport in the regime of weak coupling and weak magnetization have long been studied using traditional plasma kinetic theories. However, plasmas also exist in regimes of strong Coulomb coupling and strong magnetization. Such strongly magnetized and/or strongly coupled plasmas behave fundamentally in different ways that are not well understood. Developing a theory to understand the transport in these regimes is of interest from a fundamental point of view in addition to having applications in the above-mentioned experiments.

In this dissertation, a generalized plasma kinetic theory that applies across the Coulomb coupling - magnetization phase space, spanning from small to large values of both Γ and β is developed. The kinetic theory is

System	n_e (cm^{-3})	$k_B T_e$ (eV)	B (T)	Γ_e	β_e	Ref.
Ultracold neutral plasmas	10^7	10^{-3}	0.01	0.05	10	[8]
Antimatter traps	10^8	10^{-3}	1	0.1	310	[3]
Magnetized dusty plasma	10^{10}	3	4	10^{-4}	125	[9]
Neutron star atmospheres	10^{24}	100	10^8	0.2	300	[6]
Magnetic confinement fusion	10^{14}	10^4	5	10^{-6}	1.5	[7]

Table 1.1: A sample of systems in which electrons are strongly magnetized.

used to compute friction and temperature relaxation rates spanning these regimes.

1.1 Transport regimes

Regimes that characterize the influence of magnetization and coupling strength on transport can be identified by comparing the gyroradius ($r_c = \sqrt{k_B T/m}/\omega_c$) with the Debye length ($\lambda_D = \sqrt{k_B T/4\pi e^2 n}$), Landau length times $\sqrt{2}$ ($r_L = \sqrt{2}e^2/k_B T$), Coulomb collision mean free path ($\lambda_{\rm col}$) [13] and average interparticle spacing (a). The four possible transport regimes are shown in Fig. 1.1. Each of the four transport regimes are accessible when the plasma is weakly coupled. However, at strong coupling the parameter space collapse into two regimes since the Coulomb collision mean free path becomes shorter than both the Debye length and Landau length. The four regimes are classified as

1. Unmagnetized ($r_c > \lambda_{col}$): The plasma is considered unmagnetized when the gyroradius is larger than the Coulomb collision mean free path. In this regime gyration of particles by the magnetic field does not happen due to Coulomb collisions with other particles. The collisional transport in this regime is not significantly influenced by the magnetic field.

2. Weakly Magnetized ($\max(\lambda_D, a) < r_c < \lambda_{col}$): In this regime the gyroradius is smaller than the Coulomb collision mean free path but larger than the Debye

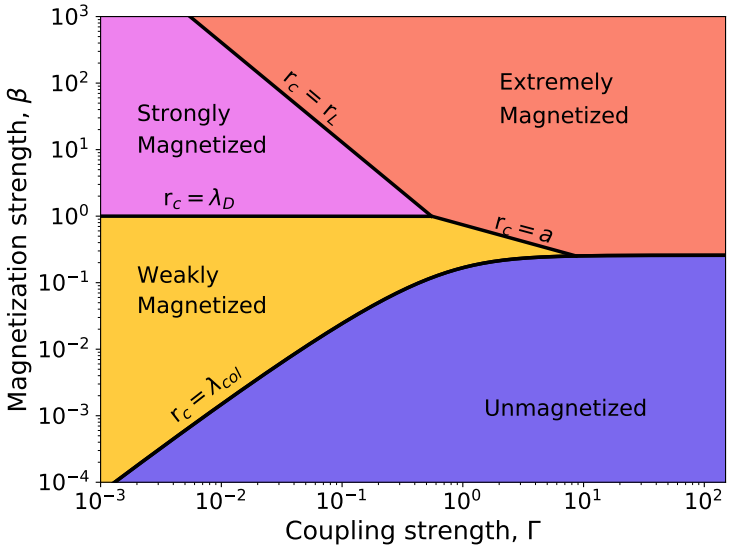

Figure 1.1: Coupling-magnetization phase space indicating the transport regimes.

length or inter particle spacing. The magnetic field influences the transport in this regime because the distribution functions are more easily distorted along the field lines than across. However, the gyromotion does not influence particles at the collision scale.

3. Strongly Magnetized ($r_L < r_c < \lambda_D$): Plasma is considered strongly magnetized when the gyroradius is smaller than the Debye length but larger than the distance of closest approach. In this regime, the gyromotion happens at the scale at which collisions occur. Here, the magnetic field influences the collisions at the microscopic scale.

4. Extremely Magnetized ($r_c < \min(r_L, a, \lambda_{col})$): In this regime gyroradius is smaller than the closest interaction distance between the particles. Particles in this regime move effectively in one dimension and have 180° collisions with other particles on the same field line.

1.2 Experiments

There are many examples of laboratory and naturally occurring plasmas that are strongly magnetized. Here, we describe two experiments that have served as the main motivation for our theoretical development.

1.2.1 Magnetized ultracold neutral plasmas

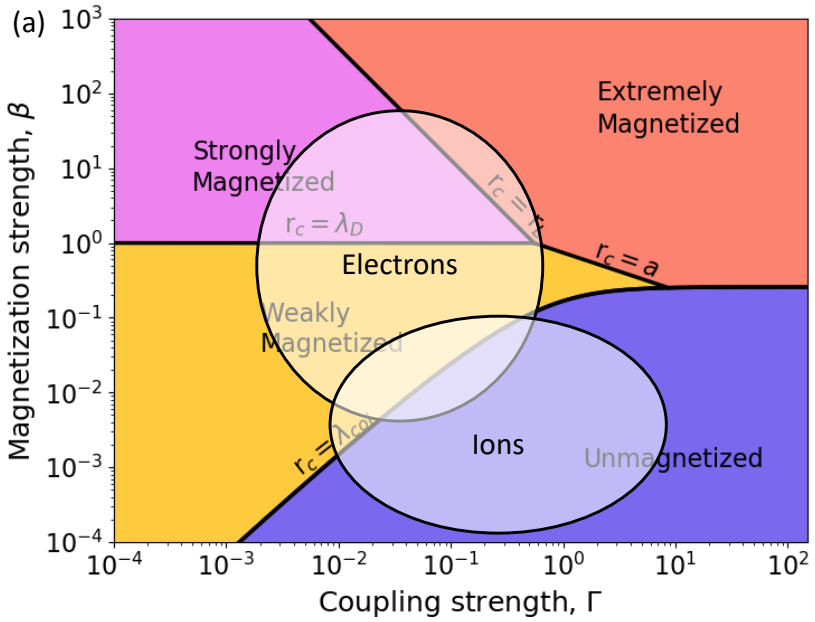

Figure 1.2: Regions corresponding to values of ions and electrons in magnetized ultracold neutral plasma experiments in the $\Gamma - \beta$ phase space

Ultracold neutral plasma experiments are well-diagnosed tabletop-scale experiments. These plasmas are created by laser-cooling neutral atoms to temperatures near absolute zero and then photoionizing them [14]. The resulting system of cold ions and electrons forms a finite-size quasi-neutral two-component plasma. The plasma expands freely with electrons confined by the positive charge of the inertially-localized ions. If not confined by an external potential, the ions expand freely and are limited only by their mass. Owing to the high ionization achieved by photoionization, the plasma is relatively free of neutral-species contaminants.

The ions in these experiments are very cold (~ 1 K) and have a density of approximately $10^{13} - 10^{15}$ m^{-3}, making them strongly coupled with the coupling strength $\Gamma < 10$. The electron temperature in ultracold neutral plasma experiments is controlled by tuning the wavelength of the photoionizing laser. In these experiments, the electron temperature is tuned from 1-1000 K. This controllability of the electron temperature is used to study the temperature dependence of many transport properties and other processes, such as three-body recombination. In a typical experiment, electrons are weakly to moderately coupled with a coupling strength of $\Gamma < 0.5$.

An advantage of ultra cold neutral plasmas is that they access strongly coupled regime in a well diagnosed table-top scale apparatus. Other strongly coupled systems, such as inertial confinement fusion plasma, warm dense matter, and white dwarf stars, are very dense. Thus, the dynamical time scale ($\sim 1/\omega_{pi}$) in these systems is on the order of 100 fs, making the measurement of fundamental dynamical properties difficult. However, ultracold neutral plasmas achieve strong coupling via very low temperatures. The low density of these systems makes the dynamical timescale on the order of 100 ns, making fundamental studies more tractable. This allows ultracold neutral plasma experiments to be a well-diagnosed platform for studying strongly coupled plasmas and is an excellent tool to benchmark theories [15].

Over the last two decades, the ability of the ultracold neutral plasma experiments to achieve the strongly correlated state has been a valuable tool for investigating the fundamental properties of strongly coupled systems. They have led to the discovery and further explanation of many physical processes associated with the strong coupling, including disorder-induced heating [16, 17], Barkas effect [18, 19], three-body recombination [20, 21], modification of collisional transport [15, 22, 23], etc.

In recent years, several ultracold neutral plasmas have been magnetized [8, 24, 25, 26]. With a magnetic field strength of a few thousand gauss, the electrons in these experiments reach the strongly magnetized transport regime. Ions, being more massive

than electrons, are not strongly magnetized in these experiments. Figure 1.2 shows the coupling strength and magnetization values of electrons and ions in the coupling magnetization phase space. These experiments are in a unique regime where the ions are strongly coupled and the electrons are strongly magnetized. Ongoing experiments measure plasma expansion, electrical conductivity, temperature evolution, and three-body recombination. Theoretical models using the traditional plasma kinetic theory for weakly magnetized plasmas have failed to capture the plasma expansion in recent magnetized experiments [26]. The generalized kinetic theory developed in this thesis can describe the novel transport processes in these strongly magnetized and strongly coupled plasmas and provide a candidate theory that may be applied to model these experiments in the future.

1.2.2 Antihydrogen Laser Physics Apparatus (ALPHA)

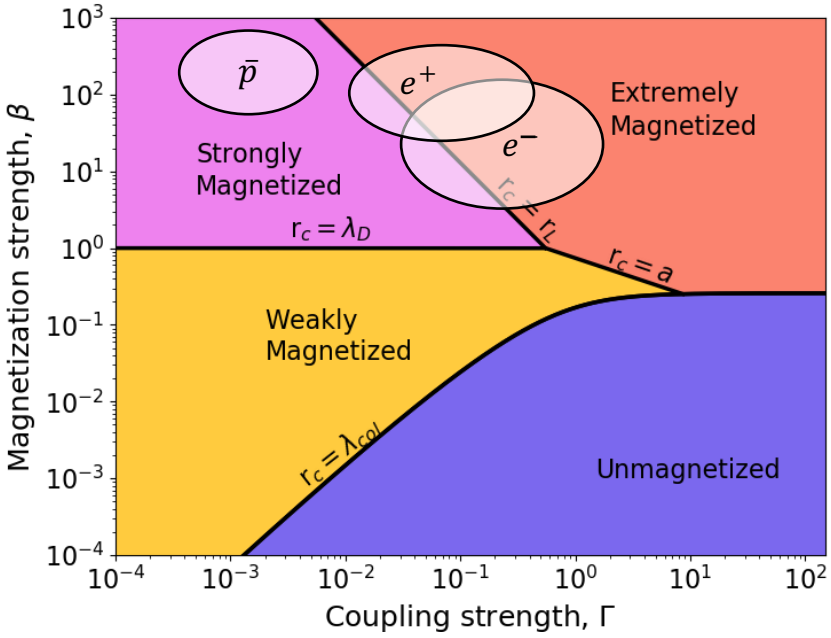

Figure 1.3: Regions corresponding to values of antiprotons ($\bar{p}$), positrons (e^+) and electrons (e^-) of ALPHA experiment in the $\Gamma - \beta$ phase space

The Nobel Prize in 1933 was awarded to Paul Dirac for the formulation of what

came to be known as the Dirac equation. The Dirac equation combines the quantum theory and the special theory of relativity, two contributions of Einstein. The Dirac equation predicted the existence of antimatter, which is a corresponding entity to ordinary matter with the same mass but with an opposite charge and spin. For example, the antiparticle of an electron is an anti-electron, called a positron. It is identical in every way to an electron but with a positive electric charge. Similarly, for a proton, there is an antiproton having a negative charge. Shortly after Dirac's prediction, the existence of antiparticles was validated experimentally. Fundamental antimatter particles can be combined to form more complex antimatter, like how ordinary particles combine to form matter.

Theories postulate that antimatter should obey the same physical laws as ordinary matter. This, along with the current understanding of the universe, suggests that the amount of antimatter in the universe should be equal to that of ordinary matter; however, to the best of our knowledge, the universe is primarily composed of matter. Antimatter is only observed in laboratory and exotic natural processes, such as cosmic rays and radiation decays. This matter-antimatter asymmetry remains one of the great mysteries in physics. The ALPHA experiment at CERN investigates this asymmetry by precisely comparing antihydrogen with hydrogen. An essential aspect of this research is to maximize the production of antihydrogen to decrease the statistical uncertainty in the measurement of its properties [27, 28, 29, 30, 31]. In these experiments, antihydrogen is produced by mixing antiprotons with positrons in a Penning-Malmberg trap. The charged antiproton and positron can be well contained in the trap. However, the antihydrogen is not well contained in the trap because it is charge neutral. The trap depth for the synthesized antihydrogen is only 0.5 K in temperature units. Thus, to maximize the efficiency of antihydrogen production, the positrons and antiprotons are first cooled before combining [32].

The positrons are cooled in the trap to cryogenic temperatures by cyclotron cool-

ing. This decreases the perpendicular temperature and produces an anisotropy, which later relaxes by Coulomb collisions. Since antiprotons are massive, the cyclotron cooling method does not reduce their temperature significantly. Instead, the antiprotons are sympathetically cooled by collisions with cool electrons. Once the antiprotons are cooled, the electrons are removed from the trap, and the antiprotons are mixed with cool positrons for antihydrogen synthesis [28, 29, 30, 33].

Figure 1.3 shows the coupling strength and magnetization values of the electrons, antiprotons, and positrons. All particles are strongly magnetized, and the electrons and positrons are moderately coupled. The generalized kinetic theory developed in this thesis can be used to model this exotic antimatter plasma. A few questions that can be answered using the generalized theory, in relation to the ALPHA experiment, include the temperature anisotropy relaxation rate of electrons and positrons, the temperature relaxation rate of antiprotons cooling down on electrons and the rate at which antiprotons and positrons reach an equilibrium temperature before they recombine to form the antihydrogen.

1.3 Previous theoretical approaches

1.3.1 Boltzmann equation

A common approach to the plasma kinetic theory is based on the Boltzmann equation:

$$\partial_t f + \mathbf{v} \cdot \partial_{\mathbf{x}} f + \frac{e}{m}[\mathbf{E} + \mathbf{v}/c \times \mathbf{B}] \cdot \partial_{\mathbf{v}} f = \mathcal{C}, \tag{1.1}$$

where the interactions between the particles occurring at microscopic scales are described by the collision operator ($\mathcal{C}$). The collision operator is

$$\mathcal{C} = \int d^3\mathbf{v}' \int \sigma d\Omega \, u \left[f(\mathbf{x}, \hat{\mathbf{v}}, t) g(\mathbf{x}, \hat{\mathbf{v}}', t) - f(\mathbf{x}, \mathbf{v}, t) g(\mathbf{x}, \mathbf{v}', t) \right]. \tag{1.2}$$

Here, σ is the differential scattering cross section, $d\Omega = \sin\theta d\theta d\phi$ is the solid angle, f and g are the distribution functions, the velocities with hat ($\hat{}$) on them are the postcollision velocities and $\mathbf{u} = \mathbf{v} - \mathbf{v}'$ is the relative velocity of the colliding particles. The theory assumes that collisions are isolated, uncorrelated events in which two particles start infinitely far apart before the collision (precollision state) and end up infinitely far apart after the collision (postcollision state). The interaction between the particles is modeled using the bare Coulomb potential, and the particles exchange momentum and energy during a collision event. The differential scattering cross section is given by the Rutherford scattering formula [34].

When calculating the transport properties using the Boltzmann equation, the resulting integrals confront a logarithmic divergence at large impact parameters (infrared divergence). This is because of the assumption that the particles interact via the bare Coulomb potential, and that the collisions are well-separated binary collision events. This logarithmic divergence of the theory is resolved using the physical argument of Debye screening to cut off the maximum impact parameter at the Debye length.

Application of the traditional Boltzmann kinetic theory to account for the effects of the magnetic field assumes that the gyroradius of the interacting particles is significantly larger than the Debye length. This is equivalent to saying that the corrections to particle trajectories due to the Lorentz force during the collision events are negligible. Thus, the Rutherford scattering formula is used for the differential scattering cross section. Consequently, the magnetic field appears only on the left-hand side of the Boltzmann equation, and the collision operator is independent of the magnetic field. This limits the theory to the unmagnetized and weakly magnetized transport regimes.

1.3.2 O'Neil's equation

O'Neil has developed a Boltzmann-like kinetic theory [35] for the opposite limit of extreme magnetization. In this theory, the collisions between particles of a pure-electron plasma are considered, and the gyroradius of the particles is assumed to be much smaller than the Landau length. The collision operator is

$$\mathcal{C} = \int d^3\mathbf{v}' \int \rho d\rho d\theta \, |\mathbf{u} \cdot \hat{\mathbf{z}}| \left[f(\mathbf{x}, \hat{\mathbf{v}}, t) g(\mathbf{x}, \hat{\mathbf{v}}', t) - f(\mathbf{x}, \mathbf{v}, t) g(\mathbf{x}, \mathbf{v}', t) \right], \tag{1.3}$$

where ρ is the transverse separation between the electrons at the beginning of the collision.

The collision operator is obtained from a closure of the BBGKY hierarchy [34] specific to extremely magnetized pure-electron plasmas. Considering only the collisions between particles of the same species simplifies the equations of motion by decoupling the center of mass and the relative motion. This simplification, along with the adiabatic invariance of the perpendicular kinetic energy in the limit of extreme magnetization, was used to simplify the first-order BBGKY equation to obtain the collision operator for extremely magnetized plasma. The utility of the collision operator was later shown by calculating the temperature anisotropy relaxation rate of a pure electron plasma and successfully verifying the results with experiments [36].

1.3.3 Lenard-Balescu equation

The Boltzmann-type collision operator is a binary collision theory, which misses the overall collective behavior of the plasma. The failure of the theory to capture collective behavior leads to an infrared divergence. In contrast, Lenard-Balescu [37, 38] theory accounts for the linear response of the plasma to a perturbation, capturing the collective behavior. This features the use of a frequency-dependent dielectric response function to account for various waves in the plasma. This theory successfully

captures the dynamic screening of the plasma, which is absent in the Boltzmann-type collision operators that model the interaction between particles via a static (Coulomb) potential. By capturing the physics of collective behavior, the Debye shielding comes naturally in theory, and thus, it does not diverge at large impact parameters.

Since the Lenard-Balescu theory only accounts for the linear response of the plasma to a perturbation, it fails to capture the close nonlinear interactions. This limits the theory to small-angle scattering at large impact parameters. The failure of the theory to capture the large-angle scatterings leads to the divergence of the theory at small impact parameters (ultraviolet divergence). This is fixed by introducing an ad hoc cut-off at the distance of the closest approach.

The Lenard-Balescu formalism for weakly magnetized plasmas was generalized to treat strong magnetization by Rostoker [39]. Similar to the Lenard-Balescu theory, this theory successfully captures the collective behavior of the magnetized plasma, including the dynamic screening. However, the weak interaction approximation of the theory leads to divergence at short distances. Thus, this approach is not applicable to the extremely magnetized plasmas where the gyroradius is smaller than the distance of the closest approach.

1.3.4 Fokker-Planck equation

Rosenbluth, MacDonald, and Judd used the Fokker-Planck formalism initially developed for the molecular gases to derive a kinetic equation for the plasmas [40]. This result is commonly referred to as the Rosenbluth equation. The classical Fokker-Planck equation has two terms: friction and diffusion coefficients. For a weakly magnetized plasma, they can be expressed in terms of Rosenbluth potentials.

Using the small scattering angle approximation, the Rosenbluth equation can also be obtained from the Boltzmann equation. It is obtained by Taylor-expanding the postcollision distribution functions for a small change in velocities and maintaining

only the terms up to the second order. The evaluation of the Boltzmann kinetic equation involves the computation of the distribution functions at postcollision velocities in the collision operator. The Fokker-Planck equation has an advantage over the Boltzmann equation, as it does not involve any postcollision velocities in the distribution functions. However, due to the small scattering angle approximation, the Fokker-Planck equation is limited to weakly coupled plasmas.

The extension of the Fokker-Planck equation to strongly magnetized plasma involves the calculation of the friction and diffusion coefficients for strongly magnetized Coulomb collisions. Different approaches used to obtain magnetized Fokker-Planck coefficients include perturbative treatments of binary collisions [41, 42, 43], guiding center approximations [44, 45], electric field fluctuations and dielectric response function [46], velocity space current [47, 48] and Green-Kubo relations [49].

Like the unmagnetized case, the magnetized Fokker–Planck equations only account for the small angle scattering events between the colliding particles in the plasma. These equations inherently assume that the momentum exchanged during a collision is small. Because large momentum transfer collisions are frequent when the gyroradius is shorter than the distance of the closest approach, this method is expected to apply only in regions 1–3.

An alternative approach is to circumvent the collision operator and directly model the macroscopic transport coefficients from the properties of particle trajectories. Previous work along these lines has utilized perturbation theory [50, 51, 52, 53], integration along unperturbed orbits [45, 54], linear-response theory [55, 56], force correlation methods [57, 58], and other perturbation methods [59] to determine the momentum and energy exchanged in a collision and to directly model the transport coefficients.

1.3.5 Mean force kinetic equation

Each approach mentioned above addresses a portion of the strong magnetization parameter space at weak coupling conditions ($\Gamma \ll 1$) but does not address strong coupling. A vital characteristic of collisions in the strongly coupled plasmas is that the large angle scattering events become prominent [60]. Thus, the Fokker-Planck and Lenard-Balescu approaches, which inherently assume small momentum transfer in collisions, are unsuitable for this regime. Theories that address transport in strongly coupled regimes use Boltzmann theory, but instead of modeling binary collisions via the bare Coulomb potential, use an effective interaction potential [61, 62, 63, 64, 65]. The effective potential introduces plasma screening and thus naturally avoids the infrared divergence of the traditional Boltzmann theory.

Mean force kinetic theory is an effective kinetic potential theory developed by Baalrud and Daligault [63, 64]. It is the mean force acting on a particle obtained while keeping it and another particle at fixed positions and averaging over all equilibrium configurations of the remaining particles. The potential of mean force asymptotes to the well-known Debye-Hückel potential when the plasma is weakly coupled; however, it also includes many-body correlation effects beyond Debye screening at higher Coulomb coupling [64].

The potential of mean force was initially introduced as an effective interaction potential to model binary collisions. [63]. However, a later rigorous work using a new expansion parameter for BBGKY hierarchy that measures the deviation of correlations from their equilibrium values, instead of using the strength of correlations as used in the traditional Boltzmann theory, has shown that the two particles interact via a mean force [64]. This theory has been extensively tested for Coulomb interactions in fully ionized unmagnetized plasmas by comparison with MD simulations [18, 60, 63, 66, 67, 68] and experiments [15, 63] for a variety of transport coefficients. These tests have shown that the theory is accurate when $\Gamma \leq 20$. At

larger coupling strength, the plasma transitions to a liquid-like regime [69], where assumptions made in the mean force kinetic theory do not apply.

1.4 Outline of this thesis

The goal of the thesis is to develop a generalized Boltzmann kinetic theory that is applicable for the whole coupling-magnetization phase space and use it to obtain macroscopic transport properties. The macroscopic transport properties computed in this thesis are the friction and temperature relaxation rate. The thesis is divided into five projects.

1.4.1 Derivation of a generalized Boltzmann collision operator

In this project a generalized Boltzmann collision operator that is applicable to all the transport regimes of the plasma is derived. The traditional Boltzmann collision operator and O'Neil's Boltzmann-like collision operator for the extremely magnetized plasma are obtained from the generalized collision operator in the limits of no magnetic field and high magnetic field, respectively. The results have been published in Ref. [70] and are the topic of chapter II.

1.4.2 Friction in strongly magnetized plasmas

The generalized collision operator is applied to compute the friction force acting on a massive test charge moving through a weakly coupled magnetized one-component plasma. It is found that the strong magnetization leads to a transverse component of the friction force that is perpendicular to both the Lorentz force and velocity of the test charge, in addition to the stopping power component aligned antiparallel to the velocity. These predictions are in agreement with a previous linear response calculation. The work also extends the computation of the friction force to the extremely

magnetized transport regime, which is not attainable using the linear response theory. The results have been published in Ref. [70] and are the topic of chapter III.

1.4.3 Friction in strongly coupled strongly magnetized plasmas

In this project, the friction force calculation on a test charge is extended to the strongly coupled strongly magnetized regime. It is found that strong coupling along with strong magnetization gives rise to a "gyro" component of friction force along the direction of the Lorentz force, in addition to the stopping power and the transverse force. The theory results are in good agreement with the results from previous molecular dynamics (MD) simulations. Computing the average motion of the test charge through the background plasma, the transverse force is found to strongly influence the trajectory by changing the gyroradius and the gyrofriction force is found to slightly change the gyrofrequency of the test charge resulting in a phase shift. The results have been published in Ref. [71] and are the topic of chapter IV.

1.4.4 Barkas effect in strongly magnetized plasmas

Conventional plasma theories obey a fundamental symmetry that the collision rate is independent of the sign of the charge of interacting particles. For example, in the Boltzmann-based models this stems from the fact that the Rutherford cross section depends only on the square of the charges. Thus, the transport coefficients remain the same if electron-ion interactions are modeled as positron-ion interactions. This project shows that this symmetry is broken when the plasma is strongly magnetized. This symmetry-breaking effect is called the Barkas effect. When extending the calculation of the friction force on a test ion to oppositely charged background particles (electrons), it is found that the friction force changes dramatically when compared to like-charged interactions. The stopping power component for oppositely charged particles decreases in magnitude compared with like-charged particles, and the per-

pendicular components increase in magnitude. The electrical resistivity is calculated from the friction force, where it is found that strong magnetization in conjunction with oppositely charged interactions significantly decreases the parallel resistivity and increases the perpendicular resistivity. The results have been published in Ref. [72] and are the topic of chapter V.

1.4.5 Ion-electron temperature relaxation rate

This project calculates the ion-electron temperature relaxation rate of strongly magnetized plasmas. Strong magnetization is generally found to increase the temperature relaxation rate perpendicular to the magnetic field, and to cause the temperatures parallel and perpendicular to the magnetic field to not relax at equal rates. This, in turn, causes a temperature anisotropy to develop during the equilibration. Strong magnetization is also shown to cause a large Barkas effect in the energy relaxation process. It is found that the combination of oppositely charged interaction and strong magnetization causes the ion-electron parallel temperature relaxation rate to be significantly suppressed, scaling inversely proportional to the magnetic field strength. This work is presented in chapter VI.

CHAPTER II

Generalized Boltzmann Collision Operator

Derivations of the Boltzmann equation begin from a general description of the dynamics of N interacting particles, but then apply a series of approximations to focus on average quantities of interest, and to make the problem tractable by invoking properties of the dilute gas (or plasma) limit. Here, we follow a traditional derivation due to Grad [73, 74, 75], insofar as it applies to arbitrary magnetization. This includes defining reduced distribution functions, and making use of the dilute limit to justify binary collisions, the molecular chaos approximation [73], and local collisions that happen at microscopic space and time scales. The departure from the traditional derivation comes about by not making approximations of a certain geometry for the collision volume that are justified only in the absence of strong magnetization, and by accounting for the Lorentz force when computing the binary collision dynamics inside that volume. This leads to a more general, but more computationally intensive, kinetic equation. It reduces to either the traditional result or O'Neil's result in the appropriate limits.

2.1 Derivation of a generalized collision operator

Derivation of the Boltzmann equation begins from Liouville's equation [34], which describes the phase space evolution of the N-particle distribution function ($f^{(N)}(\mathbf{r}_1, \mathbf{r}_2$

$\cdots \mathbf{r}_N, \mathbf{v}_1, \mathbf{v}_2 \cdots \mathbf{v}_N, t))$. However, this description is a complex computational problem because of the large number of degrees of freedom brought by the huge number of particles in the system. As a way to reduce the computational complexity of the problem and to focus on physical processes of interest, reduced distributions are defined by integrating a subset of the degrees of freedom. This results in the BBGKY hierarchy [34]. These equations are not closed because the evolution equation for the n particle distribution $(f^{(n)}(\mathbf{r}_1, \mathbf{r}_2 \cdots \mathbf{r}_n, \mathbf{v}_1, \mathbf{v}_2 \cdots \mathbf{v}_n, t))$ contains the $n+1$ particle distribution.

A kinetic equation describes the evolution of the one-particle distribution function $f^{(1)}$. Obtaining a closed form expression requires an approximation for $f^{(2)}$, which is usually obtained from an approximation that closes the BBGKY hierarchy. The Boltzmann equation is a prototypical example. It can be derived by solving for $f^{(2)}$ from the $n = 2$ equation of the hierarchy by dropping triplet correlations via the approximation $f^{(3)} = 0$. Although this method is accurate for particles interacting via short-range potentials, such as neutral gases, it leads to an infrared divergence in plasmas due to the long-range nature of the Coulomb interaction [34]. This is usually corrected by introducing an ad hoc cutoff to the impact parameter at the Debye length to model Debye screening. Recent work [64] using a new closure of the BBGKY hierarchy has shown that expanding about the deviations of correlations from their equilibrium values,

$$\Delta f^{(3)} = f^{(3)} - f_o^{(3)} f^{(2)} / f_o^{(2)} \tag{2.1}$$

rather than in terms of the strength of correlations, $f^{(3)}$, ensures that the exact equilibrium properties are maintained at all orders of the hierarchy, including screening. Here, f_o is the equilibrium distribution function. This expansion shows that binary collisions occur via the potential of mean force [60, 63], rather than the bare Coulomb

potential. The potential of mean force asymptotes to the Debye-Hückel potential in the weakly coupled limit

$$\phi(r) = \frac{e_1 e_2}{r} e^{-r/\lambda_D}. \tag{2.2}$$

Here, $r = |\mathbf{r}| = |\mathbf{r}_1 - \mathbf{r}_2|$ is the distance between the particles and e_1, e_2 are the charges of the particles. We make use of this new closure, but otherwise follow Grad's [73, 74, 75] derivation of the Boltzmann equation.

In this approach, the coordinate space is divided into a microscopic volume where the collisions occur (V_σ) and an outside region where no collisions occur. This motivates the definition of truncated reduced distribution functions according to this scale separation

$$f_\sigma^{(n)}(\mathbf{r}_1, \mathbf{v}_1 \cdots \mathbf{r}_n, \mathbf{v}_n, t) = \frac{N!}{(N-n)!} \int\limits_{\widetilde{V}_\sigma} d\mathbf{\Gamma}^{(N-n)} f^{(N)}(\mathbf{r}_1, \mathbf{v}_1 \cdots \mathbf{r}_N, \mathbf{v}_N, t), \tag{2.3}$$

where $d\mathbf{\Gamma}^{(N-n)} = d^3\mathbf{r}_{n+1} d^3\mathbf{v}_{n+1} \cdots d^3\mathbf{r}_N d^3\mathbf{v}_N$ and $\widetilde{V}_\sigma$ indicates that the collision volume is excluded in the spatial integral. Integrating the Liouville's equation, the first order term of the BBGKY hierarchy in terms of the truncated distribution function is [64]

$$\left[\partial_t + \mathbf{v}_1 \cdot \partial_{\mathbf{r}_1} + \frac{e_1}{m_1}\left(\frac{\mathbf{v}}{c} \times \mathbf{B} + \mathbf{E}\right) \cdot \partial_{\mathbf{v}_1}\right] f_\sigma^{(1)} = \int d^3\mathbf{v}_2 \oint\limits_S d\mathbf{s} \cdot (\mathbf{v}_1 - \mathbf{v}_2)\, f_\sigma^{(2)} - \int\limits_{\widetilde{V}_\sigma} d^3\mathbf{r}_2 \int d^3\mathbf{v}_2 \frac{e_1\, e_2\, \mathbf{r}}{m_1 r^3} \cdot \partial_{\mathbf{v}_1} \Delta f^{(2)}. \tag{2.4}$$

Here, the surface integral is defined by the small region of space in which the two particles interact (collision volume). As described in Ref. [64], the term corresponding to an integral of $\Delta f^{(2)}$ over the collision volume is small in comparison with the surface term because the excluded volume (i.e., collision volume) is defined as the scale over which $\Delta f^{(2)}$ is small. This scale is determined by the screening length and is directly

related to Eq. (2.2) at equilibrium [64]. Furthermore, $f_\sigma^{(1)}$ can be equated with $f^{(1)}$ because the single particle distribution is uniform over this short spatial scale. With these approximations, collision operator can be written as

$$\mathcal{C} = \int d^3\mathbf{v}_2 \oint_S ds\, \mathbf{u}\cdot\hat{\mathbf{s}}\, f_\sigma^{(2)}(\mathbf{r}_1, \mathbf{r}_2, \mathbf{v}_1, \mathbf{v}_2, t), \tag{2.5}$$

where $\mathbf{u} = \mathbf{v}_1 - \mathbf{v}_2$ is relative velocity between the colliding particles. In the small collision volume limit, the truncated distribution function is the observable particle distribution function ($f_\sigma^{(2)}(\mathbf{r}_1, \mathbf{r}_2, \mathbf{v}_1, \mathbf{v}_2, t) = f^{(2)}(\mathbf{r}_1, \mathbf{r}_2, \mathbf{v}_1, \mathbf{v}_2, t)$). Here, ds is the infinitesimal area on the surface of the collision volume and $\hat{\mathbf{s}}$ is the unit normal of the area element. The collision volume can be visualized in the relative frame with the coordinate system fixed to particle 2 with particle 1 entering the collision volume as shown in Fig. 2.1.

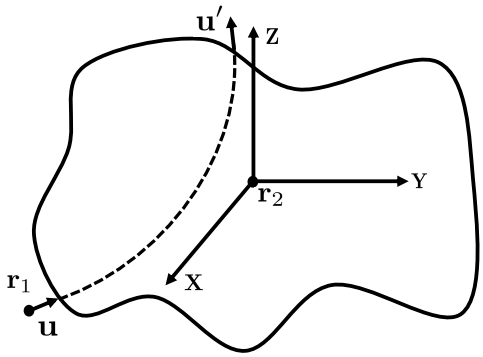

Figure 2.1: Illustration of a collision volume surrounding particle 2 ($\mathbf{r}_2$) during an interaction with particle 1 ($\mathbf{r}_1$).

Depending on the sign of $\mathbf{u}\cdot\hat{\mathbf{s}}$, the surface integral is split into two terms, representing contributions from two surfaces $S_+(\mathbf{u}\cdot\hat{\mathbf{s}} > 0)$ and $S_-(\mathbf{u}\cdot\hat{\mathbf{s}} < 0)$. Points on S_+ correspond to particles moving away from each other (postcollision state) and points on S_- correspond to particles moving towards each other (precollision state). Assuming binary collisions occurring via the mean force within the interaction volume, the second order BBGKY equation with the $\Delta f^{(3)} = 0$ truncation provides a solution

whereby $f^{(2)}(\mathbf{r}_1, \mathbf{r}_2, \mathbf{v}_1, \mathbf{v}_2, t)$ is a constant along the two particle trajectory. Thus, for points on the S_+ surface, $f^{(2)}$ can be replaced with the post collision coordinates: $f^{(2)}(\mathbf{r}_1, \mathbf{r}_2, \mathbf{v}_1, \mathbf{v}_2, t) \to f^{(2)}(\mathbf{r}_1', \mathbf{r}_2', \mathbf{v}_1', \mathbf{v}_2', t)$, where the variables with prime ($'$) represent postcollision states [73, 74]. On making these changes, the collision operator becomes

$$\begin{aligned} \mathcal{C} = & \int d^3\mathbf{v}_2 \int_{S+} ds\, |\mathbf{u}\cdot\hat{\mathbf{s}}| f^{(2)}(\mathbf{r}_1', \mathbf{r}_2', \mathbf{v}_1', \mathbf{v}_2', t) \\ & - \int d^3\mathbf{v}_2 \int_{S-} ds\, |\mathbf{u}\cdot\hat{\mathbf{s}}| f^{(2)}(\mathbf{r}_1, \mathbf{r}_2, \mathbf{v}_1, \mathbf{v}_2, t). \end{aligned} \tag{2.6}$$

In order to get an explicit form of the collision operator, the integrals can be written over the same integration range by the change of variable: $\hat{\mathbf{s}} \to -\hat{\mathbf{s}}$ in the first integral, changing S_+ to S_-. Further, we make the assumption of molecular chaos (*Stosszahlansatz*): $f^{(2)}(\mathbf{r}_1, \mathbf{r}_2, \mathbf{v}_1, \mathbf{v}_2, t) = f^{(1)}(\mathbf{r}_1, \mathbf{v}_1, t) f^{(1)}(\mathbf{r}_2, \mathbf{v}_2, t)$, where $f^{(1)}(\mathbf{r}, \mathbf{v}, t)$ is the one particle distribution function [1]. We also assume that the collision volume is small. This is justified by the short timescale of the collision compared to the larger timescale of evolution of $f^{(1)}(\mathbf{r}, \mathbf{v}, t)$. In this limit of a local collision $\mathbf{r}_1'$, $\mathbf{r}_2'$ and $\mathbf{r}_2$ can be approximated by $\mathbf{r}_1$ [73, 74]. On making these approximations, a generalized collision operator is obtained

$$\mathcal{C} = \int d^3\mathbf{v}_2 \int_{S-} ds\, |\mathbf{u}\cdot\hat{\mathbf{s}}| (f_1' f_2' - f_1 f_2), \tag{2.7}$$

[1] Considering collisions in strongly magnetized one-component plasmas, Dubin has argued that strong magnetization causes particles to recollide multiple times [54]. Such multi-body interactions violate the molecular chaos approximation. Further research will be required to understand the role of recollisions in the friction force problem considered in this chapter, or to adapt the generalized collision operator to incorporate recollision dynamics.

in which the following abbreviated notations have been applied

$$f_1' \equiv f^{(1)}(\mathbf{r}_1, \mathbf{v}_1', t), \qquad f_2' \equiv f^{(1)}(\mathbf{r}_1, \mathbf{v}_2', t),$$
$$f_1 \equiv f^{(1)}(\mathbf{r}_1, \mathbf{v}_1, t), \qquad f_2 \equiv f^{(1)}(\mathbf{r}_1, \mathbf{v}_2, t).$$

Equation (2.7) is the expression for the generalized collision operator. This result has been obtained in many prior works during the path to derive the traditional Boltzmann equation. The novelty here is to evaluate Eq. (2.7) directly, rather than proceed to simplify it by invoking arguments associated with either the weak or extreme magnetization limits. In order to evaluate this expression, the post collision velocities ($\mathbf{v}_1'$ and $\mathbf{v}_2'$) need to be evaluated. This involves solving the two body dynamics of the colliding particles inside the collision volume for the initial velocities ($\mathbf{v}_1$ and $\mathbf{v}_2$).

Equation (2.7) is a 5-D integral: 3-D velocity space volume and a 2-D surface in the coordinate space. The surface integral encloses a small region where collisions occur that is determined by the range of the potential of mean force. The integral can be viewed as summing over all possible configurations in which particle 1 enters the collision volume and interacts with particle 2, weighted by the postcollision and the precollision velocity distributions. The surface integral counts all the possible orientations in which the particle enters the collision volume and the velocity integral counts all the possible velocities of particle 2. Limiting the surface integral to the surface S_- makes sure only the precollision states are counted.

For a weakly coupled plasmas for which the potential of mean force is the Debye-Hückel potential, the collision volume is characterized by the Debye length. The equations of motion for two charged particles with masses m_1 and m_2 and charges e_1 and e_2 interacting in a uniform magnetic field $\mathbf{B}$ within the collision volume are

$$m_1\frac{d\mathbf{v}_1}{dt} = -\nabla_{\mathbf{r}_1}\phi(r) + e_1\Big(\frac{\mathbf{v}_1}{c}\times\mathbf{B}\Big) \tag{2.8}$$

$$m_2\frac{d\mathbf{v}_2}{dt} = -\nabla_{\mathbf{r}_2}\phi(r) + e_2\Big(\frac{\mathbf{v}_2}{c}\times\mathbf{B}\Big). \tag{2.9}$$

Since the potential depends only on the distance between the particles, it is useful to change the variables to the center of mass,

$$\mathbf{R} = \frac{m_1\mathbf{r}_1 + m_2\mathbf{r}_2}{m_1+m_2}, \tag{2.10}$$

$$\mathbf{V} = \frac{m_1\mathbf{v}_1 + m_2\mathbf{v}_2}{m_1+m_2}, \tag{2.11}$$

and the relative frame, $\mathbf{r} = \mathbf{r}_1 - \mathbf{r}_2$ and $\mathbf{u} = \mathbf{v}_1 - \mathbf{v}_2$. Under this transformation, the equations of motion for the center of mass and the relative velocities are

$$(m_1+m_2)\frac{d\mathbf{V}}{dt} = m_{12}\Big(\frac{\mathbf{u}}{c}\times\mathbf{B}\Big)\Big(\frac{e_1}{m_1} - \frac{e_2}{m_2}\Big) + (e_1+e_2)\Big(\frac{\mathbf{V}}{c}\times\mathbf{B}\Big), \tag{2.12}$$

$$m_{12}\frac{d\mathbf{u}}{dt} = -\nabla\phi(r) + m_{12}^2\Big(\frac{\mathbf{u}}{c}\times\mathbf{B}\Big)\Big(\frac{e_1}{m_1^2} + \frac{e_2}{m_2^2}\Big) + m_{12}\Big(\frac{\mathbf{V}}{c}\times\mathbf{B}\Big)\Big(\frac{e_1}{m_1} - \frac{e_2}{m_2}\Big). \tag{2.13}$$

These equations of motion describe how the precollision states transform to the postcollision states within the collision volume. The initial positions of the colliding particles in the relative frame correspond to the surface of the collision volume. For initial conditions corresponding to a precollision state, $\mathbf{u}\cdot\hat{\mathbf{s}} < 0$, the equations of motion are solved within the collision volume to obtain the postcollision velocities associated with the location at which the particles leave the collision volume. However, as indicated in Fig. 2.1, the precise shape of the collision volume can be arbitrary. The only relevant characteristic is that it must be significantly larger than the range of the potential of mean force [64]. As long as this condition is met, both the prec-

ollision and postcollision states correspond to a condition in which there is negligible interaction between the particles. In practice, choosing a collision volume that is much larger than the range of the potential of mean force increases the computational cost associated with evolving the particle trajectories, but it does not alter the momentum exchanged, which is the input to the collision operator resulting from trajectory calculation.

Although the general case does not require a specified volume, certain limits create symmetries that can be used to simplify the problem through the specification of a definite collision volume. We next consider two limiting cases: the traditional Boltzmann collision operator and O'Neil's collision operator.

2.2 Weakly magnetized limit: Boltzmann equation

In the unmagnetized and weakly magnetized regimes, the effect of the magnetic field in the collision volume is negligible. The dynamics of the colliding particles are modeled using the Debye-Hückel potential alone. The spherical symmetry of the Debye-Hückel potential suggests that a sphere is an appropriate collision volume.

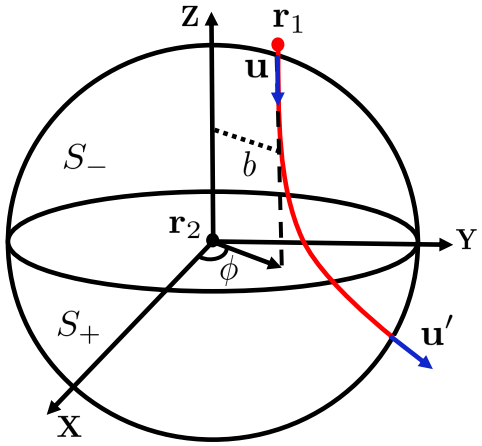

Figure 2.2: A spherical interaction volume around particle 2 ($\mathbf{r}_2$) in the presence of a repulsive interaction with particle 1 ($\mathbf{r}_1$). The disk surface is perpendicular to the precollision relative velocity ($\mathbf{u}$). Each point on the hemisphere (S_-) can be projected to a point on the disk as shown making a one to one correspondence.

The usual form of the collision operator can be obtained by introducing a plane perpendicular to the relative velocity $\mathbf{u}$ of the colliding particles and intersecting the sphere along a diameter with the coordinate system centered at particle 2 ($\mathbf{r}_1$) as shown in Fig. 2.2. The S_- surface is a hemisphere and the projection of it on this plane is a disk surface. Points on this disk surface have a one-to-one correspondence with the points on the hemisphere. This enables a transformation of the integration surface from the hemisphere to the disk surface. Using $b\,db\,d\phi$ as the area element of the polar coordinates on this disk, the collision operator can be recast as [34, 73]

$$\mathcal{C} = \int d^3\mathbf{v}_2 \int b\,db\,d\phi\,u(f_1' f_2' - f_1 f_2), \tag{2.14}$$

where $u = |\mathbf{u}|$ and b can be identified as the impact parameter from Fig. 2.2. Substituting $b\,db\,d\phi = \sigma d\Omega$, where σ is the differential scattering cross section and $d\Omega = \sin\theta d\theta d\phi$ is the solid angle, we get

$$\mathcal{C} = \int d^3\mathbf{v}_2 \int \sigma d\Omega\,u(f_1' f_2' - f_1 f_2). \tag{2.15}$$

This is the traditional Boltzmann collision operator. It is much simpler to evaluate than the general form of Eq. (2.7) because in the absence of a Lorentz force inside the collision volume, classical mechanics provides a closed form expression for the differential scattering cross section from the scattering angle [34]

$$\sigma = \frac{b}{\sin\theta}\left|\frac{db}{d\theta}\right| \tag{2.16}$$

where $\theta = \pi - 2\Theta$ and

$$\Theta = b\int_{r_0}^{\infty} dr \frac{1}{r^2}\left[1 - \frac{b^2}{r^2} - \frac{2\phi(r)}{m_{12}u^2}\right]^{-1/2} \tag{2.17}$$

is the scattering angle and r_0 is the distance of closest approach, obtained by finding the root of the denominator of the integrand. In this case, the problem reduces to solving the scattering angle integral (Eq. (2.17)). This is much simpler than the general case of solving the equations of motion (Eqs. (2.12) and (2.13)) of the colliding particles inside the collision volume, which are coupled ordinary differential equations.

2.3 Extremely magnetized limit: O'Neil equation

O'Neil developed a Boltzmann-like collision operator [35] that accounts for the collisions between particles of a one-component plasma in the extremely magnetized regime (region 4). This was later used to calculate the temperature anisotropy relaxation rate of a non-neutral plasma, and the predicted relaxation rate was validated experimentally [36, 76]. In this subsection, we show that O'Neil's results can be obtained from the generalized collision operator in the extremely magnetized limit by choosing the collision volume to be a cylinder.

The one-component plasma is a special case because when the charge-to-mass ratio is the same, the center of mass motion and relative motion are decoupled (Eqs. (2.12) and (2.13)). The resulting equations of motion in the relative frame are equivalent to that of a charged particle in a uniform magnetic field scattered by the potential at the origin. The resulting trajectory is that of a helix before and after the collision, but where both the parallel and gyromotion can change due to the collision. The natural geometry characterizing this motion is a cylinder, as depicted in Fig. 2.3.

For this geometry of the collision volume, Eq. (2.7) takes the form

$$\begin{aligned}\mathcal{C} = &\int d^3\mathbf{v}_2 \int \rho d\rho d\theta \, |\mathbf{u}\cdot\hat{\mathbf{z}}|(f_1' f_2' - f_1 f_2) \\ &+ \int d^3\mathbf{v}_2 \int \rho d\theta dz \, |\mathbf{u}\cdot\hat{\rho}|(f_1' f_2' - f_1 f_2).\end{aligned} \tag{2.18}$$

The first term corresponds to collisions in which particle 1 enters through the circular

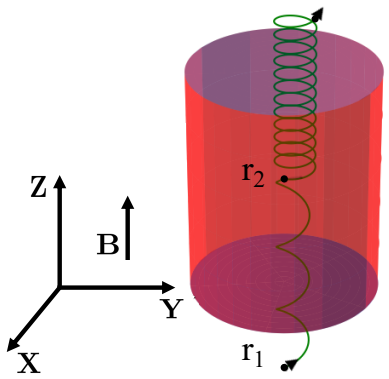

Figure 2.3: Cylindrical interaction volume around particle 2 ($\mathbf{r}_2$) during an interaction with particle 1 ($\mathbf{r}_1$) in the presence of a strong magnetic field.

surface (blue), and the second term corresponds to collisions in which particle 1 enters through the lateral surface (red) depicted in Fig. 2.3. When the plasma is extremely magnetized, the gyroradius of particles is so small compared to the size of the collision volume (λ_D) that motion is restricted to remain close to the guiding centers and scattering perpendicular to the initial guiding centers is minimal. In this case, the contribution to the collision operator from the second term (entering through the lateral surface) is negligible. In this limit

$$\mathcal{C} = \int d^3\mathbf{v}_2 \int \rho d\rho d\theta \, |\mathbf{u} \cdot \hat{\mathbf{z}}| (f_1' f_2' - f_1 f_2). \tag{2.19}$$

This is O'Neil's collision operator for extremely magnetized plasmas [35]. As there is no closed-form solution of the equations of motion of colliding particles in the presence of a magnetic field, they are solved numerically to find the postcollision states of the particles, except in the asymptotic case of a very large magnetic field where an approximation based on an adiabatic invariant was developed [36]. Even though the evaluation of the transport coefficients using O'Neil's theory is more difficult than the traditional Boltzmann theory, it is simpler than the general theory because the equations of motion in center of mass (Eq. (2.12)) and relative (Eq. (2.13)) frames are decoupled ($e_1/m_1 - e_2/m_2 = 0$ for a one-component plasma) making the numerical

calculation of the trajectories less computationally expensive.

CHAPTER III

Friction Force in Strongly Magnetized Plasmas

The generalized collision operator can be used to compute the macroscopic transport properties of the plasma in all magnetization strength regimes. To illustrate this, we compute the friction force acting on a massive projectile, taken to be a single test charge, moving through a magnetized one-component plasma. Understanding how friction is modified in the presence of a strong magnetic field is fundamentally important and it also has direct implications in many magnetized plasma experiments such as non-neutral plasmas [1], ultracold neutral plasmas [2], magnetic confinement fusion [7] and naturally occurring plasmas in planetary magnetospheres [12]. It is also the fundamental process controlling macroscopic transport of momentum.

A projectile moving through the plasma is acted upon by friction in addition to the Lorentz force from the external magnetic field. The friction force is due to Coulomb collisions with the background plasma. In the unmagnetized and weakly magnetized regimes, the Boltzmann equation predicts that the friction force is antiparallel to the velocity of the projectile and is commonly known as the stopping power [77]. It was recently predicted that a qualitatively new effect occurs in strongly magnetized plasmas: the friction force obtains a transverse component that is perpendicular to the velocity vector of the projectile, in the plane formed by $\mathbf{v}$ and $\mathbf{B}$ [56]. This prediction was made using linear response theory, and was later tested using molecular dynamics

simulations [78]. Since the transverse force is perpendicular to the velocity, it does not decrease the kinetic energy of the projectile. Thus it was not noticed in the conventional way of obtaining the stopping power by calculating the energy loss of the projectile [50, 79, 80, 81, 82]. Here, we test the generalized collision operator by comparing with the predictions of linear response theory in the strongly magnetized regime. We also compute the friction force in the extremely magnetized regime, showing that the transverse component of the friction force exists, and is large, in this regime. This extends the regime of magnetization over which this phenomenon has been studied because the linear response theory from [56] is not expected to apply in the extremely magnetized regime due to a close-collision cutoff in that theory.

3.1 Theory

Consider a massive test charge slowing down on a magnetized one-component plasma. Since the projectile is more massive than the particles constituting the background plasma, the gyromotion of the projectile happens at a larger spatial scale than the size of the collision volume. While the Lorentz force significantly influences the background plasma, it has a negligible influence on the massive test charge during the collision and can therefore be accurately excluded from the equations of motion for the test charge. The equations of motion from Eqs. (2.12) and (2.13) then reduce to

$$(m_1 + m_2)\frac{d\mathbf{V}}{dt} = e\Big(\frac{\mathbf{V}}{c} \times \mathbf{B}\Big) - \frac{e\, m_{12}}{m_2}\Big(\frac{\mathbf{u}}{c} \times \mathbf{B}\Big) \tag{3.1}$$

$$m_{12}\frac{d\mathbf{u}}{dt} = -\nabla\phi(r) + \frac{e\, m_{12}^2}{m_2^2}\Big(\frac{\mathbf{u}}{c} \times \mathbf{B}\Big) - \frac{e\, m_{12}}{m_2}\Big(\frac{\mathbf{V}}{c} \times \mathbf{B}\Big). \tag{3.2}$$

Here the charge on the massive projectile is taken to be the same as the charge of the background plasma particles ($e_1 = e_2 = e$). The friction force is $\mathbf{F} = \mathbf{R}^{12}/n_1$, where n_1 is the density of the projectile and $\mathbf{R}^{12}$ is the friction force density obtained by

taking the momentum moment of the collision operator,

$$\mathbf{R}^{12} = \int d^3\mathbf{v}_1 \int d^3\mathbf{v}_2 \int_{S_-} ds\, |\mathbf{u}\cdot\hat{\mathbf{s}}| m_1\mathbf{v}_1 (f_1' f_2' - f_1 f_2). \tag{3.3}$$

Equation (3.3) can be simplified using the principle of detailed balance [36] ($\int d^3\mathbf{v}_1 d^3\mathbf{v}_2$ $ds\, |\mathbf{u}\cdot\hat{\mathbf{s}}| m_1\mathbf{v}_1 f_1' f_2' = \int d^3\mathbf{v}_1 d^3\mathbf{v}_2 ds\, |\mathbf{u}\cdot\hat{\mathbf{s}}| m_1\mathbf{v}_1' f_1 f_2$). The derivation of the principle of detailed balance typically relies upon the invariance of the collision dynamics under time-reversal and space inversion to find an inverse collision [83]. But for a system with an externally generated magnetic field, the time-reversal symmetry is no longer valid (the system has the time-reversal invariance only if the reversal of current direction that produces the magnetic field is accounted for) making it difficult to find an inverse collision. Nevertheless, the system of charged particles with an externally generated magnetic field is expected to follow detailed balance because many collisions can be lumped together to produce a result with the same consequence as an inverse collision. This argument is similar to that made in polyatomic gases, which are another system in which a inverse binary collision does not exist [84]. Although a proof has not been developed for the magnetized plasma case, as it has for the polyatomic gas [84], we adopt the detailed balance relation as a postulate, as others have done [36]

After applying the detailed balance, the friction force density can be recast as

$$\mathbf{R}^{12} = \int d^3\mathbf{v}_1 \int d^3\mathbf{v}_2 \int_{S_-} ds |\mathbf{u}\cdot\hat{\mathbf{s}}| m_1 (\mathbf{v}_1' - \mathbf{v}_1) f_1 f_2, \tag{3.4}$$

where $\mathbf{v}_1'$ is the postcollision velocity of the projectile, obtained by solving the equations of motion. Since the projectile is a single particle, its distribution is a Dirac delta function. The background plasma distribution is taken as a uniform Maxwellian

distribution. Thus,

$$\begin{aligned} f_1 &= n_1\delta^3(\mathbf{v}_1 - \mathbf{v}_0), \\ f_2 &= \frac{n_2}{\pi^{3/2}v_T^3}\exp\left(\frac{-v_2^2}{v_T^2}\right), \end{aligned}$$

where n_2 is the density of the background plasma and $v_T = \sqrt{2k_BT/m_2}$ is the thermal velocity of the background plasma. On making these substitutions we get,

$$\mathbf{R}^{12} = \frac{n_1 n_2 m_1}{\pi^{3/2}v_T^3}\int d^3\mathbf{v}_2 \int\limits_{S_-} ds\,|\mathbf{u}\cdot\hat{\mathbf{s}}|(\mathbf{v}_1' - \mathbf{v}_0)\exp\left(\frac{-v_2^2}{v_T^2}\right). \tag{3.5}$$

Three components of the friction force are obtained from the friction force density using the following definitions

$$F_v = \frac{\mathbf{R}^{12}\cdot\hat{\mathbf{v}}_0}{n_1}, \tag{3.6a}$$

$$F_\times = \frac{\mathbf{R}^{12}\cdot(\hat{\mathbf{v}}_0\times\hat{\mathbf{n}})}{n_1}, \tag{3.6b}$$

$$F_n = \frac{\mathbf{R}^{12}\cdot\hat{\mathbf{n}}}{n_1}, \tag{3.6c}$$

where $\hat{\mathbf{n}}$ is the unit vector perpendicular to $\mathbf{v}_0$ and $\mathbf{B}$ defined as $\hat{\mathbf{n}} = \hat{\mathbf{v}}_0\times\hat{\mathbf{b}}/\sin\theta$, $\hat{b} = \mathbf{B}/|\mathbf{B}|$ is the unit vector in the direction of the magnetic field and θ is the angle between $\mathbf{v}_0$ and $\mathbf{B}$. Here, $-F_v$ is the stopping power, $F_\times$ is the transverse force and F_n is the friction force component along the direction of the Lorentz force. The geometry of the friction force components are shown in Fig. 3.1.

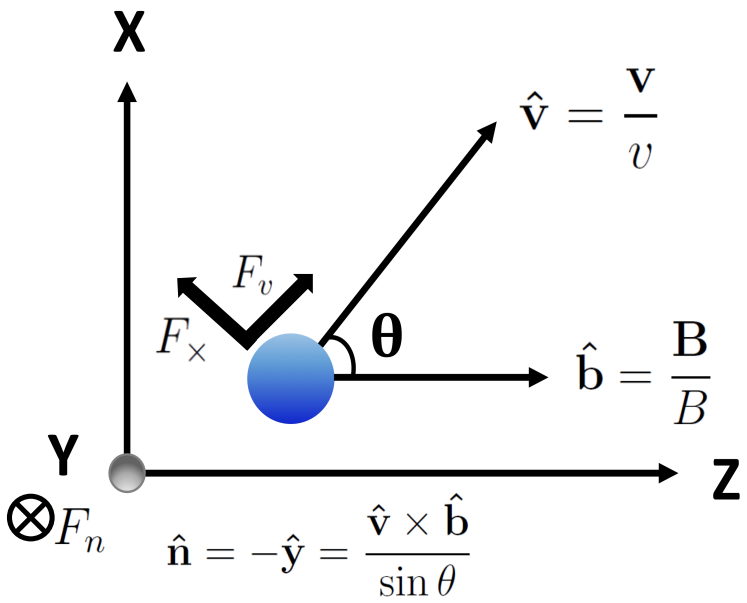

Figure 3.1: Friction force components in a strongly magnetized plasma.

3.2 Numerical evaluation

The integrals for computing different components of the friction force are five-dimensional: three in the velocity space and two in the coordinate space. They were solved numerically using Monte Carlo integration. The computational difficulty is that the coupled differential equations (Eq. (3.1) and Eq. (3.2)) describing the two-body interaction in a magnetic field must be solved numerically to compute the change in velocity of the projectile $(\mathbf{v}_1' - \mathbf{v}_0)$ for each Monte Carlo integration point. Because the parameter-space is five-dimensional, a very large number of integration points is required for convergence. In our computations, the number ranged from 10^6 to 10^8. In order to solve the integrals numerically, the equations were first made dimensionless by normalizing the time with the plasma frequency, distance with the Debye length and velocity with the Debye length times the plasma frequency. Using

the scaled variables,

$$\mathbf{R}^{12} = \frac{m_r k_B T n_1}{8\sqrt{6}\pi^{5/2}\Gamma^{3/2}\lambda_D} \int \tilde{v}_2^2 \sin\theta_{v_2} d\theta_{v_2} d\phi_{v_2} d\tilde{v}_2$$
$$\times \int_{\tilde{S}_-} \tilde{R}_s^2 \sin\theta_{R_s} d\theta_{R_s} d\phi_{R_s} |\tilde{\mathbf{u}} \cdot \hat{\mathbf{s}}| (\tilde{\mathbf{v}}_1' - \tilde{\mathbf{v}}_0) \exp\left(\frac{-\tilde{v}_2^2}{2}\right). \tag{3.7}$$

Here, the collision volume is taken as a sphere and the integrals are written in spherical polar coordinates for both velocity and space (recall that the shape of the collision volume is unimportant in the general theory, so long as it is large compared to the range of the interparticle force). Since the potential falls off exponentially on the Debye length scale, the radius of the sphere (R_s) is taken as 2.5 Debye lengths for computations in which the Coulomb coupling strength is $\Gamma = 0.1$ and 3.5 Debye lengths for $\Gamma = 0.01$. Here, m_r is the ratio of the mass of the projectile to that of the background plasma particle ($m_r = \frac{m_1}{m_2}$) and the variables with tilde ($\tilde{}$) on top represent scaled variables. We note that although Eq. (3.7) has a leading term that is proportional to m_r, the true scaling of the friction force density is a non-trivial function of mass that depends on the result of the trajectory calculation. The expectation is that it becomes independent of the projectile mass in the limit that the projectile is much more massive than the background plasma. This can be seen by considering Eqs. (3.1) and (3.2). When $m_r \gg 1$, $\Delta\mathbf{V} \propto 1/m_r$ and $\mathbf{V} \approx \mathbf{v}_1$. Using this result in equation (3.7) shows that the friction force density is expected to become independent of the ion mass in this limit.

A variety of Monte Carlo integration techniques are available to reduce the large number of sample points required in the integration routine. One common technique is the transformation method [36, 85], but this requires an approximate analytic expression for the change in momentum of the projectile during a collision. As there is no known analytic expression for this problem, a different technique is desirable. Instead, we use an adaptive Monte Carlo integration technique - VEGAS [85, 86, 87,

88]. In this method, the integration variables are recast in an attempt to make the integrand a constant and a Monte Carlo integration is performed. These two steps are iterated several times. The algorithm uses the information about the integrand from one iteration to optimize the change of variable for the next iteration.

Friction force curves were obtained by evaluating the integrals (Eqs. (3.6a), (3.6b) and (3.6c)) based upon trajectory calculations with initial conditions selected from the adaptive Monte Carlo algorithm. Each point in this 5-D integral corresponds to an initial velocity of the background particle and an initial position in the relative coordinates

$$\tilde{\mathbf{r}}_i = \begin{bmatrix} \tilde{R}_s \sin\theta_{R_s} \cos\phi_{R_s} \\ \tilde{R}_s \sin\theta_{R_s} \sin\phi_{R_s} \\ \tilde{R}_s \cos\theta_{R_s} \end{bmatrix} \tag{3.8}$$

$$\tilde{\mathbf{v}}_{2i} = \begin{bmatrix} \tilde{v}_2 \sin\theta_{v_2} \cos\phi_{v_2} \\ \tilde{v}_2 \sin\theta_{v_2} \sin\phi_{v_2} \\ \tilde{v}_2 \cos\theta_{v_2} \end{bmatrix} \tag{3.9}$$

and the initial velocity of the projectile $\tilde{\mathbf{v}}_{1i}$ is taken as $\tilde{\mathbf{v}}_0$. The unit normal vector is $\hat{\mathbf{s}} = \tilde{\mathbf{r}}_i/\tilde{R}_s$. Using Eq. (2.10), $\tilde{\mathbf{v}}_0$ and $\tilde{\mathbf{v}}_{2i}$ were transformed to the relative and the center of mass coordinates. For initial states that satisfy $\tilde{\mathbf{u}} \cdot \hat{\mathbf{s}} < 0$, the two particle equations of motion (Eq. (3.1) and Eq. (3.2)) were solved using the 'DOP 853' method [89]. The trajectory calculations were stopped when the particle crossed the collision volume, i.e, $|\tilde{\mathbf{r}}| > \tilde{R}_s$ and the change of projectile velocity $(\tilde{\mathbf{v}}_1' - \tilde{\mathbf{v}}_0)$ was calculated. Twenty iterations of the VEGAS grid adaptation and the integral estimate were made. The final result and error was obtained by taking the weighted average of the last 10 iterations with the weight chosen to be the inverse of the variance of each of those iterations. The numerical implementation is described in detail in appendix A. Results from evaluation of the friction force in different transport regimes are discussed in the following section.

3.3 Results

In this section, we discuss the results from calculation of the friction on the projectile and compare it with the traditional Boltzmann theory and the linear response theory. The traditional Boltzmann theory is valid for the unmagnetized and weakly magnetized regimes and predicts that the stopping power is the only non-zero component of the friction force. The expression for the stopping power when the interaction is modeled using the Debye-Hückel potential in the traditional Boltzmann collision theory is [77]

$$F_v = \frac{-n_2 m_{12} v_T}{2\sqrt{\pi}|\mathbf{v}_0|^2} \int du u^2 \sigma^{(1)}(u) \Big[e^{-(u-|\mathbf{v}_0|)^2/v_T^2} \Big(\frac{2u|\mathbf{v}_0|}{v_T^2} - 1 \Big) + e^{-(u+|\mathbf{v}_0|)^2/v_T^2} \Big(\frac{2u|\mathbf{v}_0|}{v_T^2} + 1 \Big) \Big], \tag{3.10}$$

where

$$\sigma^{(1)} = 4\pi \int_0^\infty bdb \cos^2 \Theta(b,u) \tag{3.11}$$

is the momentum-transfer scattering cross section and $\Theta(b,u)$ is the scattering angle (Eq. (2.17)).

Linear response theory is valid in all the transport regimes except the extremely magnetized regime. It computes the friction force from the induced electric field associated with the wake generated by the movement of a projectile (ion) in the plasma. The result is [56]

$$\mathbf{F} = -\frac{e^2}{2\pi^2} \int d^3k \frac{\mathbf{k}}{k^2} \mathrm{Im} \Big\{ \frac{1}{\hat{\epsilon}(\mathbf{k}, \mathbf{k}\cdot\mathbf{v})} \Big\}, \tag{3.12}$$

where $\mathbf{k}$ is wave vector and

$$\hat{\epsilon}(\mathbf{k}, \mathbf{k}\cdot\mathbf{v}) = 1 + \frac{1}{k^2\lambda_D^2}\left[1 + \frac{\mathbf{k}\cdot\mathbf{v}}{|k_{||}|v_T}\exp\left(\frac{-k_\perp^2 v_T^2}{2\omega_c^2}\right)\right] \times\left[\sum_{n=-\infty}^{\infty} I_n\left(\frac{k_\perp^2 v_T^2}{2\omega_c^2}\right) Z\left(\frac{\mathbf{k}\cdot\mathbf{v} - n\omega_c}{|k_{||}|v_T}\right)\right] \tag{3.13}$$

is the linear dielectric response function of the plasma. Here, Z is the plasma dispersion function [90], I_n is the nth order modified Bessel function of the first kind, and $k_{||}$ and $k_\perp$ are parallel and perpendicular components of the wave vector with respect to the direction of the magnetic field. Since the linear response theory does not account for the short range collisions, it would lead to a logarithmic divergence [91]. This is typically avoided by choosing a high wave number cut off for the k integral, $k_{\max} = m_{12}(v_T^2 + v_0^2)/e^2$, which is approximately the inverse of distance of closest approach [92].

3.3.1 Unmagnetized and weakly magnetized plasma

In order to test the generalized collision operator, and our numerical implementation, we first compute the friction force in the unmagnetized and weakly magnetized plasma regimes and compare the results with the accepted results from the Boltzmann equation. Our computations are consistent with the expectation from the Boltzmann equation that, in this regime, only the stopping power component F_v is non-zero [77]. Figure 3.2 compares the stopping power curve obtained using the generalized collision operator to the result of the traditional Boltzmann collision operator with the Debye-Hückel potential as well as the results of linear response theory [92] for $\Gamma = 0.1$ and $\Gamma = 0.01$. Since the influence of the magnetic field during collisions is negligible, the magnetic field was taken as zero in the equations of motion (Eq. (3.1) and Eq. (3.2)).

Results from the generalized and traditional Boltzmann collision operators agree to within numerical tolerances. Of course, this is expected since the traditional Boltz-

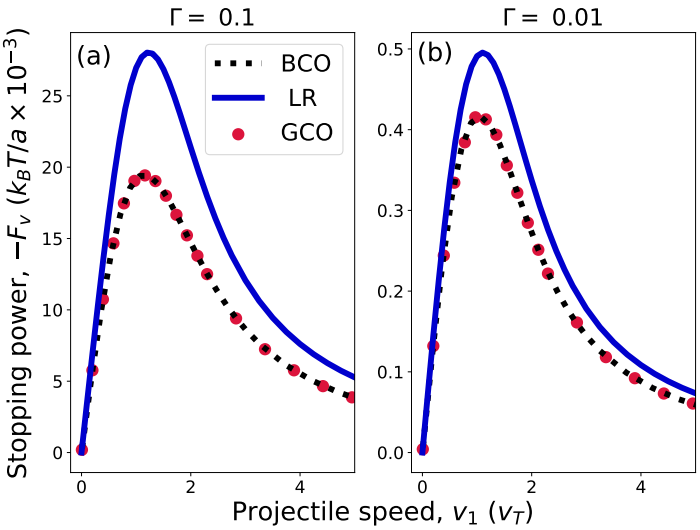

Figure 3.2: Stopping power ($-F_v$) of a massive projectile ($m_r = 1000$) in a light background plasma with the coupling strengths (a) $\Gamma = 0.1$ and (b) $\Gamma = 0.01$ using the generalized collision operator (GCO). Also shown are the predictions using the linear response theory (LR) and the traditional Boltzmann collision operator (BCO)

mann collision operator is a limiting case of the generalized collision operator. Nevertheless, this comparison also helps to verify the generalized collision operator and our numerical implementation.

The linear response predicts a slightly larger stopping power than the predictions by the binary collision models. Sources of discrepancy between these approaches include the absence of the velocity-dependent screening (dynamic screening) in the Debye-Hückel potential used for modeling the binary collisions, as well as uncertainty in the short-range cut off length (Landau length) used in the linear response theory to avoid the logarithmic divergence caused by neglecting strong nonlinear scattering associated with close collisions [91]. The strengths and weaknesses of these models were previously studied using molecular dynamics simulations [93, 94], and the results shown in Fig. 3.2 are consistent with these previous studies. Results from the two methods merge in the limit $\Gamma \to 0$.

3.3.2 Strongly magnetized plasma

In the strongly magnetized regime, the magnetic field influences the collision dynamics, causing the numerical evaluation of the trajectories of colliding particles to become much more computationally expensive. The computational expense was reduced by optimizing the number of integration points per iteration of VEGAS (*neval*) and setting the tolerance for the trajectory calculations (*tol*) in order to achieve a chosen numerical accuracy of the computed friction force coefficients. The tolerance of the trajectory calculation is set by both the relative tolerance and the absolute tolerance, which were taken to be the same. Figure 3.3 shows an example convergence test for the transverse force on a projectile in a background plasma of $\Gamma = 0.1$ and $\beta = 50$ and having speed $0.2v_T$ and $2v_T$. In (a), the tolerance was chosen to be 10^{-8} and convergence with respect to the number of integration points was established. In (b), the number of integration points for each iteration was chosen to be 10^6 and convergence with respect to the tolerance was established. As expected, convergence is obtained as the number of integration points increases, as well as when the tolerance of the trajectory calculation decreases. The number required for convergence was observed to depend on the projectile speed, as well as the Γ and β parameters. Nevertheless, a tolerance of 10^{-8} and number of integration points for each iteration of 10^6 was sufficient to obtain convergence to less than 1% throughout the strongly magnetized and extremely magnetized regimes.

Figure 3.4 shows the friction force curves obtained using the generalized collision operator and the linear response theory for the coupling strength $\Gamma = 0.1$ and the magnetic field strength $\beta = 10$ for different orientations of the initial projectile velocity with respect to the magnetic field. Only a qualitative agreement can be reached between the curves from these two theories, because of the shortcomings of the two models that were discussed in the previous subsection.

The main result of this chapter is shown in panels (b) and (e) of Fig. 3.4. This

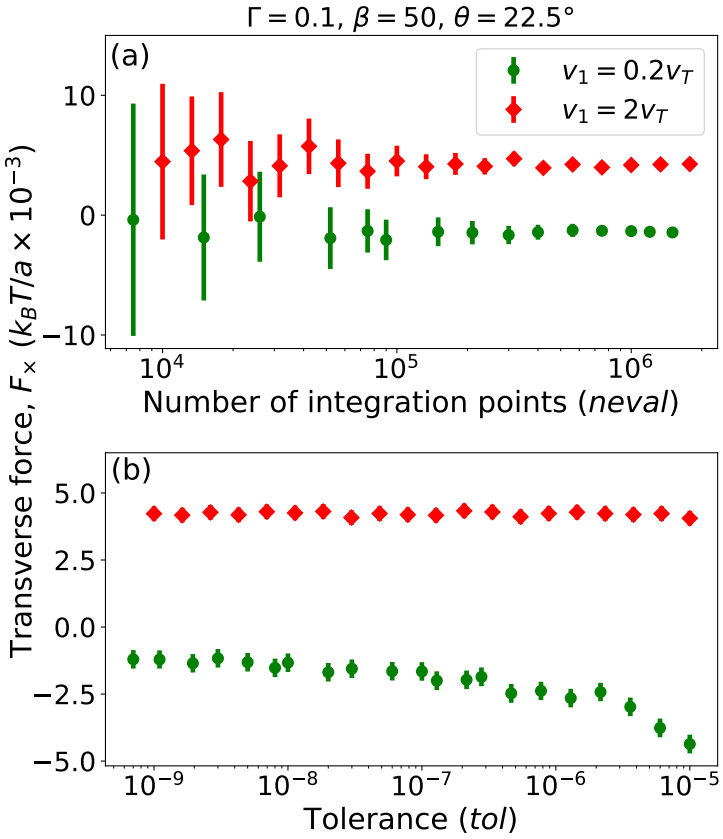

Figure 3.3: Transverse force ($F_\times$) on a projectile in a light background plasma of $\Gamma = 0.1$ and $\beta = 50$ as a function of (a) number of integration points per iteration (*neval*) and (b) tolerance in trajectory calculation (*tol*). The velocity of the projectile makes an angle of 22.5° with the direction of the magnetic field and initial speed of $v_1 = 0.2v_T$ (green circle) and $v_1 = 2v_T$ (red diamond).

shows that a significant transverse component of the friction force is predicted by the GCO computations. The existence of this component was recently predicted by the linear response approach. Our results demonstrate that this effect is captured in the more complete description from the collision operator of a kinetic theory. It also demonstrates that the effect is captured by the binary collision approach. The two approaches predict qualitatively similar behavior, but have quantitative differences at a similar level to what was observed in the unmagnetized case. This is expected at $\Gamma = 0.1$ due to the uncertainties associated with the screening model, or the

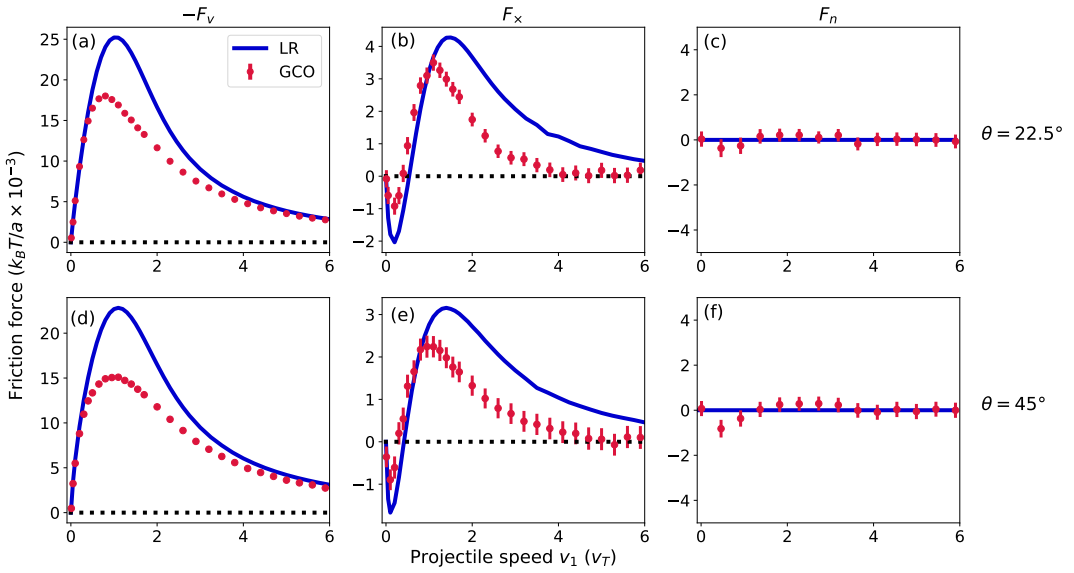

Figure 3.4: Friction force on a massive projectile ($m_r = 1000$) slowing down on a light background plasma with coupling strength $\Gamma = 0.1$ and magnetic field strength $\beta = 10$ for different initial projectile velocity angles with respect to the magnetic field $\theta = 22.5°$ [a, b, and c] and $\theta = 45°$ [d, e, and f]. The generalized collision operator results (GCO) and linear response theory curve (LR).

short-range cutoff. However, the two approaches would be expected to merge as the coupling strength decreases.

In linear response theory, the friction force on the projectile is due to the induced electric field associated with the wake generated by the projectile in the background plasma. But in the binary collision theory, the friction force is the net force acting on the projectile from subsequent binary interactions with the background plasma. The linear response theory attributes the origin of the transverse force to the way in which the Lorentz force on the background plasma influences the instantaneously generated wake. In contrast, the generalized collision operator captures the transverse force by accounting for the gyromotion of the background particles while interacting with the projectile. Even though these two are completely different approaches, they both are equally capable of capturing the physics of transverse force in this regime.

On comparing the stopping power curves ($-F_v$) from Fig. 3.4 with those for the

weakly magnetized regime from Fig. 3.2, qualitative changes are observed. The position of the peak shifts to a lower speed, and the magnitude of the force decreases at the Bragg peak, but decays less rapidly with speed. The stopping power is also observed to depend on the orientation of the projectile velocity with respect to the magnetic field. The friction force along the direction of the Lorentz force (F_n) is much smaller than either the stopping power or transverse force. Points computed at most velocities are consistent with zero to within the estimated accuracy of the data, but there are a few points at which the computed force appears to be non-zero. This is a qualitative distinction with the predictions of linear response theory and is studied in greater detail in next chapter. We expect that the agreement between these two approaches becomes better as Γ decreases.

3.3.3 Extremely magnetized plasma

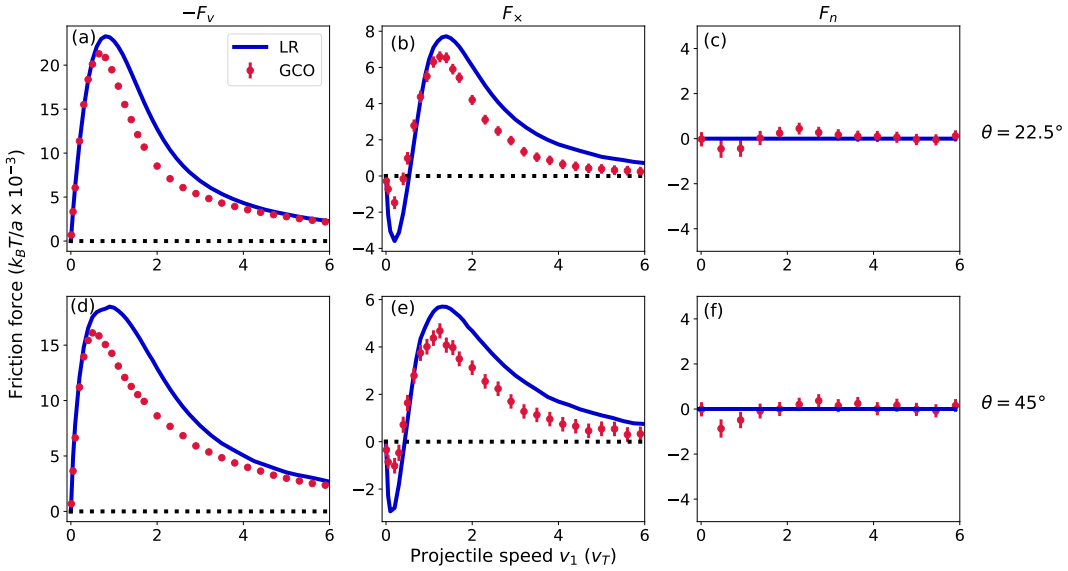

Figure 3.5: Friction force on a massive projectile ($m_r = 1000$) slowing down on a light background plasma with coupling strength $\Gamma = 0.1$ and magnetic field strength $\beta = 50$ for different initial projectile velocity angles with respect to the magnetic field $\theta = 22.5°$ [a, b, and c] and $\theta = 45°$ [d, e, and f]. The generalized collision operator results (GCO) and linear response theory curve (LR).

Figure 3.5 shows the friction force curves obtained using the generalized collision operator and the linear response theory for the coupling strength $\Gamma = 0.1$ and the magnetic field strength $\beta = 50$ for different orientations of the initial projectile velocity with respect to the magnetic field. On comparing with the friction force curves in the strongly magnetized regime, the magnitude of the friction force is predicted to increase and the peak of stopping power curve shifts slightly to lower projectile speeds. Similar to the case of strongly magnetized regime, the friction force in the direction of the Lorentz force, F_n is much smaller than either the stopping power or transverse force.

Linear response theory assumes that the interactions are weak and are small angle collisions. In order to avoid the divergence in the theory caused by the strong large-angle collisions an ad hoc short-range cut off is introduced at the Landau length. These assumptions break down in the extremely magnetized regime. In this regime, the gyroradius is the smallest length scale and the particles are bound to the magnetic field lines. The collisions between the particles are strong and are large-angle collisions. However, the physics of strong interactions are captured by the binary collision theory. This makes the generalized collision operator a strong candidate to understand the physics of the extremely magnetized plasmas. Although the $k_{\max}$ cutoff used in the linear response theory is not expected to apply in the extremely magnetized regime, Fig. 3.5 shows a similar level of agreement between linear response theory and the GCO as is observed in the strongly magnetized regime shown in Fig. 3.4. It is unknown if this a fortuitous agreement particular to this combination of Γ and β, or if it will also extend to yet stronger magnetization.

3.4 Discussion

This section provides a qualitative description of the physical origin of the transverse friction force due to strong magnetization from the binary collision perspective.

Binary collision theory calculates the friction force via the change in momentum of the projectile after a sequence of elementary binary collisions with the background plasma particles that includes all possible scattering events. When the gyroradius of the colliding particles are larger than the characteristic scattering length (λ_D), the influence of the magnetic field during the collisions is negligible. In this case, background plasma particles collide with the projectile from all the directions with equal probability. The net change in momentum from the collisions in all the directions except parallel or antiparallel to the projectile velocity will be zero. For instance, take the projectile velocity to be in the $+\hat{x}$ direction as shown in panel (a) of Fig. 3.6. Here, the projectile is labeled (P) and the background particles are numbered r_1 to r_4. The change in momentum of the projectile from a collision with a background particle having velocity $v\hat{y}$ ($\mathbf{r}_4$) is canceled by the change in momentum from a collision with a background particle having velocity $-v\hat{y}$ ($\mathbf{r}_3$). This leads to the conclusion that there is no transverse component of the friction. In contrast, the change in momentum of the projectile from collisions with the background particle having velocity $-v\hat{x}$ ($\mathbf{r}_1$) is greater than from a collision with velocity $+v\hat{x}$ ($\mathbf{r}_2$) because of the larger magnitude of the relative velocity. Thus the friction force is antiparallel to the projectile velocity.

When the plasma is strongly magnetized or extremely magnetized, background particles are bound to the magnetic field lines, effectively making their motion 1-D. This restricts the approach of background particles to the projectile along the $\pm\hat{b}$ direction, breaking the symmetry of particles approaching uniformly from all directions, as in the unmagnetized and weakly magnetized cases. Panel (b) of Fig. 3.6 shows the collision of a projectile with four different background particles. The projectile (P) velocity vector makes an angle θ with respect to the magnetic field and the background particles are numbered $\mathbf{r}_1$ to $\mathbf{r}_4$.

Consider the case that the velocity vector of the projectile makes an acute angle to the magnetic field ($0° \leq \theta \leq 90°$). The net change in momentum of the projectile

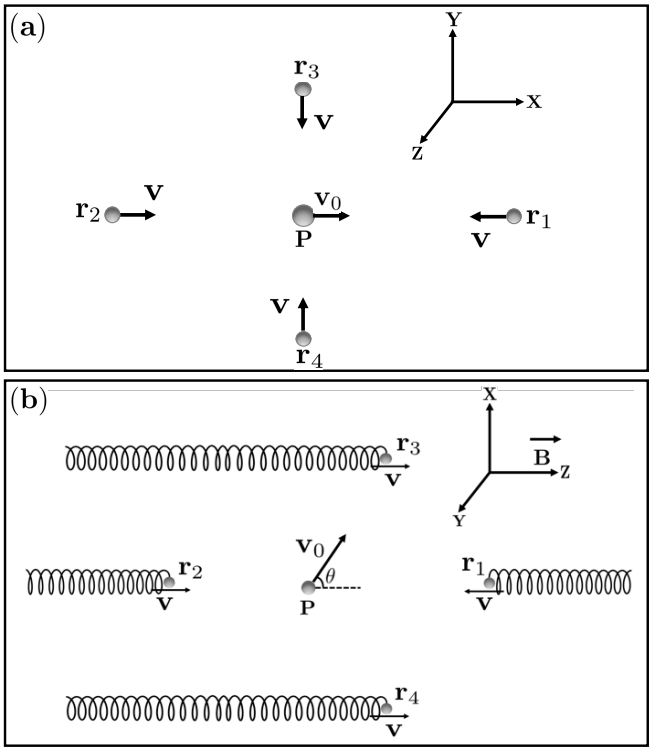

Figure 3.6: Illustration of collisions of the massive projectile with the background particles - (a) unmagnetized and weakly magnetized (b) strongly magnetized and extremely magnetized transport regimes.

along the magnetic field direction from collisions with the background plasma particles approaching from the $+\hat{b}$ direction will be higher than that of the collision with background plasma particle approaching from the $-\hat{b}$ direction, resulting in a force anti parallel to the direction of the magnetic field. For example consider the collision between particle 1 ($\mathbf{r}_1$) and particle 2 ($\mathbf{r}_2$). Both the particles have equal speed, but the relative velocity is higher for the collision with particle 2, resulting in higher exchange of momentum.

The projectile also experiences a net force in the $-\hat{x}$ direction. This can be understood by comparing collisions between the projectile and particle 3 ($\mathbf{r}_3$) or particle 4 ($\mathbf{r}_4$). The projectile experiences more change in momentum from the collision with particle 3 than collision with particle 4 because the projectile is moving towards the particle 3. The conclusion of these arguments is that the presence of the magnetic

field breaks the symmetry about the velocity vector, causing there to be both a stopping power component antiparallel to the velocity and a transverse component perpendicular to the velocity in the plane of $\mathbf{v}_0$ and $\mathbf{B}$.

The force on the projectile in the $\hat{y}$ direction is nominally expected to be zero because the projectile has no component of the velocity in this direction, other than its gyromotion, and the symmetry of momentum exchange with particles entering from either $\pm\hat{y}$ directions is expected to balance. For instance, the force on the projectile in the $\hat{y}$ direction from a background particle moving along the magnetic field line at $|y|\hat{y}$ is canceled by the force from the background particle moving along the field line at $-|y|\hat{y}$.

The above discussion considered oblique angles between $\mathbf{v}_0$ and $\mathbf{B}$, but when the projectile moves either perpendicular or parallel to the magnetic field, symmetry about the projectile velocity vector is expected to return, and the transverse component of the friction force to vanish. Consider a projectile moving perpendicular to the magnetic field in the $\hat{x}$ direction. In this case, the projectile is not expected to experience any net force in the $\hat{z}$ direction as the momentum exchanged in collisions with background particles approaching from the $+\hat{b}$ and $-\hat{b}$ directions are antisymmetric. In this case, the projectile experiences a force in the $-\hat{x}$ direction only. Thus, a projectile moving perpendicular to the magnetic field only has a stopping power component and no transverse force. Similar arguments of symmetry can be made to understand why there is also no transverse component when the projectile velocity aligns along the magnetic field. Although the solutions in the previous section focused only on oblique angles, these symmetry properties were confirmed, and they have also been shown to hold in both the previous linear response calculations [56] and molecular dynamics simulations [78].

CHAPTER IV

Friction Force in Strongly Coupled Strongly Magnetized Plasmas

The effects of strong magnetization on the friction force when the plasma is weakly coupled were discussed in the last chapter. It was found that strong magnetization significantly affects the friction force. Instead of being aligned antiparallel to the velocity vector, the friction force shifts, gaining a transverse component that is perpendicular to the velocity vector in the plane formed by the velocity and magnetic field vectors. However, many magnetized experiments such as ultracold neutral plasmas [25], non neutral plasmas [1] and antimatter plasmas [3] exhibit strong Coulomb coupling ($\Gamma > 1$) in addition to strong magnetization. This chapter extends the generalized collision operator from weak coupling to strong coupling. This is done by combining the generalized collision operator with the mean force kinetic theory that extends the traditional Boltzmann equation to treat strong Coulomb coupling. The mean force kinetic theory is derived based on an expansion related to the deviation of correlations from their equilibrium values, rather than in terms of the strength of correlations [64]. The result is similar to the Boltzmann equation, but where binary collisions occur via the potential of mean force, rather than the bare (Coulomb) potential.

In order to test this model, we compute the friction force on a single massive

charged particle (ion) moving through a background one-component plasma (electrons). We choose the friction force on a single particle as the test transport model for a few reasons: first-principles molecular dynamics (MD) simulation data are available with which to benchmark the theory [95] and these data predict novel transport behaviors associated with strong coupling and strong magnetization that a correct kinetic theory should be able to reproduce. The MD simulations [95] have revealed that a third "gyrofriction" component of the friction force vector arises in the strongly coupled strongly magnetized regime: $F_n = \mathbf{F} \cdot \hat{\mathbf{n}}$. Here, we show that the kinetic theory is able to capture this physical effect. The theory is also used to provide an explanation for the physical origin of the gyrofriction force, which arises due to asymmetries associated with gyromotion during close collisions. This chapter is based on Ref. [71].

4.1 Theory and evaluation

When the plasma is strongly coupled, spatial correlations between the particles become significant. The theory accounts for this many-body effect in the collision by using the potential of mean force, which is the potential obtained by fixing the positions of two particles at a distance r apart and averaging over the positions of the remaining particles at equilibrium. In the strongly coupled regime, the potential of mean force for a one-component plasma can be accurately modeled using the hypernetted-chain approximation (HNC) [96]

$$g(r) = \exp[-v(r)/k_B T + h(r) - c(r)], \tag{4.1a}$$

$$\hat{h}(k) = \hat{c}(k)[1 + n\hat{h}(k)], \tag{4.1b}$$

where $h(r) = g(r) - 1$, $\hat{h}(k)$ is the Fourier transform of $h(r)$, $v(r) = e^2/r$ is the Coulomb potential, $c(r)$ is the direct correlation function and $\hat{c}(k)$ is its Fourier trans-

form. The potential of mean force is obtained from the pair distribution function via: $\phi(r) = -k_B T \ln(g(r))$. The pair distribution function and the potential of mean force for coupling strengths $\Gamma = 0.1$, 1, 10 and 100 are shown in Figs. 4.1 and 4.2 respectively.

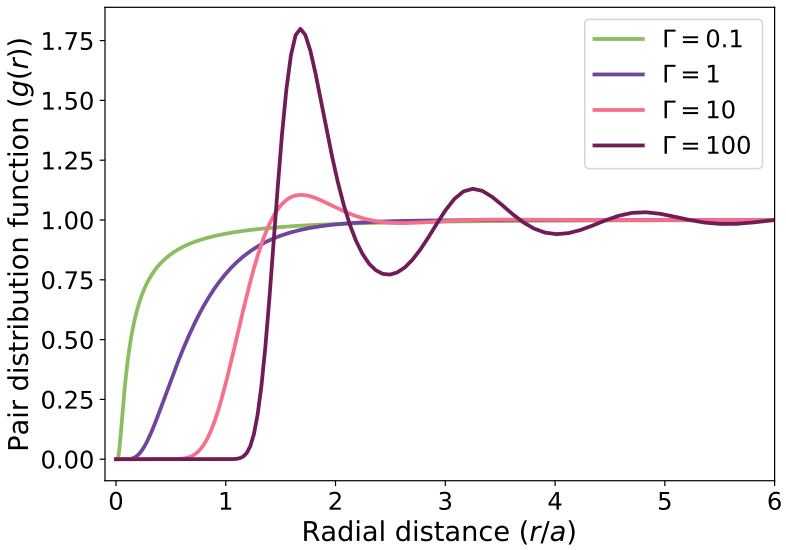

Figure 4.1: Pair distribution function for the one-component plasma at $\Gamma = 0.1$, 1, 10 and 100.

The use of the potential of mean force to model binary interactions introduces aspects of many-body effects such as screening and correlations that become essential at strong coupling. The mean force kinetic theory also accounts for the Coulomb hole surrounding the particles interacting via Coulomb force [97]. This excluded volume leads to a reduced volume of space that the particles can occupy resulting in an increased collision frequency for strongly coupled plasma. This leads to a frequency enhancement factor $\chi[g(r = \sigma)]$, where σ is the Coulomb hole radius, in the collision operator. This is obtained from the modified version of the Enskog's theory of hard spheres for plasmas developed in Ref. [97]. In this model, the χ factor is computed based on a property of thermodynamic equilibrium $[g(r)]$, and as a result does not depend on the strength of the magnetic field. The χ factor for the coupling strengths

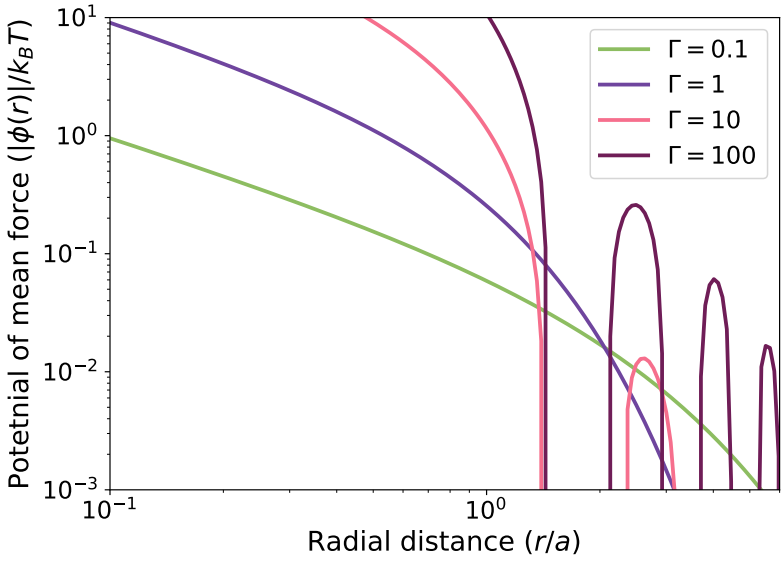

Figure 4.2: Potential of mean force for the one-component plasma at $\Gamma = 0.1$, 1, 10 and 100.

studied here $\Gamma = 1$, 10 and 100 are 1.36, 1.45 and 1.65 respectively. The modified expression of the friction force density after including the χ factor is

$$\mathbf{R}^{12} = \frac{\chi n_1 n_2 m_1}{\pi^{3/2} v_T^3} \int d^3\mathbf{v}_2 \int_{S_-} ds\, |\mathbf{u}\cdot\hat{\mathbf{s}}|(\mathbf{v}_1' - \mathbf{v}_0) \exp\left(\frac{-v_2^2}{v_T^2}\right). \tag{4.2}$$

The potential of mean force, $\phi(r)$, was computed numerically by solving Eqs. (4.1a) and (4.1b). The result was interpolated using the Cubic spline method [85] for the trajectory calculations. Numerical evaluation of the friction force integral, Eq. (4.2), was the same as that described in chapter III except that the numerically computed potential of mean force was used instead of the Debye-Hückel potential, and the variables used to solve the equations of motion inside the collision volume were scaled using the Wigner-Seitz radius (a) instead of the Debye-length (λ_D) to account for the change in the scale of the collision volume at strong coupling. Since the potential falls off rapidly on the inter-particle distance scale, the radius of the spherical collision volume for the coupling strengths $\Gamma = 1$, 10 and 100 were taken to be $2.89a$, $2.74a$ and

4.16a respectively. It was confirmed that these were large enough to reach convergence with respect to the size of the collision volume.

4.2 Results

4.2.1 Comparison with molecular dynamics simulations

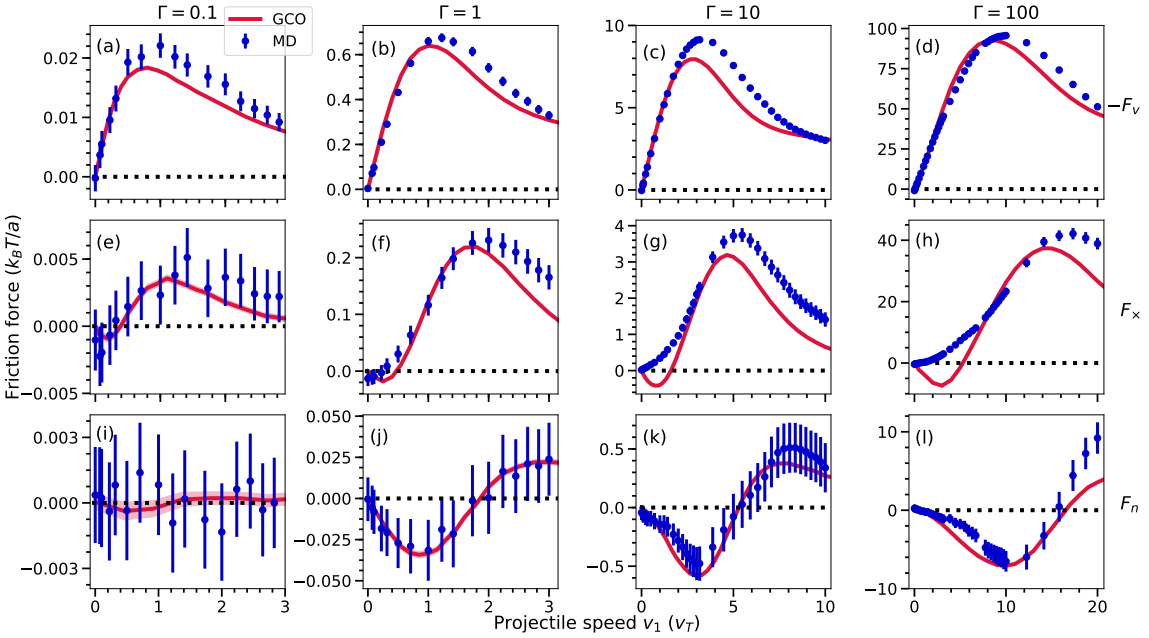

Figure 4.3: Friction force components at $\beta = 10$ and $\theta = 22.5°$ for different coupling strengths $\Gamma = 0.1$ [(a), (e), and (i)], $\Gamma = 1$ [(b), (f), and (j)], $\Gamma = 10$ [(c), (g), and (k)]and $\Gamma = 100$ [(d), (h), and (l)]. The generalized collision operator (GCO) results are shown as red solid lines and the molecular dynamics (MD) results as data points.

In order to test the results computed from the generalized collision operator, Eq. (4.2), we compare with results of recent molecular dynamics simulations [95]. Molecular dynamics simulations provide a rigorous benchmark because they directly solve the first-principles equations of motion for all interacting particles. The results are compared across different coupling strengths, magnetization strengths and orientation of the projectile's velocity with respect to the direction of magnetic field.

Figure 4.3 compares the friction force curves by fixing the magnetization strength ($\beta = 10$) and orientation of projectile's velocity with respect to the direction of the

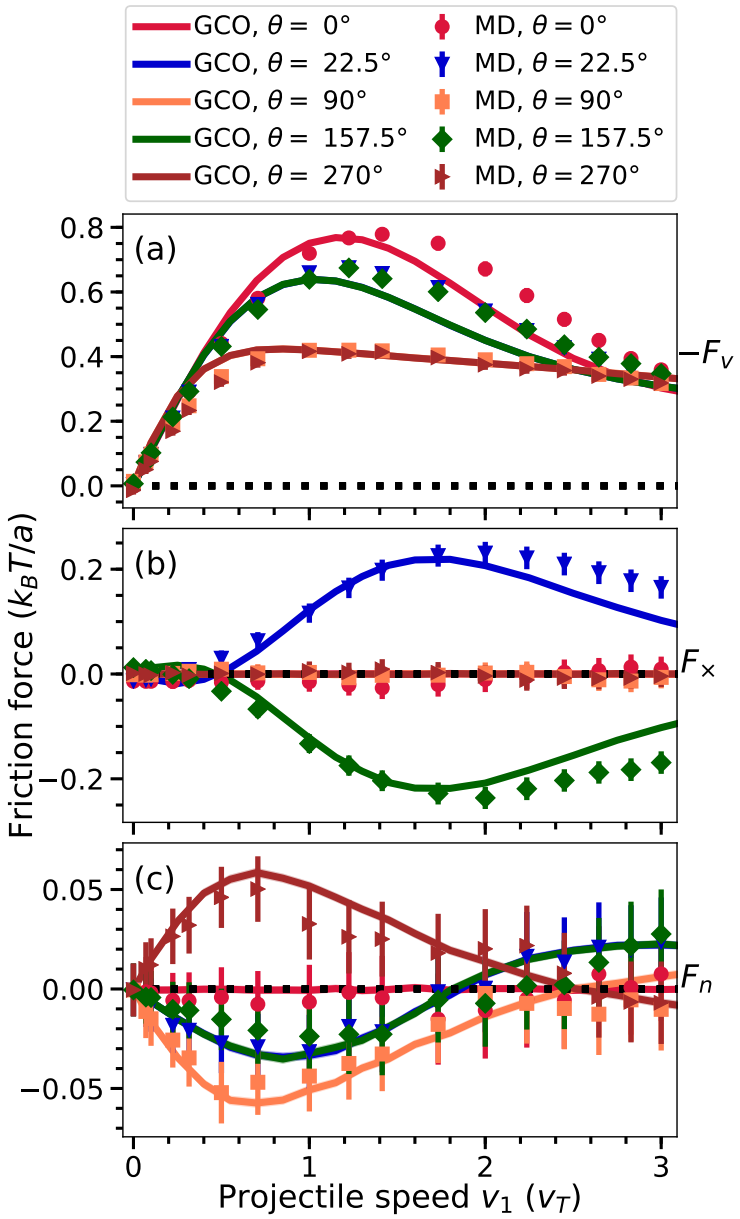

Figure 4.4: Comparison of GCO (lines) and MD (data points) predictions for the friction force components $[-F_v$ in (a), $F_\times$ in (b) and F_n in (c)] at $\Gamma = 1$ and $\beta = 10$ for different orientations of projectile and magnetic field $\theta = 0°$, 22.5°, 90°, 157.5° and 270°.

magnetic field ($\theta = 22.5°$) and varying the coupling strength ($\Gamma = 0.1, 1, 10$ and 100). The model predictions are generally in good agreement with the MD results across this entire range of coupling strengths. At $\Gamma = 100$, the plasma is liquid-like and the agreement between theory and MD is quite remarkable. In these plots,

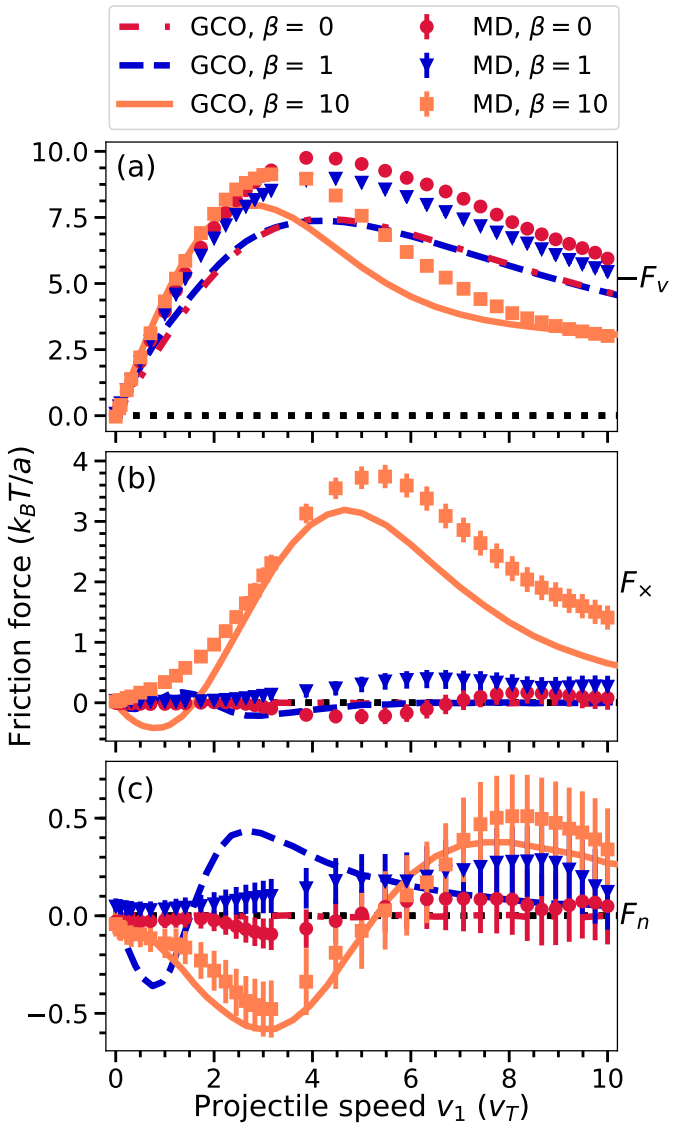

Figure 4.5: Comparison of GCO (lines) and MD (data points) predictions for the friction force components [$-F_v$ in (a), $F_\times$ in (b) and F_n in (c)] at $\Gamma = 10$ and $\theta = 22.5°$ for different magnetization strengths $\beta = 0$, 1 and 10.

$\Gamma = 0.1$ are in the strongly magnetized transport regime and the rest are in the extremely magnetized transport regime as defined in the introduction. This shows the versatility of the GCO to be applicable across a wide range of both Coulomb coupling and magnetization strength regimes. A previous approach [56, 98] based on linear response theory is limited to the strongly magnetized regime because it does not account for strong non-linear interactions that arise in either the extremely

magnetized regime, or the strongly coupled regime.

On comparing the stopping power curves, good qualitative agreement is observed. Features like an increase in magnitude of the force, shift in position of the Bragg peak and broadening of the curves with increasing coupling strength are observed. A good quantitative agreement between theory and MD is observed for small speeds of the projectile, but some quantitative differences emerge at high speeds. This was also observed in unmagnetized plasmas [93]. The larger discrepancy at high speeds may be due to the absence of dynamic screening (velocity-dependent screening) in the potential of mean force used for modeling the binary interactions.

The transverse force curves obtained by the theory also capture the qualitative trends predicted by the MD. Features like an increase in the magnitude of the force and broadening of the curves with increasing coupling strength are observed in both. However, some quantitative differences are observed. The most significant difference is that for coupling strengths $\Gamma = 10$ and $\Gamma = 100$, the theory predicts a change in sign of the transverse force at low speeds, which is not observed in the MD data. This change in sign is a prominent characteristic of the transverse force and is observed when $\Gamma = 0.1$ and $\Gamma = 1$ by both the theory and MD. The GCO calculations predict that the change in sign happens at higher speeds with increasing coupling strength. The cause of this disagreement remains uncertain at this time. Strong magnetization causes particles to move tightly along the field lines and to re-collide multiple times, resulting in increased inter-particle correlations in space and time [99]. These increased correlations increase the time it takes for the plasma to reach hydrodynamic behavior. One possible reason for the discrepancy might be that the strong correlations cause a disconnect between the concept of an "instantaneous" friction force with what is computed over a few plasma period interval in the MD simulations. Such correlations may also violate the molecular chaos approximation used in the generalized collision operator [54] and might be another reason for the discrepancy.

A significant result of this chapter is the prediction of the gyrofriction force component in the direction of the Lorentz force (F_n). Good agreement is found between the theory and the MD across coupling strengths. This component is found to be negligible in the weakly coupled regime and its strength increases with the coupling strength. This prediction shows the ability of the generalized collision operator to accurately capture novel physics arising from the combination of strong magnetization and strong coupling.

The friction force is found to not only depend on the speed of the projectile but also on the orientation of the projectile's velocity with the direction of the magnetic field. Figure 4.4 compares the friction force curves for different orientation of the projectiles velocity with the direction of the magnetic field ($\theta = 0°$, $22.5°$, $90°$, $157.5°$ and $270°$) for the coupling strength $\Gamma = 1$ and the magnetization strength $\beta = 10$. The good agreement with MD shows that the theory can accurately capture the dependence of the friction force components on the orientation of the projectile's velocity.

At strong coupling, the coupling-magnetization parameter space identifying transport regimes is predicted to collapse to two regions - unmagnetized and extremely magnetized. Fixing the coupling strength Γ and changing the magnetization strength β can span these two transport regimes. Figure 4.5 compares the friction force components obtained using MD simulations and theory for magnetization strengths $\beta = 0, 1$ and 10. Here the coupling strength is $\Gamma = 10$ and angle $\theta = 22.5°$. Theory captures the overall trends observed in the MD results. Both predict that strong magnetization causes a shift of the position of the Bragg peak to lower speed and decrease the stopping power at high speeds. The increase in relative magnitude of the transverse force with the increase in magnetization strength is captured by both the theory and MD. However, some quantitative features like the position of the peaks and sign reversal differ. For instance, the theory predicts a sign reversal of the transverse force (once for $\beta = 10$ and twice for $\beta = 1$), which is absent in the MD results. Good agreement

between the theory and MD is seen in the gyrofriction force curve for $\beta = 10$, and both are consistent with zero at $\beta = 0$. However, at the transition magnetization strength ($\beta = 1$), the agreement is poor across the projectile speeds.

4.2.2 Coupling strength and angle

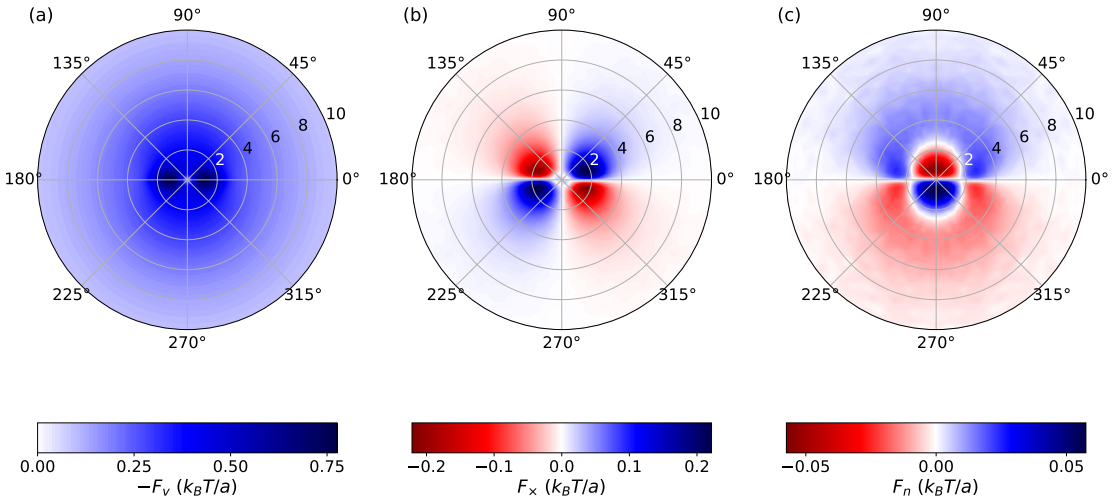

Figure 4.6: Polar plots of the friction force components [$-F_v$ in panel (a), $F_\times$ in panel (b) and F_n in panel (c)] at $\Gamma = 1$ and $\beta = 10$. The radial axis is the speed of the projectile (v_1/v_T) and the angle is the phase angle that the projectile's velocity makes with the direction of the magnetic field (θ).

The friction force exhibits strong dependence on the orientation of the velocity with the direction of the magnetic field. For this reason, an entire polar plot that includes both speed and angle is required to compute the average trajectory of a test charge in a strongly magnetized plasma. Because so many data points are required to solve for this 2D parameter space, it is impractical to obtain this information from MD simulations due to their high computational cost. However, the much lower computational expense of the GCO calculations makes this possible. Polar plots also reveal the symmetry properties of the different friction force components.

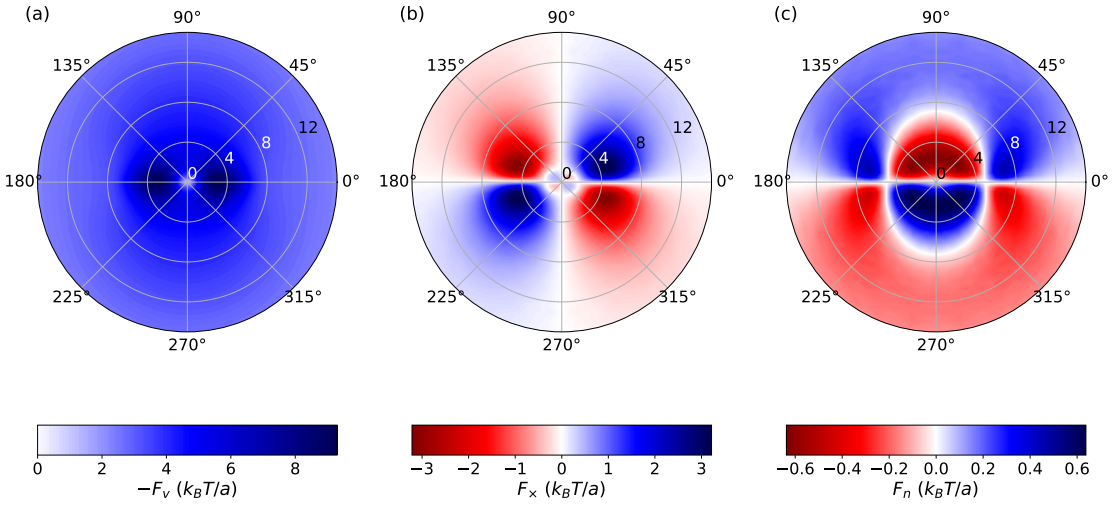

Figure 4.7: Polar plots of the friction force components [$-F_v$ in panel (a), $F_\times$ in panel (b) and F_n in panel (c)] at $\Gamma = 10$ and $\beta = 10$. The radial axis is the speed of the projectile (v_1/v_T) and the angle is the phase angle that the projectile's velocity makes with the direction of the magnetic field (θ).

Figures 4.6, 4.7, and 4.8 show the polar plots of each friction force component for $\beta = 10$ and coupling strengths $\Gamma = 1$, 10 and 100. On comparing these figures, quantitative changes are observed. The magnitude of the friction increases with increasing coupling strength. Panel (a) of figures 4.6, 4.7, and 4.8 show that the stopping power curve broadens and the Bragg peak shifts to higher speed with increasing coupling strength. This trend is similar to that observed in the unmagnetized plasma [77, 93]. The phase angle of the stopping power follows the symmetry: $F_v(\theta) = F_v(\pi - \theta) = F_v(\pi + \theta) = F_v(2\pi - \theta)$ for $0 \leq \theta \leq \pi/2$. This is the same symmetry observed in the weakly coupled transport regime [56]. When θ increases from 0°, the magnitude of the Bragg peak monotonically decreases and reaches a minimum value at 90°. The position of the Bragg peak is observed to shift to lower speed with increasing θ in the first quadrant. Since stopping power is anti-parallel to the velocity of the projectile, these results imply that the energy deposition of the

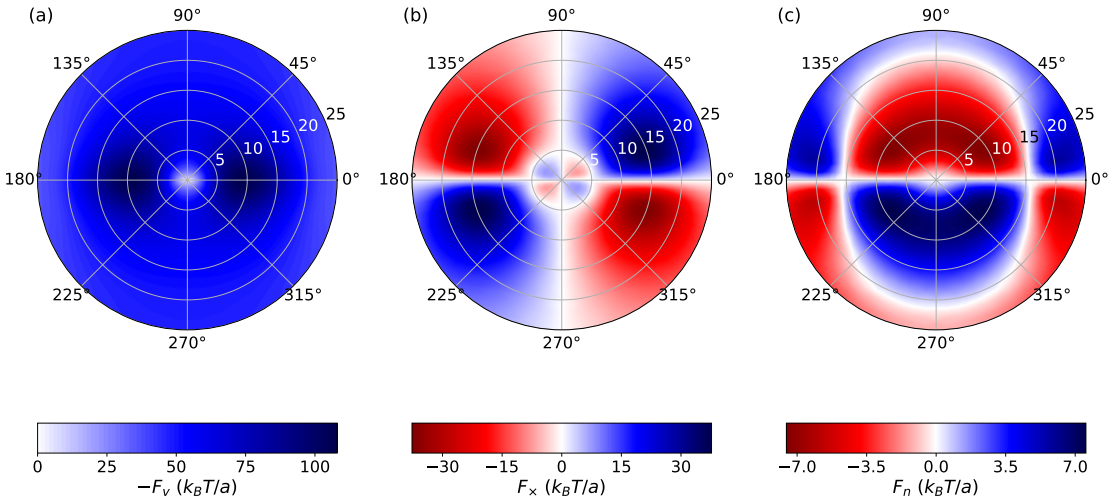

Figure 4.8: Polar plots of the friction force components [$-F_v$ in panel (a), $F_\times$ in panel (b) and F_n in panel (c)] at $\Gamma = 100$ and $\beta = 10$. The radial axis is the speed of the projectile (v_1/v_T) and the angle is the phase angle that the projectile's velocity makes with the direction of the magnetic field (θ).

projectile has a significant dependence on the orientation of the velocity vector.

Panel (b) of figures 4.6, 4.7, and 4.8 show the transverse component of the friction. Similar to the stopping power, both the positive and negative peaks shift to higher speeds and the transverse force curve widens as the coupling strength increases. The prominent sign reversal signature of the transverse force is seen across coupling strengths. The phase angle of the transverse force follows the symmetry: $F_\times(\theta) = -F_\times(\pi - \theta) = F_\times(\pi + \theta) = -F_\times(2\pi - \theta)$ for $0 \leq \theta \leq \pi/2$. This is the same symmetry observed at weakly coupling [56]. Similar to the previous findings, the transverse force is zero when the projectile's motion is parallel or perpendicular to the magnetic field. For a phase angle less than 90°, a positive transverse force increases the gyroradius and a negative transverse force decreases the gyroradius. Thus the transverse force increases the gyroradius of the fast projectile by redirecting the kinetic energy from the parallel direction to the perpendicular direction and de-

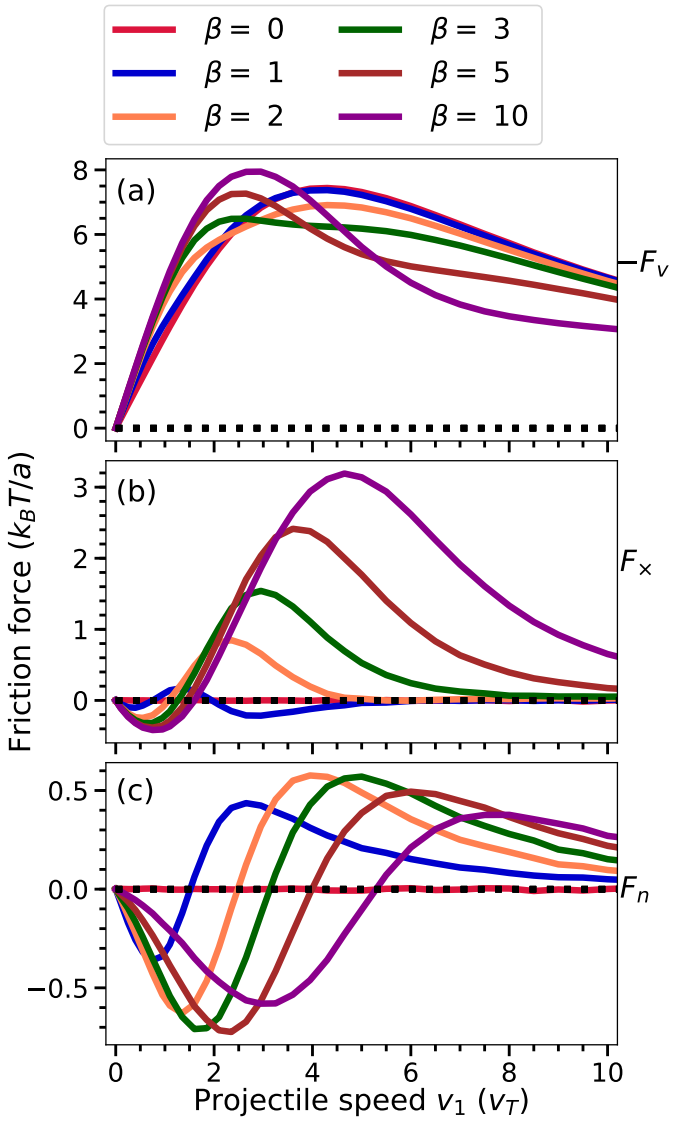

Figure 4.9: Friction force components [$-F_v$ in (a), $F_\times$ in (b) and F_n in (c)] at $\Gamma = 10$ and $\theta = 22.5°$ for different magnetization strengths $\beta = 0$, 1, 2, 3, 5 and 10.

creases the gyroradius of the slower projectile by redirecting the kinetic energy from the perpendicular direction to the parallel direction.

Panel (c) of figures 4.6, 4.7, and 4.8 show the gyrofriction component of the friction force. This component is absent in linear response theory calculations [56, 98], which apply in the weakly coupled regime. The linear response theory inherently assumes that the interactions between the colliding particles are weak and avoids the strong non-linear interactions characterizing close collisions [91]. However, the binary

collision theories are capable of capturing the physics associated with the strong close collisions. This suggests that the F_n component of the friction force is due to close collisions.

The magnitude of the gyrofriction component is found to be smaller than the other two components for all coupling strengths studied. Similar to the transverse force, the sign of the gyrofriction force has a dependence on the speed of the projectile. The critical speed at which the transition occurs is found to depend on the coupling strength. Similar to the other two friction components, the force curve broadens and both the positive and negative peaks shift to higher speeds with the increase in coupling strength. The phase angle of the gyrofriction follows the symmetry: $F_n(\theta) = F_n(\pi - \theta) = -F_n(\pi + \theta) = -F_n(2\pi - \theta)$ for $0 \leq \theta \leq \pi/2$. The gyrofriction is zero when the projectile moves parallel or anti-parallel to the magnetic field ($\theta = 0^\circ$ and $\theta = 180^\circ$). Its magnitude is maximum when the projectile's motion is perpendicular to the magnetic field. For a phase angle less than 90°, a positive sign of the gyrofriction corresponds to an increase in the gyrofrequency of the projectile, whereas a negative sign corresponds to a decrease in the gyrofrequency. Thus, gyrofriction increases the gyrofrequency of a fast projectile and decreases that of a slow projectile.

4.2.3 Magnetization

In order to study how the friction force components change across transport regimes, we compute them for a fixed coupling strength ($\Gamma = 10$) and orientation of the projectile velocity ($\theta = 22.5^\circ$) and change the magnetization strength ($\beta = 0$ to 10). The boundary between the unmagnetized and extremely magnetized transport regimes for $\Gamma = 10$ is at $\beta \approx 0.25$.

Figure 4.9 shows the components of the friction force curves for $\beta = 0, 1, 2, 3, 5$ and 10. The Bragg peak of the stopping power curve shifts to the lower speeds and the magnitude of the Bragg peak increases on moving from the unmagnetized to

the extremely magnetized regime. Careful examination shows that this transition involves 2 stages. A new peak develops at low speed and increases in magnitude with increasing magnetization strength. Simultaneously, the stopping power at high speed decreases. Thus magnetization increases the stopping power of slow projectiles and decreases the stopping power of fast projectiles. This is similar to the weak coupling limit [56].

The transverse force is present only when the plasma is in the extremely magnetized transport regime and its magnitude increases with increasing magnetization strength. For this orientation of the projectile ($\theta = 22.5°$) the positive sign of the transverse force corresponds to a force that acts to increase the gyroradius of the projectile, and the negative sign corresponds to a force that decreases its gyroradius. The curve for $\beta = 1$ predicts two negative dips of very small magnitudes. This prediction is unique to the regime of strong coupling and a transitional magnetic field strength ($\beta \approx 1$). The effect may be associated with the non-monotonic nature of the potential of mean force at strong coupling. The second negative dip disappears with increasing magnetization strength.

The gyrofriction is absent in the unmagnetized regime ($\beta = 0$). For this angle ($\theta = 22.5$), a negative sign of the gyrofriction corresponds to a force that acts to decrease the gyrofrequncy of the projectile, whereas a positive sign corresponds to a force that acts to increase its gyrofrequency. The increase in magnetization strength from $\beta = 1$ to $\beta = 10$, increases and then decreases the magnitude of the peak of the gyrofriction. This is in contrast to $F_\times$ where the magnitude of the peak monotonically increases. However the change in the critical speed at which the gyrofriction changes its direction has a strong dependence on the magnetization strength. The critical speed moves to larger speeds with increasing magnetization strength. This can also be contrast with the transverse force, where the sign change is nearly independent of the magnetization strength (β).

4.3 Physical interpretation of gyrofriction

A qualitative description of the physical origin of stopping power and transverse force from the binary collision perspective was provided in chapter III. Although that chapter concentrated on the weakly coupled regime, the qualitative explanations carry over to the strongly coupled regime. Here, we give a qualitative description of the physical origin of the gyrofriction.

Gyrofriction is only observed in the strongly coupled strongly magnetized regime. When the plasma is strongly coupled, the screening distance reduces and close collisions become more relevant. Gyrofriction is also absent in the linear response calculations, which ignores close collisions. These suggest that gyrofriction is associated with close collisions. Binary collision theory obtains the friction force by summing the change in momentum of the projectile from all possible binary scattering events.

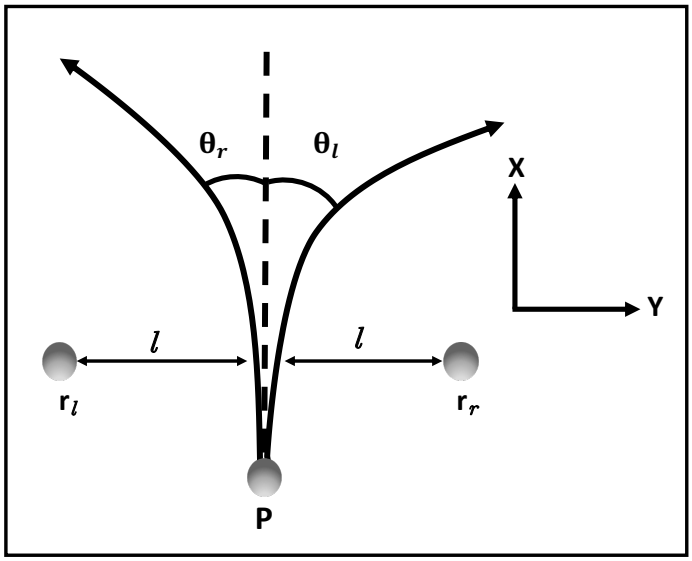

Figure 4.10: Illustration of a collision between a projectile particle (p) and a background particle starting with a y position a distance l to the left of the projectile ($\mathbf{r}_l$, case 1), or with a y position a distance l to the right of the projectile ($\mathbf{r}_r$, case 2). If the associated scattering angles balance ($\theta_l = \theta_r$) the net force along y is zero and there is no net gyrofriction force. If $\theta_l \neq \theta_r$, a net gyrofriction force is expected.

In order to have a clearer qualitative description, consider the interaction of the test charge (projectile) and a background particle in 2D, corresponding to the situa-

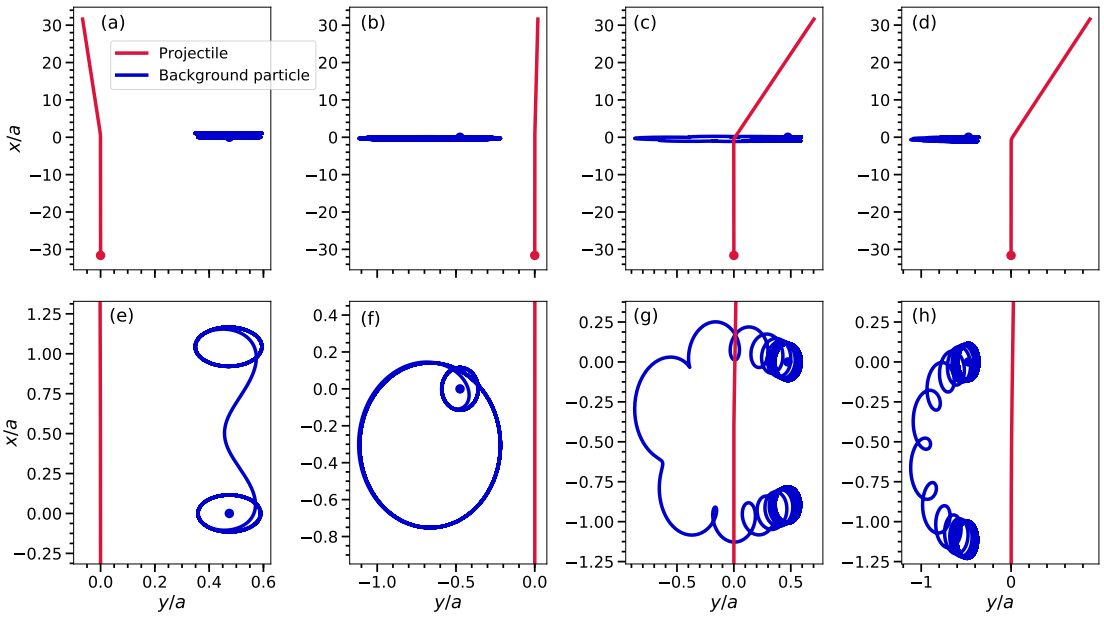

Figure 4.11: Trajectories of the projectile (red) and the background plasma particle (blue) during a Coulomb collision in the 2D plane perpendicular to $\mathbf{B} = B\hat{\mathbf{z}}$. Panels (a), (b), (e) and (f) show the case of a fast projectile ($v_1 = 1v_T$) and panels (c), (d), (g) and (h) are for a slow projectile ($v_1 = 0.1v_T$). The bottom panels show the zoomed in view of the top panels. The initial speed of the background particle is taken as ($0.2v_T$, $0.2v_T$, 0) and the initial position (red dot) of the projectile is at ($-32a$, 0, 0). The initial guiding center position (blue dot) of the background particles are (0, $0.5a$, 0) [(a), (e), (c), (g)] and (0, $-0.5a$, 0) [(b), (f), (d), (h)]. The trajectories shown are binary interactions occurring via the Debye-Hückel potential for $\Gamma = 1$, which is an excellent approximation of the potential of mean force at this conditions, and the Lorentz force is modeled using $\beta = 2$.

tion of both the particles in a plane perpendicular to the magnetic field; see Fig. 4.10. The projectile has an initial velocity in the $+\hat{\mathbf{x}}$ direction. Consider two example interactions: (1) a background particle that starts a distance l to the left of the initial projectile position ($\mathbf{r}_l \cdot \hat{\mathbf{y}} = -l$), and (2) a background particle that starts a distance l to the right of the initial projectile position ($\mathbf{r}_r \cdot \hat{\mathbf{y}} = l$). The interaction deflects the projectile from its initial trajectory by an angle θ_l in case (1), and θ_r in case (2). In an unmagentized plasma $\theta_l = \theta_r$, so the momentum exchanged in the $\hat{\mathbf{y}}$ direction in case (1) cancels the momentum exchanged in the $\hat{\mathbf{y}}$ direction in case (2). Since the net force on the projectile is the result of all of the possible collisions with the back-

ground, and because each particle at a position $\mathbf{r}_l$ will have a partner at a position $\mathbf{r}_r$, this symmetry results in no net gyrofriction force.

This symmetry is broken when the plasma is strongly magnetized because the deflection angles become unequal ($\theta_l \neq \theta_r$), as illustrated in Fig. 4.11. Here, the magnetic field is in the $+\hat{\mathbf{z}}$ direction and the charge of the particles is positive, so the background particles gyrates in the counterclockwise direction. The initial velocity of the projectile is in the $\hat{\mathbf{x}}$ direction, thus $\hat{\mathbf{n}} = -\hat{\mathbf{y}}$. The initial position of the projectile is $(-32a,\ 0,\ 0)$, and the initial guiding center position of the background particle in case (1) is $(0,\ -0.5a,\ 0)$ and in case (2) is $(0,\ 0.5a,\ 0)$. A net gyrofriction force results when the component of momentum exchanged in the $\hat{\mathbf{n}}$ direction from case (1) does not balance that in case (2). The dominant symmetry breaking process is observed to depend on the speed of the projectile. At sufficiently high speed it is associated with the strength of the relative velocity between the projectile and background particle when they are closest together (most strongly interacting), which is asymmetric because the gyromotion causes the velocity vector of the background particle to be either aligned with the projectile (case 1), or antialigned (case 2). At sufficiently low projectile speed, the dominant symmetry breaking mechanism is an $\mathbf{E} \times \mathbf{B}$ drifting motion of the background particle. Each process is found to lead to a different sign of the gyrofriction and the sign change is associated with the transition from one process dominating over the other.

First, consider the interaction of a fast projectile with a thermal background particle; as shown in panels (a), (b), (e) and (f) of Fig. 4.11. When the background particle starts to the right of the projectile (case 2; panels (a) and (e)), the collision deflects the projectile in the $-\hat{\mathbf{y}}$ direction. In contrast, when the background particle starts to left of the projectile (case 1; panels (b) and (f)), the collision deflects the projectile in the $+\hat{\mathbf{y}}$ direction. However, the momentum transfer is greater in case 2 than in case 1, resulting in different scattering angles, $\theta_l \neq \theta_r$. Since $\theta_r > \theta_l$, this

asymmetry produces a net force in the $-\hat{\mathbf{y}}$ direction, which is the $+\hat{\mathbf{n}}$ direction, leading to a positive sign of the gyrofriction at high speed. The reason for the asymmetry is that the relative velocity between the projectile and background particle is higher in case (2) than in case (1). Within the region of closest approach, where the interaction is strongest, the interaction is head-on in case (2). In contrast, in case (1) the $\hat{\mathbf{x}}$ component of the velocity of both particles is positive at closest approach. The higher relative velocity in the head-on collision causes a greater momentum transfer. Any $\mathbf{E} \times \mathbf{B}$ motion is negligible in this case because the collision time is too short for the background particle to exhibit an $\mathbf{E} \times \mathbf{B}$ drift when the projectile speed is large.

In contrast, panels (c), (d), (g) and (h) of Fig. 4.11 show the collision of a slow projectile with a thermal particle of the background plasma. At these conditions, the projectile is observed to deflect to the right ($+\hat{\mathbf{y}}$ direction) whether it starts to the right or left of the background particle. The reason for this qualitative difference is that when the projectile approaches slowly, the background particle has enough time to $\mathbf{E} \times \mathbf{B}$ drift in a counterclockwise orbit around the projectile (it sees an almost static electric field from the projectile at the timescale of the gyromotion). This leads to a situation where, even though the background particle starts to the right of the projectile (case 2), the $\mathbf{E} \times \mathbf{B}$ drift takes it to the left side of the projectile for a large fraction of the time interval over which the particles interact strongly. This results in momentum transfer in the $+\hat{\mathbf{y}}$ direction for case (2). In case (1), when the background particle starts to the left of the projectile, there is still a counterclockwise $\mathbf{E} \times \mathbf{B}$ drift as shown in the panels (d) and (h). However, the drift is not as pronounced in this case because it acts to shorten the interaction time between the particles by deflecting the background particle behind the projectile. For this reason, the background particle remains on the left side of the projectile for the entire interaction, and the net force is in the $+\hat{\mathbf{y}}$ direction. Thus, for a slow projectile both cases act to transfer momentum in the $+\hat{\mathbf{y}}$ direction, so the net gyrofriction is also in the $+\hat{\mathbf{y}}$ direction (which is the

$-\hat{\mathbf{n}}$ direction).

The critical speed at which the gyrofriction changes sign can be estimated by comparing the interaction timescale (τ_c) to the gyroperiod of the background particle ω_c^{-1}. The interaction timescale is set by the ratio of the interaction length and the speed of the projectile: $\tau_c \sim l/v_1$. The interaction length (l) is approximately characterized by λ_D in the weakly coupled regime, and a in the strongly coupled regime. If $\tau_c \gtrsim \omega_c^{-1}$, then the background particle undergoes complete gyro-orbits during the collision and can thus exhibit $\mathbf{E} \times \mathbf{B}$ drifting motion. Note that gyration during a collision also requires that $r_c < l$, where l is the interaction range, but we are already assuming that this condition is met ($\beta > 1$) and concentrating here on the dependence on the projectile speed. In this sense, it defines a speed-dependent parameter to characterize strong magnetization when $v_1 > v_T$. The condition $\tau_c > \omega_c^{-1}$ is satisfied when the projectile is sufficiently slow

$$\frac{v_1}{v_T} \lesssim \frac{l\omega_c}{v_T} \approx \frac{l}{\lambda_D}\beta. \tag{4.3}$$

When this is satisfied, the $\mathbf{E}\times\mathbf{B}$ drift is expected to cause F_n to be in the $-\hat{\mathbf{n}}$ direction. In contrast, when $v_1/v_T \gtrsim l\omega_c/v_T \approx (l/\lambda_D)\beta$ the interaction time is too short for $\mathbf{E}\times\mathbf{B}$ motion to occur, and we expect the net gyro force to be in the $+\hat{\mathbf{n}}$ direction. The expectation that this transition speed increases proportionally with β is consistent with the trend observed in panel (c) of Fig. 4.9. Considering strong coupling effects, the interaction range scales as $l/\lambda_D \approx a/\lambda_D = \sqrt{3}\Gamma^{1/2}$. The prediction that the critical speed increases proportionally to $\Gamma^{1/2}$ in the strongly coupled regime also appears consistent with the data shown in panel (c) of Figs. 4.6–4.8.

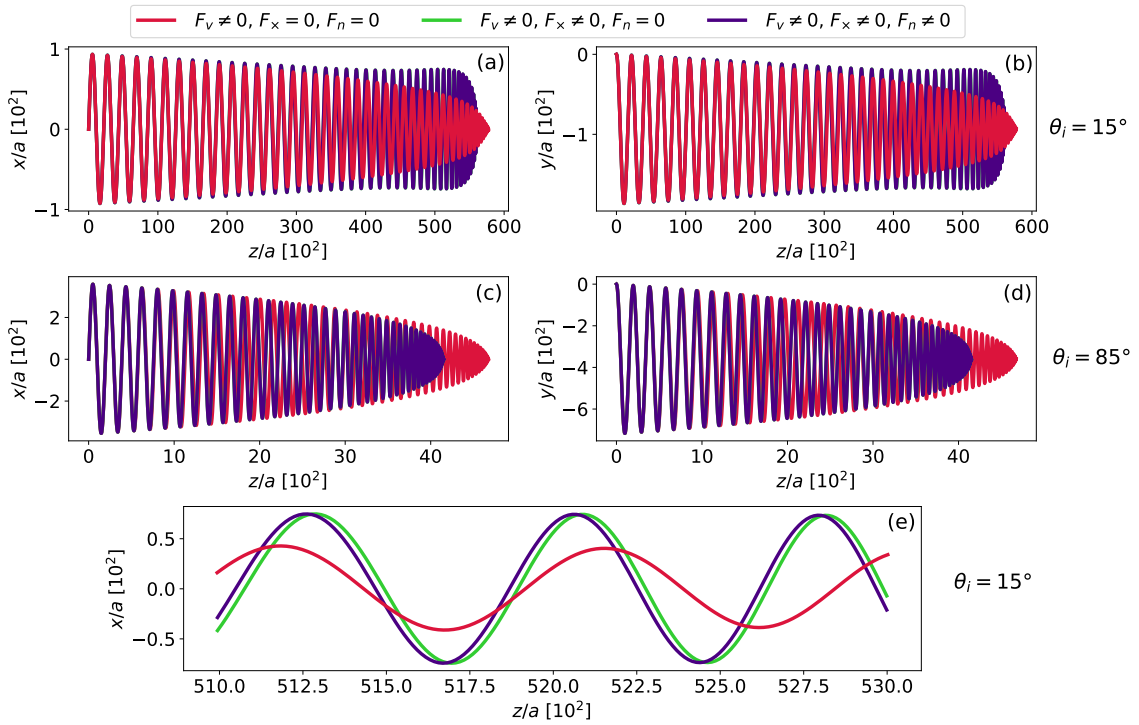

Figure 4.12: Trajectories of a massive projectile ($m_r = 1000$) with initial speed $14v_T$ moving through a one component plasma with coupling strength $\Gamma = 10$ and magnetization strength $\beta = 10$. The initial orientation of the velocity with respect to the magnetic field is $\theta_i = 15°$ (panel (a), (b) and (e)) and $\theta_i = 85°$ (panel (c) and (d)).

4.4 Trajectories

The average motion of a projectile in a plasma is influenced by the Lorentz force and the friction force. Thus, the equations of motion can be written as

$$m_t \frac{d\mathbf{v}}{dt} = q(\mathbf{v} \times \mathbf{B}) + \mathbf{F}. \tag{4.4}$$

Although the trajectory of an individual particle is influenced by diffusive motion resulting from interactions with other particles, Eq. (4.4) describes the expected trajectory resulting from the average of many sample individual trajectories. In order to study the effects of the various friction force components on the motion of a projectile through the plasma, we solve Eq. (4.4) including each of the three vector

components of **F** shown in the polar plot Fig. 4.7. Figure 4.12 shows the resulting trajectory of a projectile moving in a background plasma characterized by $\Gamma = 10$ and $\beta = 10$. The projectile starts at the origin with an initial speed of $v = 14v_T$. The initial velocity is $v_z = v\cos\theta_i$, $v_x = v\sin\theta_i$, $v_y = 0$ and initial orientation with respect to the magnetic field is $\theta_i = 15^\circ$ (panel (a), (b) and (e)) and $\theta_i = 85^\circ$ (panel (c) and (d)). Here the magnetic field direction is taken along the $\hat{\mathbf{z}}$ direction. The trajectories are calculated for three different scenarios to emphasize the importance of different friction components: 1) includes the stopping power ($F_v \neq 0$), but excludes the transverse and gyrofriction components ($F_\times = 0$ and $F_n = 0$) (red line). 2) includes the stopping power ($F_v \neq 0$) and transverse force ($F_\times \neq 0$), but excludes the gyrofriction component ($F_n = 0$) (green line). 3) includes all the three components ($F_v \neq 0$, $F_\times \neq 0$ and $F_n \neq 0$) (blue line). The green and blue lines are only separated by a small phase shift and appear overlapping in panels (a) – (d). Panel (e) zooms into the phase shift.

Out of the three components of the friction force, only stopping power decreases the kinetic energy of the projectile. It acts opposite to the motion of the projectile and reduces both the parallel and perpendicular kinetic energy. This results in a monotonic decrease in the gyroradius of the projectile (red line in Fig. 4.12). The transverse force is perpendicular to the velocity of projectile and does not influence its total kinetic energy. However, it influences the gyroradius by redirecting parallel speed to perpendicular speed, or vice-versa (green line). For larger speeds, the transverse force is positive and it increases the gyroradius, whereas for smaller speeds, it is negative and decreases the gyroradius. This effect is prominent in the case of $\theta_i = 15^\circ$. Here, the gyroradius increased for most of the motion and steeply decreased near the stopping point after the projectile speed had dropped sufficiently that the transverse force changed sign.

The transverse force also changes the stopping distance of the projectile. It is

not a prominent effect at $\theta_i = 15°$, but is well demonstrated by the $\theta_i = 85°$ initial condition. In this scenario, the initial parallel speed is very low compared to previous scenario leading to a smaller stopping distance. But the transverse force strongly alters its trajectory by decreasing the parallel speed, resulting in a significantly shorter stopping distance.

The gyrofriction force is in the direction of the Lorentz force and is observed to create a small phase shift in the motion of the projectile; see panel (e) in Fig. 4.12. For larger speeds, the gyrofriction is positive and it increases the gyrofrequency and for smaller speeds it is negative and decreases the gyrofrequency. The effect of gyrofriction in the overall evolution of the projectile is not as prominent as the transverse force or stopping power. This can be deducted by writing the equations of motion using the scaled variables in spherical polar coordinates. On scaling the velocity using v_T, friction by k_BT/a and time using ω_p, we get

$$\frac{d\tilde{v}}{d\tilde{t}} = \frac{\tilde{F}_v}{\sqrt{6\Gamma}m_r}, \tag{4.5a}$$

$$\frac{d\theta}{d\tilde{t}} = \frac{\tilde{F}_\times}{\sqrt{6\Gamma}m_r\tilde{v}}, \tag{4.5b}$$

$$\frac{d\phi}{d\tilde{t}} = -\frac{\beta}{m_r} - \frac{\tilde{F}_n}{\sqrt{6\Gamma}m_r\tilde{v}\sin\theta}. \tag{4.5c}$$

Here, the variables with tilde ($\tilde{}$) on top represents scaled variables, θ is the polar angle which is same as the orientation of the projectile's velocity with the direction of the magnetic field and ϕ is the azimuthal angle. On comparing the magnitude of the terms in the Eq. (4.5c), the $\tilde{F}_n$ term is 10^3 - 10^4 times smaller than the β term. On the other hand, other friction force components do not have any external force to compete with in the equations of motion. This explains the small effect of the gyrofriction component in the trajectories of the projectile compared to other two components.

The overall movement of the projectile inside the plasma is primarily determined

by the combined effect of both the stopping power and the transverse force. The effect of the gyrofriction is comparatively weak because it competes with the large Lorentz force. However, the gyrofriction may influence other macroscopic transport or wave properties by changing the gyration rates.

CHAPTER V

Barkas Effect in Strongly Magnetized Plasmas

5.1 Introduction

Conventional plasma theories obey a fundamental symmetry that the collision rate is independent of the sign of the charge of interacting particles [100]. Thus the transport coefficients remain the same if electron-ion interactions are modeled as positron-ion interactions. In this chapter, we show that this symmetry is broken when the plasma is strongly magnetized.

This charge-sign asymmetry in collision rates is often referred to as the "Barkas effect" [101]. The Barkas effect was first observed in emulsion experiments, where differences between the stopping power of positive mesons and negative mesons were observed [101]. These differences were attributed to the atomic screening from the bound electrons in the emulsion medium [101, 102, 103, 104]. The Barkas effect has also been observed and studied in plasmas [18, 105]. In plasmas, the effect arises from differences in the trajectories of oppositely-charged versus like-charged particles when interacting through a screened potential rather than the Coulomb potential. Interaction through a screened potential results in a larger momentum transfer cross section for oppositely-charged collisions compared to like-charged collisions. Deviations between these cases become greater as the scattering angle increases. The Barkas effect is therefore more prominent in low-speed interactions than high-speed interactions.

Likewise, the Barkas effect is greater in strongly coupled plasmas than in weakly coupled plasmas because large-angle collisions are more frequent [18, 19, 105]. In each case studied so far in this thesis, the sign of the charge of the test charge was the same as the background particles it interacts with (++). This chapter explores how changing the test charge's sign affects the friction force (+−). It is found that the components of the friction force in the oppositely-charged (+−) case are both qualitatively and quantitatively different than the like-charged (++) case. The friction force on a single test charge is the basis for more complex macroscopic transport phenomena. Alterations in the friction by strong magnetization and the sign parity of the interacting particles translates to alterations of macroscopic transport properties. To demonstrate this, we compute the electrical resistivity tensor from the friction force curves using the first order moment method. When considering like-charged interactions, strong magnetization is observed to increase both the parallel and perpendicular resistivity. This result is similar to what was observed in a recent calculation using linear response theory [106]. However, the linear response approach only models long-range interactions, and therefore does not predict the Barkas effect which arises from higher order terms corresponding to short-range physics [56, 98]. Opposite-charged interactions are then considered, where the Barkas effect in combination with strong magnetization are observed to both decrease the parallel resistivity and increase the perpendicular resistivity by almost an order of magnitude (for $\Gamma = 1$ and $\beta = 10$ conditions). These results can be used to model the resistivity in ultra-cold-neutral plasma experiments [8, 24] with a strong magnetic field and can be extended to calculate other transport properties. This chapter is based on Ref. [72].

5.2 Theory

The friction force on the test charge is obtained by solving Eq. (4.2). The difference in evaluating the friction force integral for the +− case compared to the ++ case

described in the previous chapters comes into the equations of motion of the colliding particles inside the collision volume.

$$(m_1 + m_2)\frac{d\mathbf{V}}{dt} = e\Big(\frac{\mathbf{V}}{c} \times \mathbf{B}\Big) - \frac{e\, m_{12}}{m_2}\Big(\frac{\mathbf{u}}{c} \times \mathbf{B}\Big), \tag{5.1a}$$

$$m_{12}\frac{d\mathbf{u}}{dt} = -[\pm\nabla\phi(r)] + \frac{e\, m_{12}^2}{m_2^2}\Big(\frac{\mathbf{u}}{c} \times \mathbf{B}\Big) - \frac{e\, m_{12}}{m_2}\Big(\frac{\mathbf{V}}{c} \times \mathbf{B}\Big). \tag{5.1b}$$

The interaction potential for the oppositely charged test charge is taken as the negative of the potential of mean force of the like charged case [18]. In the equations of motion [Eqs. (5.1a) and (5.1b)], the plus (+) sign of the potential is for the like-charged case and the minus (−) is for the opposite-charged case. The difference in the interaction potential alters the trajectories of the particles during the Coulomb collisions. In a like-charged collision, the particles do not get too close because of Coulomb repulsion. However, for an opposite-charged collision, the particles get very close, sometimes forming a pseudo-bound state and interacting for a long time before ending in the post-collision free state. This contrast in the trajectories causes the difference in the momentum exchanged during the collisions leading to the Barkas effect.

Numerical evaluation of the friction force integral, Eq. (4.2), was the same as that described in chapters III and IV. The χ factor [97] for attractive collisions have not been formally derived. For this reason, the χ factor is only used in the case of repulsive interactions.

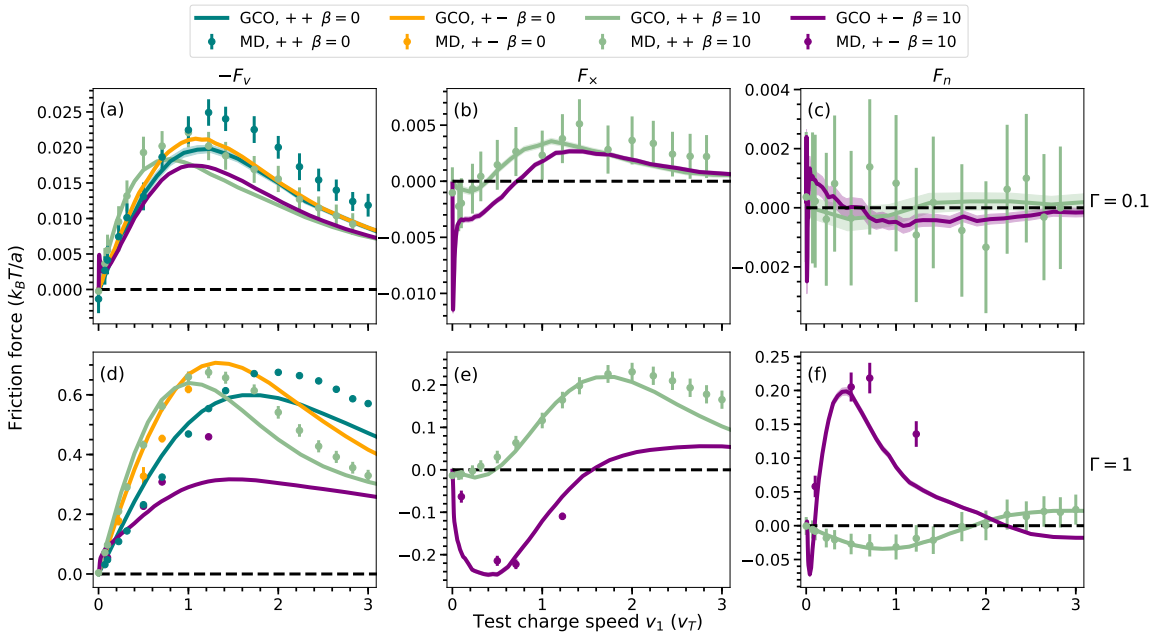

Figure 5.1: Friction force components $[-F_v,\ F_\times$ and $F_n\ ]$ of the like-charged $(++)$ and opposite-charged $(+-)$ cases for coupling strengths $\Gamma = 0.1$ [(a), (b) and (c)] and $\Gamma = 1$ [(d), (e) and (f)] and magnetization strength $\beta = 10$ and $\beta = 0$. The orientation of the test charge is $\theta = 22.5°$.

5.3 Results

5.3.1 Comparison with molecular dynamics simulations

Figure 5.1 shows that the GCO and MD results generally agree, but have some quantitative differences. Features like shifting of the Bragg peak, increase in magnitude and broadening of the curves due to strong magnetization are observed in both. Although transverse and gyrofriction curves from theory are in good agreement with MD results, small quantitative differences are observed for stopping power curves at high speeds, especially in the case of oppositely-charged interaction. The difference is seen particularly above the Bragg peak. One source of deviation may be the lack of an Enskog model for the collision rate enhancement factor (χ) for oppositely-charged interactions. Another possibility may be the lack of dynamic screening in the potential of mean force used to model the binary interactions in the theory. The latter effect has been shown in previous work to be most significant at speeds above the

Bragg peak [93], which is where the largest disagreements are observed.

In an unmagnetized plasma ($\beta = 0$), the friction force has only a stopping power component. The Barkas effect is more prominent at $\Gamma = 1$ than $\Gamma = 0.1$, which is expected to be due to the increased screening effect and associated large-angle collisions at higher coupling strengths [18]. The stopping power is larger for the opposite-charged case at low speeds but has the same value as the like-charged case at high speeds. This is because the turning points in trajectories of particles with low relative speeds occur at larger distances, where screening is most important, so the oppositely charged collisions deviate from like charged collisions at low speeds only [18].

When the plasma is strongly magnetized ($\beta = 10$), the Bragg peak of the stopping power curve for the opposite-charged case is less than the like-charged case. This is opposite to what was observed without a magnetic field, where the magnitude of the Bragg peak increased. Similar to the case of unmagnetized plasma, the two curves merge at high speeds. A similar effect was observed in experiments on electron cooling [11, 107, 108] where there was a reduction of the stopping power when an ion interacted with a magnetized beam of electrons [109]. One of the most apparent observations is that the magnitude of the peak of the transverse and gyrofriction components are significantly larger for the opposite-charged case. This contrasts with the stopping power. In fact, the peak magnitude of the gyrofriction increases to such an extent that it becomes comparable in magnitude to the transverse force when $\Gamma = 1$. For comparison, gyrofriction is an order of magnitude smaller than the transverse force in the like-charge case. Similar to the stopping power, the transverse friction force curves merge at high speeds. The gyrofriction force curves are found to have the same magnitude but opposite signs at large speeds.

In the oppositely charged cases, attractive interactions sometimes lead to the formation of a pseudo bound state in which the less massive background particle

revolves around the ion for a long time before ending in post-scattering state. These interactions are more frequent when the test charge speed is low. This might be the reason behind the sharp features of the friction force curves of the oppositely charged test charge at small speeds. The magnitude of the friction force curves at low speeds are proportional to the electrical resistivity [106]. This difference in magnitude due to the Barkas effect suggests a significant modification of Ohm's law for the ion-electron collisions in strongly magnetized plasmas, [8, 106], which will be discussed further in Sec. 5.4.

5.3.2 Coupling strength and angle

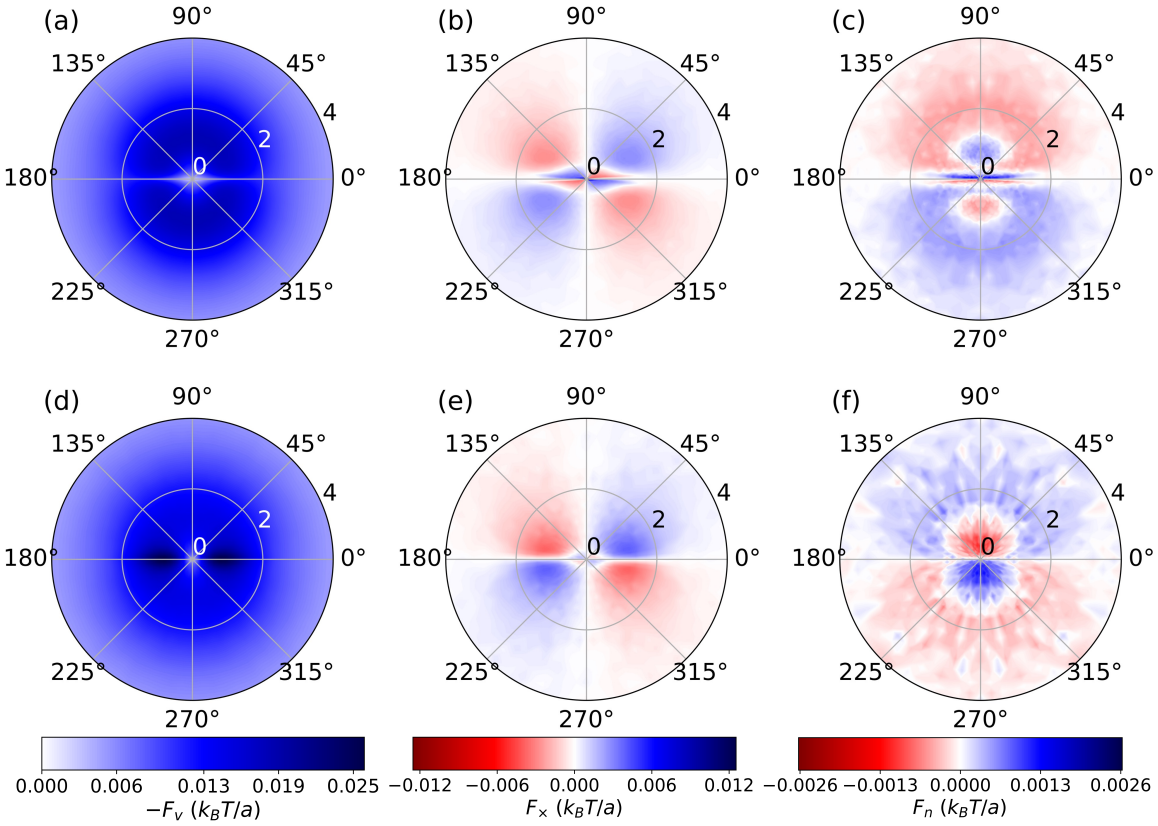

Figure 5.2: Polar plots of the friction force components ($-F_v$, $F_\times$ and F_n) in the opposite-charged case (+−) [(a), (b) and (c)] and like-charged case (++) [(d), (e) and (f)] at $\Gamma = 0.1$ and $\beta = 10$. The radial axis is the speed of the test charge (v_1/v_T) and the angle is the phase angle that the test charge's velocity makes with the direction of the magnetic field (θ).

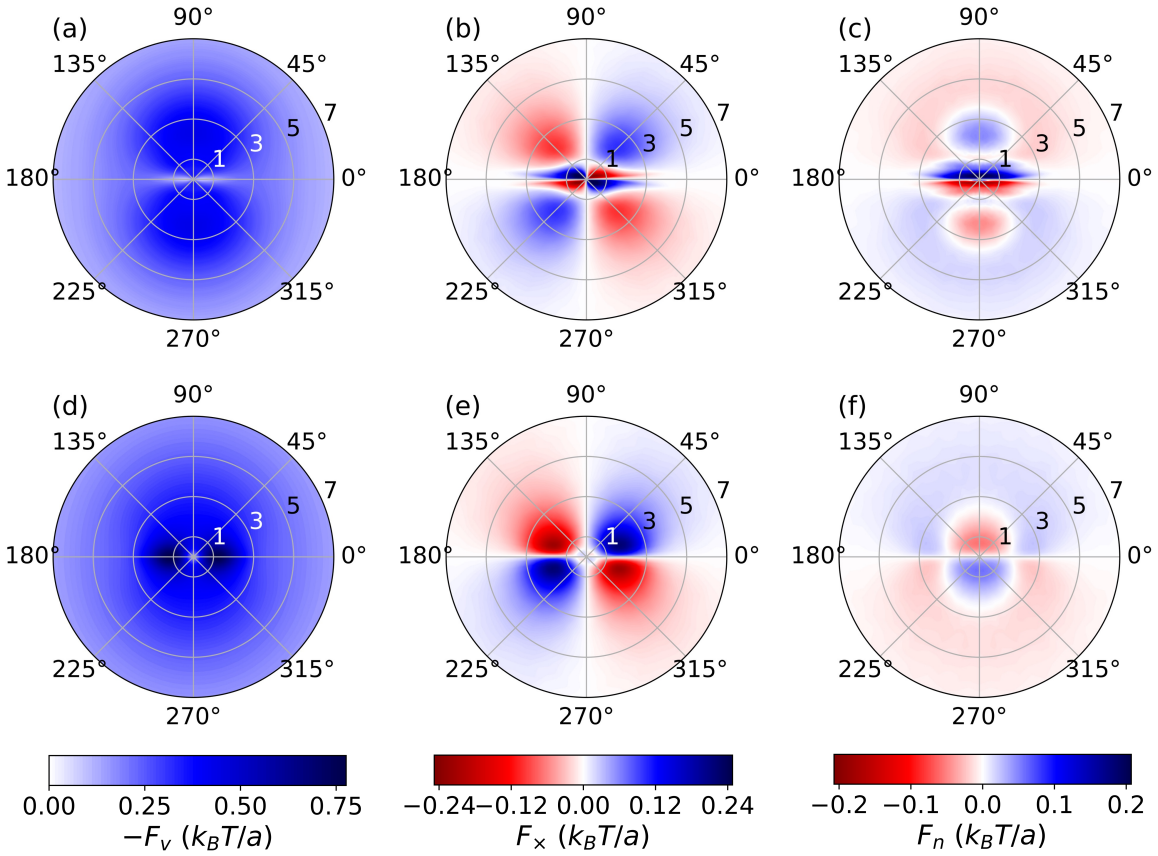

Figure 5.3: Polar plots of the friction force components ($-F_v$, $F_\times$ and F_n) in the opposite-charged case (+−) [(a), (b) and (c)] and like-charged case (++)[(d), (e) and (f)] at $\Gamma = 1$ and $\beta = 10$. The radial axis is the speed of the test charge (v_1/v_T) and the angle is the phase angle that the test charge's velocity makes with the direction of the magnetic field (θ).

The friction force in a strongly magnetized plasma is found to depend on the orientation of the test charge with the direction of the magnetic field, in addition to its speed. In order to study this, we compute polar plots that include both the orientation and speed using GCO. We compare these for the like and opposite charge cases to understand how the Barkas effect modifies the friction; see Figs. 5.2 and 5.3. The polar plots show symmetries of the friction force components with the direction of the magnetic field. Obtaining these polar plots with MD simulations is impractical due to high computational cost, so we rely on GCO calculations for this.

Panels (a) and (d) of Figs. 5.2 and 5.3 show the stopping power. The most

apparent Barkas effect is that the maximum of the Bragg peak occurs at perpendicular incidence ($\theta = 90°$) in the opposite-charge ($+-$) case, whereas it occurs at parallel incidence ($\theta = 0°$) in the like-charge ($++$) case. For opposite-charges, the magnitude of the Bragg peak increases monotonically from $\theta = 0°$ and reaches a maximum value at $\theta = 90°$. This is in contrast to the like-charged case where the magnitude of the Bragg peak monotonically decreases from $\theta = 0°$ and reaches minimum at $\theta = 90°$. In fact, some previous models predict that the stopping power vanishes for parallel incidence ($\theta = 0°$) in the strongly magnetized regime [109]. Our model predicts a reduction of the stopping power by approximately a factor of two compared to perpendicular incidence ($\theta = 90°$); a non-zero value that is of the same order as other angles of incidence. Since stopping power is anti-parallel to the velocity of the test charge, this implies that an opposite-charged test charge loses more energy when it moves perpendicular to the magnetic field, whereas as a like-charged test charge loses more energy when it moves parallel to the magnetic field. These results imply that the energy deposition by the test charge in a strongly magnetized plasma has significant dependence on the sign of its charge, as well as the orientation of the test charge velocity with respect to the magnetic field.

Comparing Figs. 5.2 and 5.3 shows that increasing coupling strength broadens the stopping power curve and causes the Bragg peak to shift to a higher speed. The magnitude of the stopping power for the opposite-charged case is generally smaller than the like-charged case, except at very low speeds. The phase angle of the stopping power follows the same symmetry in both cases: $F_v(\theta) = F_v(\pi - \theta) = F_v(\pi + \theta) = F_v(2\pi - \theta)$ for $0 \leq \theta \leq \pi/2$.

The transverse force doesn't change the overall kinetic energy of the test charge, but it deflects kinetic energy from the parallel direction to perpendicular when its sign is positive and from perpendicular to parallel when its sign is negative (this statement refers to the sign of the force in the first quadrant, $0 \leq \theta \leq \pi/2$) [56].

These effects can significantly alter the trajectories of the test charge and can lead to non-intuitive effects such as an increase in the gyroradius of the test charge as it slows down; see Sec. 4.4. Panels (b) and (e) of Figs. 5.2 and 5.3 show the transverse force component. The magnitude of the negative dip of the transverse force is much larger for $+-$ case than that of the $++$ case. This large negative dip of the transverse force at slow speeds results in a sharp decrease of the gyroradius of the test charge near its stopping point by deflecting kinetic energy from perpendicular direction to parallel. The phase angle of the transverse force for the $++$ and $+-$ cases follow the same symmetry: $F_\times(\theta) = -F_\times(\pi - \theta) = F_\times(\pi + \theta) = -F_\times(2\pi - \theta)$ for $0 \leq \theta \leq \pi/2$.

A finite gyrofriction component causes a phase shift in the trajectories of the test charge; see Sec. 4.4. However, its influence on the overall trajectory is not as prominent as the transverse and stopping power components because it competes with the Lorentz force, which is large in the strongly magnetized regime. Even though its effect is small for a single particle trajectory, how it manifests in macroscopic transport coefficients has yet to be investigated. Panels (c) and (f) of Figs. 5.2 and 5.3 show the gyrofriction component. The $++$ and $+-$ cases follow the same symmetry: $F_n(\theta) = F_n(\pi - \theta) = -F_n(\pi + \theta) = -F_n(2\pi - \theta)$ for $0 \leq \theta \leq \pi/2$. The gyrofriction in the $+-$ case at high speeds is observed to have opposite sign to that of the $++$ case, but with approximately the same magnitude.

5.3.3 Magnetization

In this section we study the dependence of the friction force components on the magnetization strength. This is done by fixing the coupling strength at $\Gamma = 1$ and orientation of the test charge at $\theta = 22.5^\circ$ and varying β. Results are shown in Fig. 5.4. With increasing magnetization strength, the magnitude of the Bragg peak decreases. This is in contrast to the like-charged case where the magnetization was found to increase the magnitude of the Bragg peak (Subsec. 4.2.3). A consequence is

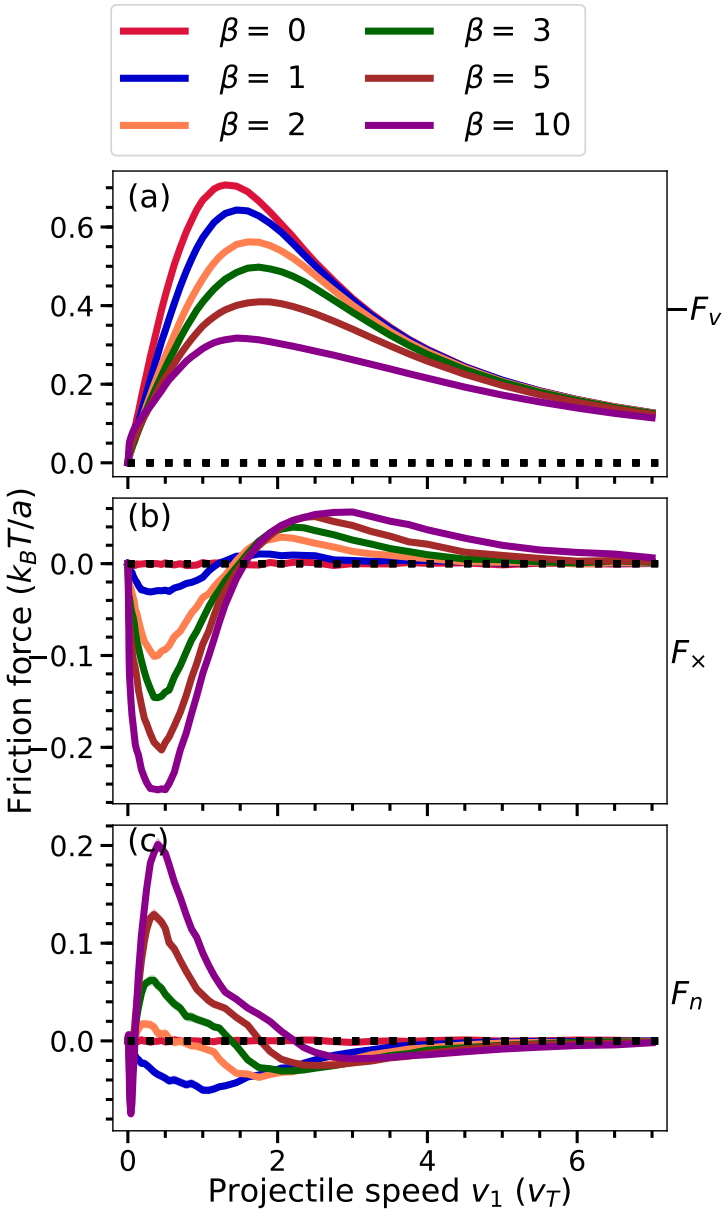

Figure 5.4: Friction force components [$-F_v$ in (a), $F_\times$ in (b) and F_n in (c)] for an opposite-charged test charge at $\Gamma = 1$, $\theta = 22.5°$.

that the Barkas effect decreases the energy deposition rate at strong magnetization.

The transverse force is zero when $\beta = 0$ and its magnitude increases with increasing magnetization strength. The increase in the magnitude of the negative dip at lower speeds is much more prominent than the increase of the magnitude of the positive rise at higher speeds. For this orientation of the test charge ($\theta = 22.5°$), the

positive sign corresponds to a force that increases the gyroradius and negative sign corresponds to a force that decreases the gyroradius. Thus at high magnetization, test charge's trajectory at low speeds will be strongly influenced by the diversion of kinetic energy from the perpendicular direction to the parallel direction.

The gyrofriction is zero when the magnetization is zero and increases in magnitude with increasing magnetization strength. For this orientation of the test charge ($\theta = 22.5°$), the positive sign of the gyrofriction corresponds to a force that increases the gyrofrequency of the test charge and the negative sign corresponds to a force that decreases the gyrofrequency of the test charge. The physical origin of the gyrofriction at low speeds is due to the $\mathbf{E} \times \mathbf{B}$ drift motion of the background particle around the test charge during the interaction (Sec. 4.3). At high speeds, it is due to the close interaction between the gyrating background particle and the test charge. These two mechanisms act in opposite directions, so they have opposite signs. As the speed of the projectile increases the interaction time decreases, changing the dominant mechanism from $\mathbf{E} \times \mathbf{B}$ drift to close interaction. The critical speed at which the sign change happens is proportional to the magnetization strength (β) (Sec. 4.3). In the $++$ case, only one sign change was observed (Sec. 4.2). However, in the $+-$ case, multiple sign changes are observed at small speeds. This might be due to the pseudo-bound state formation during the collisions.

5.4 Electrical resistivity

The qualitative changes to the friction force arising from strong magnetization and particles with opposite charge translate to significant quantitative changes in the components of the electrical resistivity tensor. Here, we apply the results above to a first-order moment method that was used recently to explore the consequences of strong magnetization from a calculation of the friction force based on linear response theory [106]. Recall that linear response theory does not predict the Barkas effect [56].

This application of the GCO calculations are the first to explore the consequence of the Barkas effect on the electrical resistivity in a strongly magnetized plasma. Consider the form of Ohm's law obtained from the electron and ion force balance equation at steady state [106]

$$\mathbf{E}' = \eta_{\parallel}\mathbf{J}_{\parallel} + \eta_{\perp}\mathbf{J}_{\perp} + \eta_{\wedge}\mathbf{J}_{\wedge}, \tag{5.2}$$

where $\mathbf{E}' = \mathbf{E} + \mathbf{V} \times \mathbf{B}/c$ is the electric field in the rest frame of the fluid and $\mathbf{V}$ is the fluid center of mass velocity. Here, $\mathbf{J}_{\parallel}$, $\mathbf{J}_{\perp}$, $\mathbf{J}_{\wedge}$ are parallel, perpendicular and polar current density components with respect to the magnetic field. The parallel ($\eta_{\parallel}$), perpendicular ($\eta_{\perp}$) and Hall resistivity ($\eta_{\wedge}$) coefficients are related to the friction force density of ion-electron collisions via

$$\eta_{\parallel} J_{\parallel} = -\frac{2\mathbf{R}\cdot\hat{\mathbf{J}}_{\parallel}}{en}, \tag{5.3a}$$

$$\eta_{\perp} J_{\perp} = -\frac{2\mathbf{R}\cdot\hat{\mathbf{J}}_{\perp}}{en}, \tag{5.3b}$$

$$\eta_{\wedge} J_{\wedge} = \frac{BJ_{\wedge}}{en} - \frac{2\mathbf{R}\cdot\hat{\mathbf{J}}_{\wedge}}{en}. \tag{5.3c}$$

The friction force density for a Maxwellian distribution of ions with a small drift velocity can be related to the friction force on a single test charge via [106]

$$\mathbf{R} = \frac{2}{e\pi^{3/2}v_{T_1}^5}\int d^3v e^{-v^2/v_{T_1}^2}(\mathbf{J}\cdot\mathbf{v})\mathbf{F}. \tag{5.4}$$

The parallel, perpendicular and Hall conductivity coefficients can be obtained from the electrical resistivity coefficients using the following relations [106]

$$\sigma_{\parallel} = \frac{1}{\eta_{\parallel}} \tag{5.5a}$$

$$\sigma_{\perp} = \frac{\eta_{\perp}}{\eta_{\perp}^2 + \eta_{\wedge}^2} \tag{5.5b}$$

$$\sigma_{\wedge} = \frac{\eta_{\wedge}}{\eta_{\perp}^2 + \eta_{\wedge}^2}. \tag{5.5c}$$

Case	$\eta_\parallel/\eta_0$	$\eta_\perp/\eta_0$	$\eta_\wedge/\eta_0$	$\sigma_\parallel/\sigma_0$	$\sigma_\perp/\sigma_0$	$\sigma_\wedge/\sigma_0$
$\beta = 10, ++$	1.73	2.23	26.67	0.58	0.003	0.04
$\beta = 10, +-$	0.17	9.19	26.46	5.88	0.01	0.03
$\beta = 0, ++$	0.98	0.98	0.00	1.02	1.02	0.00
$\beta = 0, +-$	1.47	1.47	0.00	0.68	0.68	0.00

Table 5.1: Comparison of the parallel, perpendicular and Hall resistivity coefficients from oppositely charged and like-charged collisions. Here, the electron coupling strength is, $\Gamma = 1$.

Resistivity and conductivity coefficients are obtained by inserting the results from the previous section (corresponding to the polar plots shown in Figs. 5.2 and 5.3) into Eq. (5.4), computing the integral numerically and applying the results to Eqs. (5.3) and (5.5).

The results of the resistivity and conductivity calculations for $\Gamma = 1$ are shown in table 5.1. Here, $\eta_0 = m_2/(2n_2e^2\tau_2)$ and $\sigma_0 = 1/\eta_0$ are the reference resistivity and conductivity respectively. The Coulomb logarithm in electron collision time, $\tau_2 = 3\sqrt{m_2}(k_BT)^{(3/2)}/(8\sqrt{2\pi}n_2e^4\Xi)$ is replaced by the generalized Coulomb logarithm (Ξ) for an unmagnetized plasma [60] to account for strong coupling effects. The Barkas effect in unmagnetized plasma ($\beta = 0$) is found to increase the resistivity in both the perpendicular and parallel direction by almost 1.5 times. Strong magnetization in the case of like-charged collisions increases both the parallel and perpendicular resistivity. This is similar to what was observed in the linear response theory calculations [106]. However, the combination of the Barkas effect and strong magnetization is found to lead to a much more significant change, where the parallel resistivity is found to decrease by an order of magnitude and the perpendicular resistivity to also increase substantially. This is an expected consequence of the polar plots in Fig. 5.3 as the stopping power and transverse force components change in the Barkas case in such a way that the net force on the test charge in the perpendicular direction is increased and the parallel direction is decreased. Here, results from the $\Gamma = 0.1$ data are not shown because it was difficult to achieve the necessary accuracy of the numerical

evaluation of the GCO model at small speeds required to obtain convergent results in the resistivity calculations. However, the general the trend seen at $\Gamma = 1$ is expected at $\Gamma = 0.1$ too.

The linear response theory calculations predicted an increase in parallel resistivity with strong magnetization, [106] as does the GCO model for repulsive (++) interactions (i.e., the Barkas effect is not taken into account). A recent calculation using a Fokker-Plank collision operator predicted a decrease in the parallel resistivity due to strong magnetization [110]. Our GCO calculation agrees with this trend when the Barkas effect is accounted for. So, the disagreement between the Fokker-Plank calculation from Ref. [110] and the linear response calculation from Ref. [106] may be due to the lack of a Barkas effect in the linear response approach. The use of magnetized Fokker-Plank coefficients [44] assume attractive +− interactions, which may model the Barkas effect.

CHAPTER VI

Ion-Electron Temperature Relaxation Rate in Strongly Magnetized Plasmas

6.1 Introduction

Plasma generation typically results in a non-equilibrium state with electrons and ions at different temperatures, which subsequently equilibrate through energy exchange in Coulomb collisions. Understanding the rate of this relaxation is important to understanding plasma evolution. In this chapter, we calculate the ion-electron temperature relaxation rate in strongly magnetized plasmas.

In a weakly magnetized plasma, the ion temperature evolution owing to collisions with electrons can be obtained by taking the energy moment of the Boltzmann equation. For a spatially homogeneous plasma, this provides

$$\frac{dT_1}{dt} = -\nu\left(T_1 - T_2\right) \tag{6.1}$$

where T_1 is the ion temperature, T_2 is the electron temperature and ν is the temperature relaxation rate. For a weakly magnetized plasma where the gyromotion of the particles occurs at a larger length scale than scattering, the traditional Boltzmann

collision operator predicts the relaxation rate as [92]

$$\nu = \frac{32\sqrt{\pi}e^4 n_2 \ln\Lambda}{3m_1 m_2 (v_{T1}^2 + v_{T2}^2)^{3/2}}. \tag{6.2}$$

Here, n_2 is the density of the electrons, m_1 and m_2 are the masses of the ions and electrons, respectively, $v_{T1} = \sqrt{2T_1/m_1}$ and $v_{T2} = \sqrt{2T_2/m_2}$ are the thermal velocities, and $\ln\Lambda$ is the Coulomb logarithm.

The ion-electron temperature relaxation rate is calculated from the energy exchange density of a test ion interacting with background electrons. It is found that when the plasma is strongly magnetized, the parallel and perpendicular relaxation rates are no longer equal, causing a temperature anisotropy to form. Cases are considered for both attractive (electron-ion) and repulsive (positron-ion) interactions. The calculation predicts that the relaxation rates are qualitatively and quantitatively different in each case. The difference between the parallel and perpendicular relaxation rates for attractive collisions is much more significant than for repulsive collisions. For repulsive interactions, strong magnetization increases both the parallel and perpendicular relaxation rates and becomes constant at extreme values. In contrast, for attractive interactions, the parallel relaxation rate is inversely proportional to the magnetic field strength in the strongly magnetized regime.

Understanding the thermal relaxation of ions in strongly magnetized plasmas has many applications, including the antimatter experiments at Antihydrogen Laser Physics Apparatus (ALPHA), which synthesizes antihydrogen from antiprotons and positrons [28, 30]. In the experiment, the collisional temperature relaxation of antiprotons occurs in two stages. First, antiprotons are collisionally cooled with electrons, and second, the thermal equilibration of antiprotons with positrons during the recombination process [28, 30, 33]. For the typical experimental conditions, electrons and positrons are strongly magnetized and have magnetization strengths around few

hundred [28, 30]. Since both ion-electron and ion-positron interactions are important, the results for attractive (+−) and repulsive (++) potentials are both relevant to this experiment.

6.2 Theory

The temperature relaxation rate of a distribution of ions is closely related to the energy exchange density of a test ion slowing down on electrons [93, 111]. This is because the heavy mass of the ions makes their distributions very narrow compared to the electron velocity distribution. In this limit, the ion distribution can be modeled as a Dirac delta function, which is mathematically equivalent to a single particle. We first calculate the energy exchange density of a single test charge and later use it to calculate the temperature relaxation rate.

The energy exchange of a test charge that moves with a velocity, $\mathbf{v}_0$ in a sea of background electrons can be obtained by taking the energy moment of the collision operator ($\mathcal{Q}^{12} = \int d^3\mathbf{v}_1 m_1 (\mathbf{v}_1 - \mathbf{v}_0)^2 \mathcal{C}/2$). The velocity distribution of the test charges is a Maxwellian distribution with a flow ($\mathbf{v}_0$), but zero temperature. This limit is the Dirac delta function ($f_1 = n_1 \delta^3(\mathbf{v}_1 - \mathbf{v}_0)$). Thus for a single test charge, the energy exchange moment is $\mathcal{Q}^{12}/n_1$. Here, species 1 is ions and species 2 is the background electron or positron distribution. Using GCO, the energy exchange density is

$$\frac{\mathcal{Q}^{12}}{n_1} = \frac{n_2 m_1}{2\pi^{3/2} v_{T2}^3} \int d^3\mathbf{v}_2 ds |\mathbf{u} \cdot \hat{\mathbf{s}}| (\mathbf{v}_0' - \mathbf{v}_0)^2 e^{-v_2^2/v_{T2}^2}. \tag{6.3}$$

Here, the surface integral is on the surface of the collision volume, and the background plasma is assumed to be a Maxwellian distribution with thermal velocity $v_{T2} = \sqrt{2k_B T_2/m_2}$. The post collision velocity of the test charge ($\mathbf{v}_0'$) is the input to the collision operator and is obtained by solving equations of motion of the colliding particles inside the collision volume [Eqs. (3.1) and (3.2)].

The energy exchange density can be split into components parallel and perpendicular to the magnetic field ($\mathcal{Q}_{\parallel}^{12} = \int d^3\mathbf{v}_1 m_1(\mathbf{v}_{1\parallel} - \mathbf{v}_{0\parallel})^2\mathcal{C}/2$) and ($\mathcal{Q}_{\perp}^{12} = \int d^3\mathbf{v}_1 m_1(\mathbf{v}_{1\perp} - \mathbf{v}_{0\perp})^2\mathcal{C}/2$). The two components add up to give the total energy exchange density, i.e., $\mathcal{Q}^{12} = \mathcal{Q}_{\parallel}^{12} + \mathcal{Q}_{\perp}^{12}$. In a weakly magnetized plasma, $Q_{\parallel}^{12} = \frac{1}{2}Q_{\perp}^{12}$ in the limit of a low test charge speed. Separating the parallel and perpendicular components will enable an analysis of temperature anisotropy formation in strongly magnetized plasmas.

Similar to the case of the friction force calculation (Sec. 3.2), the energy moment integral is solved using the adaptive Monte Carlo integration code VEGAS [87, 88] and the equations of motion of the colliding particles were solved to obtain the post collision velocity.

6.3 Results

Figure 6.1 shows example profiles of the energy exchange density, in this case for a background coupling strength of $\Gamma_2 = 1$ and an angle of $\theta = 22.5^\circ$ between the test particle velocity and magnetic field. The energy exchange density in the parallel and perpendicular directions gives the thermalization rate of a cool beam of ions in those directions. Its value in the perpendicular direction is expected to be double that of the parallel direction because there are two degrees of freedom compared to one. When the parallel and perpendicular energy exchange densities do not satisfy this criterion, it leads to different relaxation rates in each direction, which can generate a temperature anisotropy.

For low speeds, the energy exchange densities are independent of the speed of the test charge (see Fig. 6.1). In the unmagnetized cases, the low-speed value of the perpendicular energy exchange density is double that of the parallel. This is the usual expectation of weakly magnetized plasma, where the electrons and ions relax isotropically in the limit there is no relative drift. However, in the case of strongly

magnetized plasma, the limiting values of the perpendicular energy exchange density are greater than double that of the parallel. Thus, strong magnetization is expected to lead to the development of temperature anisotropy during the relaxation. This difference in the perpendicular and parallel energy exchange densities is significantly enhanced for attractive collisions compared to repulsive. In fact, for $\beta_2 = 10$, $Q_\perp$ is more than an order of magnitude greater than $2Q_\parallel$, suggesting that electron-ion energy exchange is much faster in the perpendicular direction.

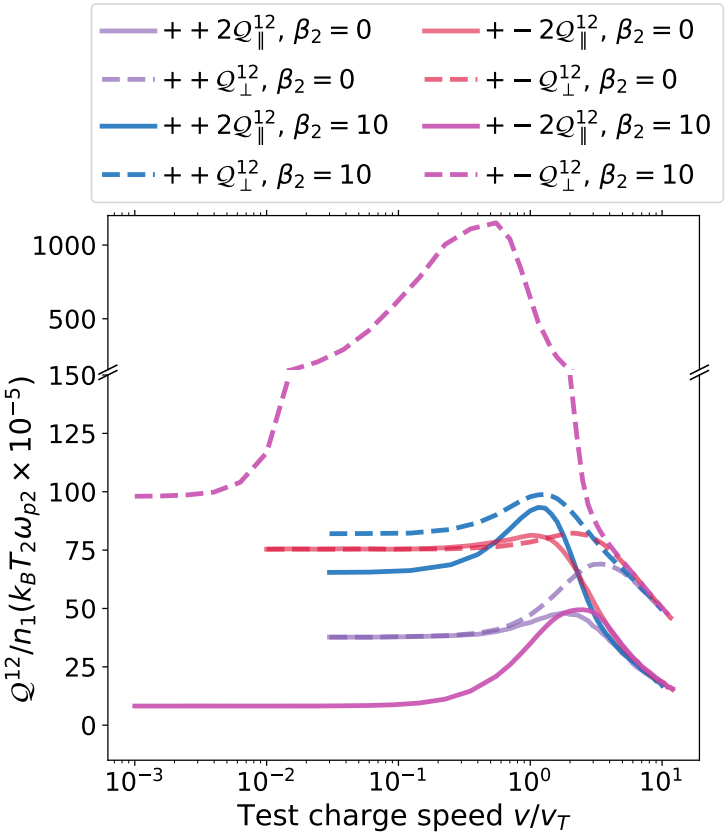

Figure 6.1: Energy exchange density components ($\mathcal{Q}_\perp^{12}$ and $\mathcal{Q}_\parallel^{12}$) of the like charged (++) and opposite charged (+−) cases for coupling strength, $\Gamma_2 = 1$ and orientation $\theta = 22.5°$. Note that the break in the vertical axis signifies a switch from linear to logarithmic scale.

The source of the difference in relaxation rate in the repulsive versus attractive cases (i.e., Barkas effect) is screening of the Coulomb potential (the effective potential part of this calculation). This difference is more significant in the case of small-speed

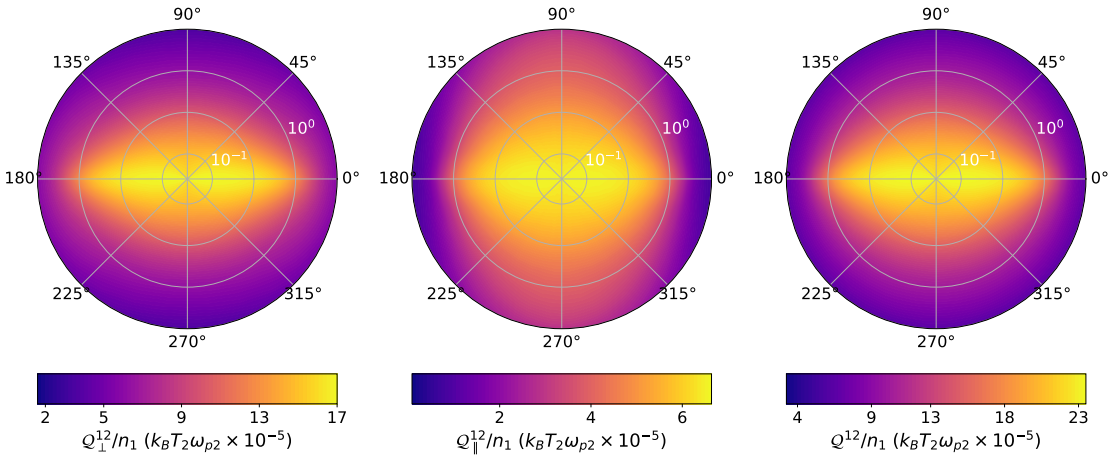

Figure 6.2: Polar plots of the energy exchange density components ($\mathcal{Q}_\perp^{12}$, $\mathcal{Q}_\parallel^{12}$ and $\mathcal{Q}^{12}$) of the like-charged (++) interaction at $\Gamma_2 = 0.1$ and $\beta_2 = 10$. The radial axis is the speed of the test charge (v_1/v_{T_2}) and the angle is the phase angle that the test charge velocity makes with the direction of the magnetic field (θ).

large-angle scattering than for high-speed small-angle scattering because the turning points in collisions are longer range where screening is significant. Thus, the energy exchange density enhancement due to the Barkas effect is absent at high speeds of the test charge and indicated by the merging of the like-charged and oppositely-charged curves; see Fig. 6.1. Similarly, the curves for the strongly magnetized conditions merge with those for unmagnetized conditions at high speeds. This is because the collisions of a high-speed test charge happen at a faster time scale than the gyromotion of the electrons, nullifying the strong magnetization effect.

Figures 6.2, 6.3 and 6.4 show results of computations of the energy exchange density components for different orientations of the test charge with respect to the direction of the magnetic field. Figures 6.2 and 6.3 show results for like-charged interactions at coupling strengths $\Gamma_2 = 0.1$ and $\Gamma_2 = 1$ and Fig. 6.4 for oppositely-charged interactions at coupling strength $\Gamma_2 = 1$. The energy exchange density not only depends on the speed and sign of the ion charge, but also on the orientation of the ion's velocity with respect to the direction of the magnetic field (θ). However, at very low speeds $Q_\parallel^{12}$ and $Q_\perp^{12}$ become independant of the orientation of test charge.

The comparison of Figs. 6.2 and 6.3 show that $Q_{\parallel}^{12}$ is largely independent of the angle (θ) at weak coupling ($\Gamma_2 = 0.1$), while $Q_{\perp}^{12}$ is peaked along the magnetic field. Here, both $Q_{\parallel}^{12}$ and $Q_{\perp}^{12}$ take maximal values in the low speed limit, having long flat plateaus at low speed. In contrast, at moderate coupling ($\Gamma_2 = 1$), the dependence of both $Q_{\parallel}^{12}$ and $Q_{\perp}^{12}$ on the angle becomes more pronounced and the peak value of each is along the magnetic field at a speed of a few thermal speeds.

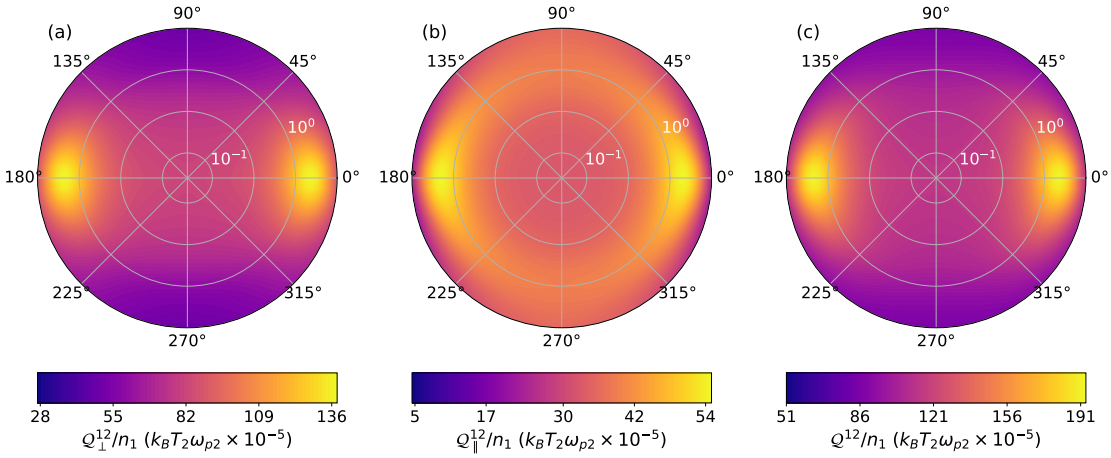

Figure 6.3: Polar plots of the energy exchange density components ($\mathcal{Q}_{\perp}^{12}$, $\mathcal{Q}_{\parallel}^{12}$ and $\mathcal{Q}^{12}$) of the like-charged (++) interaction at $\Gamma_2 = 1$ and $\beta_2 = 10$. The radial axis is the speed of the test charge (v_1/v_{T_2}) and the angle is the phase angle that the test charge velocity makes with the direction of the magnetic field (θ).

The comparison of Figs. 6.3 and 6.4 show that for attractive interactions (+−), the peak value of $Q_{\perp}^{12}$ is significantly larger than all other cases and occurs at a speed slightly less than the thermal speed. This suggests that the energy exchange in the perpendicular direction is very rapid for an oppositely charged beam especially when moving slightly slower than the thermal speed of the electrons. In this case, the peak value of all energy exchange density components is when the test charge moves perpendicular to the magnetic field. This contrasts with the repulsive (++) case, where the peak values occur when the test charge moves along the magnetic field. This observation is similar to the friction force, where the oppositely charged test charge (+−) experiences maximum friction when moving perpendicular to the

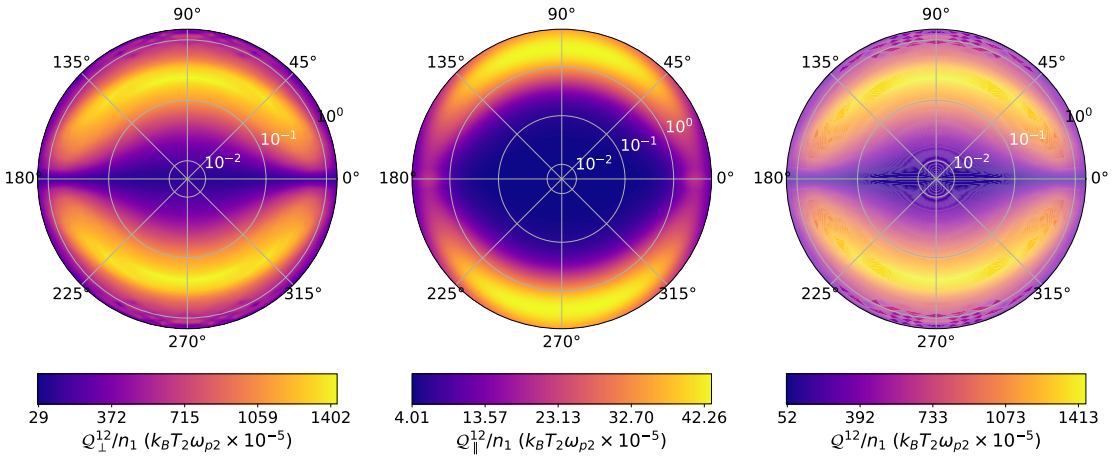

Figure 6.4: Polar plots of the energy exchange density components ($\mathcal{Q}_{\perp}^{12}$, $\mathcal{Q}_{\parallel}^{12}$ and $\mathcal{Q}^{12}$) of the opposite-charged ($+-$) interaction at $\Gamma_2 = 1$ and $\beta_2 = 10$. The radial axis is the speed of the test charge (v_1/v_{T_2}) and the angle is the phase angle that the test charge velocity makes with the direction of the magnetic field (θ).

magnetic field, while the like-charged case is peaked when moving parallel to the magnetic field (Subsec. 5.3.2). The increase of the peak value from the plateau value in the low speed limit is also significant in the $+-$ case.

6.4 Temperature relaxation

The energy exchange density for a test charge was discussed in the previous section. Here, we extend the calculation to a distribution of ions with a finite temperature and apply the result to model the evolution of the ion distribution as it relaxes with a strongly magnetized electron distribution held at a fixed temperature (i.e., a heat bath). Since strong magnetization causes an anisotropy in the energy exchange density, we consider an anisotropic Maxwellian distribution for ions

$$f_1 = \frac{n_1}{\pi^{3/2} v_{T_{1\perp}}^2 v_{T_{1\parallel}}} e^{-v_{1\parallel}^2/v_{T_{1\parallel}}^2} e^{-v_{1\perp}^2/v_{T_{1\perp}}^2}. \tag{6.4}$$

Here, $v_{T_{1\parallel}} = \sqrt{2k_B T_{1\parallel}/m_1}$ and $v_{T_{1\perp}} = \sqrt{2k_B T_{1\perp}/m_1}$ are parallel and perpendicular ion thermal speeds. For parallel energy exchange density, we get,

$$\mathcal{Q}_\parallel = \frac{1}{2} m_1 \int d^3\mathbf{v}_1 d^3\mathbf{v}_2 ds |\mathbf{u}\cdot\hat{\mathbf{s}}| (v_{1\parallel}'^2 - v_{1\parallel}^2) f_1 f_2 \tag{6.5}$$

Using, $v_{1\parallel}'^2 - v_{1\parallel}^2 = (v_{1\parallel}' - v_{1\parallel})^2 + 2v_{1\parallel}(v_{1\parallel}' - v_{1\parallel})$, this can equivalently be expressed as

$$\mathcal{Q}_\parallel = \frac{1}{2} m_1 \int d^3\mathbf{v}_1 d^3\mathbf{v}_2 ds |\mathbf{u}\cdot\hat{\mathbf{s}}| \Big[(v_{1\parallel}' - v_{1\parallel})^2 + 2v_{1\parallel}(v_{1\parallel}' - v_{1\parallel}) \Big] f_1 f_2. \tag{6.6}$$

On rewriting $f_1(\mathbf{v}_1) = \int \delta^3(\mathbf{v}_1 - \mathbf{v}_0) f_1(\mathbf{v}_0) d^3\mathbf{v}_0$, and evaluating the $d^3\mathbf{v}_1$ integral

$$\begin{aligned} \mathcal{Q}_\parallel = & \int d^3\mathbf{v}_0 f_1(\mathbf{v}_0) \int d^3\mathbf{v}_2 ds |\mathbf{u}\cdot\hat{\mathbf{s}}| \frac{1}{2} m_1 (v_{0\parallel}' - v_{0\parallel})^2 f_2 \\ & + \int d^3\mathbf{v}_0 f_1(\mathbf{v}_0) \int d^3\mathbf{v}_2 ds |\mathbf{u}\cdot\hat{\mathbf{s}}| m_1 v_{0\parallel} (v_{0\parallel}' - v_{0\parallel}) f_2. \end{aligned} \tag{6.7}$$

Assuming an isotropic Maxwellian distribution of electrons,
$f_2 = n_2/(\pi^{3/2} v_{T_2}^3) \exp(-v_2^2/v_{T_2}^2)$ and using the definitions of energy exchange density, Eq. (6.3), and friction force of the test charge charge (Sec. 3.1)

$$\mathbf{F} = \frac{n_2 m_1}{\pi^{3/2} v_T^3} \int d^3\mathbf{v}_2 \int\limits_{S_-} ds\, |\mathbf{u}\cdot\hat{\mathbf{s}}| (\mathbf{v}_0' - \mathbf{v}_0) e^{-v_2^2/v_T^2}, \tag{6.8}$$

this can be further simplified to

$$\mathcal{Q}_\parallel = \int d^3\mathbf{v}_0 f_1(\mathbf{v}_0) \mathcal{Q}_\parallel^{12}/n_1 + \int d^3\mathbf{v}_0 f_1(\mathbf{v}_0) F_\parallel v_{0\parallel}. \tag{6.9}$$

Similarly, the perpendicular energy exchange density is

$$\mathcal{Q}_\perp = \int d^3\mathbf{v}_0 f_1(\mathbf{v}_0) \mathcal{Q}_\perp^{12}/n_1 + \int d^3\mathbf{v}_0 f_1(\mathbf{v}_0) \mathbf{F}_\perp \cdot \mathbf{v}_{0\perp}. \tag{6.10}$$

Finally, the parallel and perpendicular energy moments of the Boltzmann equation connect the energy exchange densities to the rate of change of the respective temperatures

$$n_1 k_B \frac{dT_{1\perp}}{dt} = \mathcal{Q}_\perp, \tag{6.11}$$

$$\frac{1}{2} n_1 k_B \frac{dT_{1\parallel}}{dt} = \mathcal{Q}_\parallel. \tag{6.12}$$

Considering the common situation that the electron and ion temperatures are not dramatically different (i.e., $T_1/T_2 \sim 1$), an analytic approximation of the temperature evolution can be obtained by assuming a linear dependence of the form: $\mathcal{Q}_\parallel \propto (1 - T_{1\parallel}/T_2)$ and $\mathcal{Q}_\perp \propto (1 - T_{1\perp}/T_2)$. In the limit that the parallel or perpendicular temperature is zero, the energy exchange density should asymptote to the value for that of a test charge in the limit of zero speed, i.e., $\mathcal{Q}_\perp(T_{1\perp} \to 0) = \mathcal{Q}_\perp^{12}(v_1 \to 0)$ and $\mathcal{Q}_\parallel(T_{1\parallel} \to 0) = \mathcal{Q}_\parallel^{12}(v_1 \to 0)$. In the limit that the ion parallel or perpendicular temperature is equal to that of the electron temperature, the energy exchange in the respective directions goes to zero, i.e., $\mathcal{Q}_\perp(T_{1\perp} \to T_2) = 0$ and $\mathcal{Q}_\parallel(T_{1\parallel} \to T_2) = 0$. With these two limiting cases and the assumption of a linear dependence on the temperature ratio, the parallel and perpendicular energy exchange densities for a distribution of ions can be related to the test particle values in the low speed limit

$$\mathcal{Q}_\parallel = \lim_{v_1 \to 0} \mathcal{Q}_\parallel^{12}(v_1) \left(1 - \frac{T_{1\parallel}}{T_2}\right) \tag{6.13}$$

$$\mathcal{Q}_\perp = \lim_{v_1 \to 0} \mathcal{Q}_\perp^{12}(v_1) \left(1 - \frac{T_{1\perp}}{T_2}\right) \tag{6.14}$$

where $\mathcal{Q}_\parallel^{12}(v_1)$ and $\mathcal{Q}_\perp^{12}(v_1)$ are the components of the test particle energy exchange density.

This linear model is overall in good agreement with direct numerical integration of Eqs. (6.9) and (6.10) for ion-electron temperature ratios near 1; as shown in Fig. 6.5.

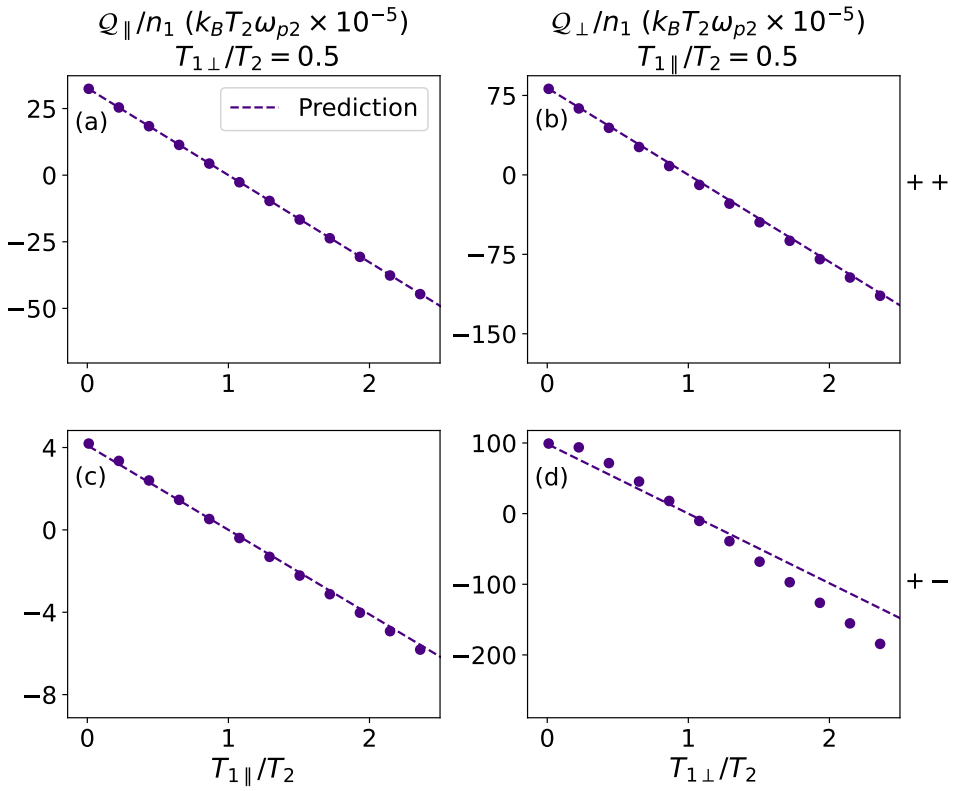

Figure 6.5: Energy exchange density of an ion distribution as a function of its parallel [(a) and (c) for fixed $T_\perp/T_2 = 0.5$] and perpendicular [(b) and (d) for fixed $T_\parallel/T_2 = 0.5$] temperatures. Circles denote solutions of Eqs. (6.9) and (6.10). The dashed line shows the linear prediction from Eqs. (6.13) and (6.14). The top row is for the case of like-charged collisions and bottom row is for the case of opposite-charged collisions. Here, the coupling strength is $\Gamma_2 = 1$ and magnetization is $\beta_2 = 10$.

The small deviation of $\mathcal{Q}_\perp$ from the linear prediction in the attractive interaction case $(+-)$ might be because the $\mathcal{Q}_\perp^{12}$ curve does not plateau to a constant value until very small speeds are reached ($v/v_T \lesssim 10^{-2}$); see Fig. 6.1. The energy exchange density of the ions having a linear dependence on the ion temperature is equivalent to saying that the temperature relaxation rate is independent of the ion temperature. From Eqs. (6.11)–(6.14), we get

$$\frac{dT_{1\perp}}{dt} = -\nu_\perp \left(T_{1\perp} - T_2\right) \tag{6.15}$$

$$\frac{dT_{1\parallel}}{dt} = -\nu_\parallel \left(T_{1\parallel} - T_2\right) \tag{6.16}$$

where,

$$\nu_\perp = \lim_{v_1 \to 0} \frac{\mathcal{Q}_\perp^{12}(v_1)}{n_1 k_B T_2}, \tag{6.17}$$

$$\nu_\parallel = 2 \lim_{v_1 \to 0} \frac{\mathcal{Q}_\parallel^{12}(v_1)}{n_1 k_B T_2}. \tag{6.18}$$

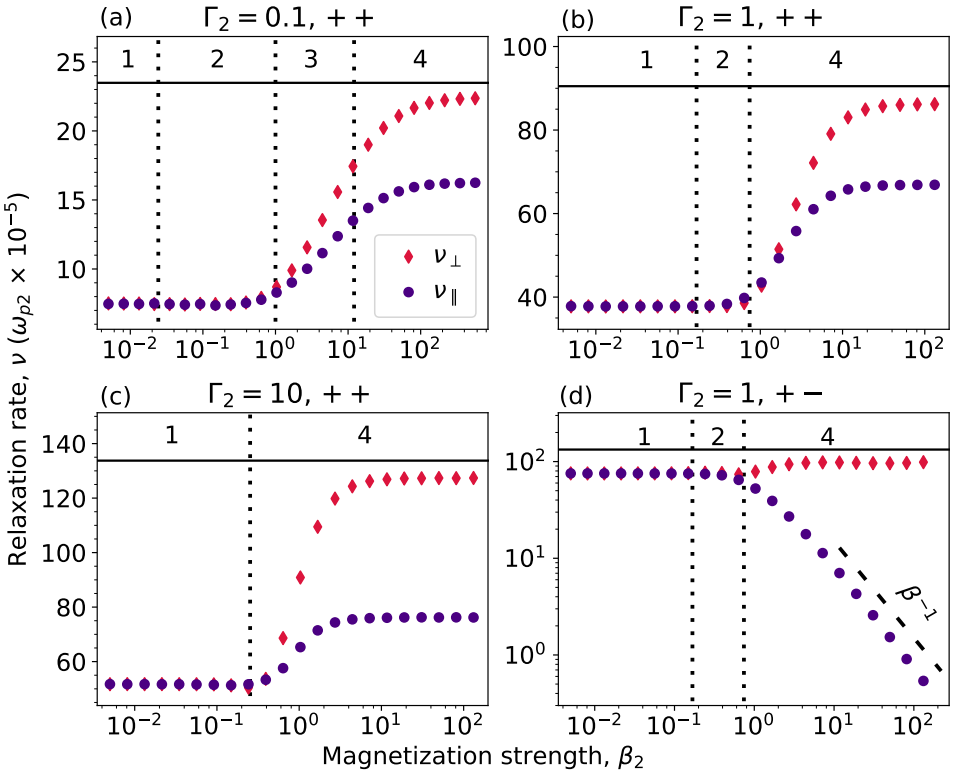

Figure 6.6: The ion-electron temperature relaxation rates for like-charged collisions [(a) $\Gamma_2 = 0.1$, (b) $\Gamma_2 = 1$ and (c) $\Gamma_2 = 10$] and opposite charged collisions [(d) $\Gamma_2 = 1$]. The red circles are the perpendicular relaxation rates and the blue circles are the parallel relaxation rates. Vertical dotted lines delineate transitions between the four transport regimes.

The temperature relaxation rates ν (linear order) depend only on the low speed value of $\mathcal{Q}^{12}$. Since the low speed value of $\mathcal{Q}^{12}$ does not depend on the orientation of the test charge with respect to the magnetic field, the calculation of the temperature relaxation can be extended to higher β values very efficiently. Instead of creating the whole polar plot and integrating, $\mathcal{Q}^{12}$ was calculated for a fixed orientation $\theta = 22.5°$,

at very low speed ($\approx 10^{-2} v_{T2}$) for different magnetization strengths. The results of this calculation for different coupling strengths are shown in Fig. 6.6. This figure also indicates the four transport regimes discussed in Sec. 1.1

As expected, the parallel and perpendicular temperature relaxation rates are independent of the magnetic field strength and have the same value through the unmagnetized and weakly magnetized regimes (1 and 2). The independence of the relaxation rates on the magnetic field is expected because the generalized collision operator in these regimes is equivalent to the traditional Boltzmann collision operator, which does not depend on the magnetic field strength (Sec. 2.2). In contrast, the parallel and perpendicular relaxation rates depend on the magnetic field strength and take different values from one another in the strongly and extremely magnetized regimes. The difference in the relaxation rates can cause anisotropy to form in the ion temperature during the collisional relaxation to thermal equilibrium. For like-charged interactions, strong magnetization increases both the parallel and perpendicular temperature relaxation rates (though by differing amounts), reaching constant values in the large β limit. A strikingly different behaviour is observed in the case of oppositely charged interactions, where although the perpendicular relaxation rate increases, the parallel relaxation rate decreases at a rate inversely proportional to β: $\nu_{\parallel} \propto \beta^{-1}$. This leads to a dramatic suppression of energy exchange along the magnetic field at high values of the magnetization strength.

6.5 Discussion

This section discusses the temperature evolution of warm ions cooling down on a cool bath of electrons. The density of the background electrons (lighter species) is taken as much larger than the ion density so it can be considered a heat bath (i.e., constant temperature). This case is representative of anti-matter traps where antiprotons are mixed with electrons at the cooling stage (repulsive case) and with

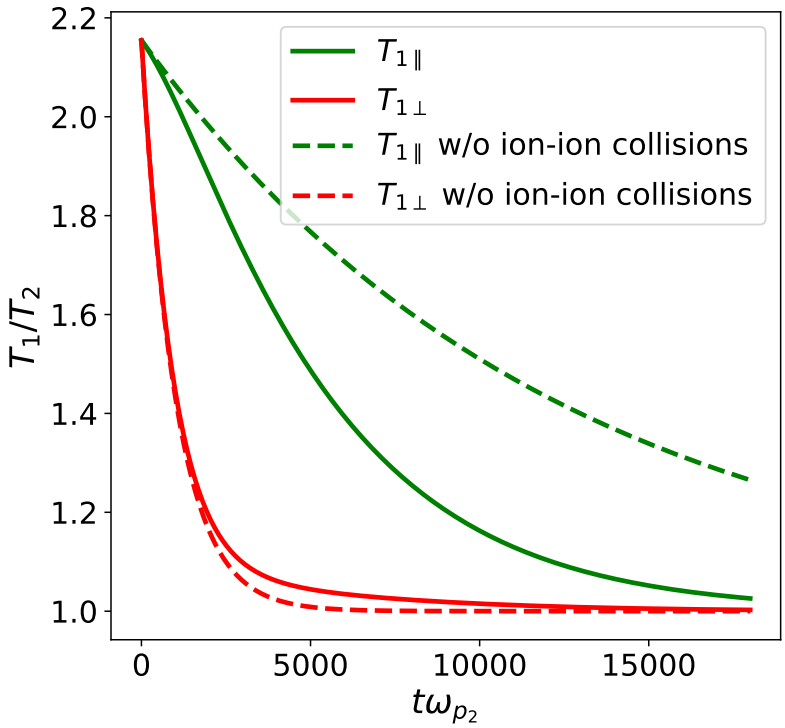

Figure 6.7: The parallel and perpendicular ion temperature evolution when warm ions collisionally relax with a heat bath of electrons. Here, the electron coupling strength is $\Gamma_2 = 1$ and magnetization strength is $\beta_2 = 10$. Solid lines are for the case were both the ion-electron and ion-ion collisions are present and dashed lines are for the case where ion-ion collisions are turned off.

positrons during antihydrogen formation (attractive case) [28, 30, 33].

When there is an anisotropy in the ion temperature, ion-ion collisions reduce the anisotropy. Thus, when considering the ion temperature evolution, in addition to the ion-electron collisions, contributions from ion-ion collisions are included as a collision term in the Boltzmann equation. The temperature evolution equation of the ions then takes the following form,

$$\frac{dT_{1\perp}}{dt} = -\nu_\perp \left(T_{1\perp} - T_2\right) - \nu_A (T_{1\perp} - T_{1\|}) \tag{6.19}$$

$$\frac{dT_{1\|}}{dt} = -\nu_\| \left(T_{1\|} - T_2\right) + 2\nu_A (T_{1\perp} - T_{1\|}) \tag{6.20}$$

where ν_A is the anisotropy relaxation rate due to ion-ion interactions. Since ions are weakly magnetized, we use the relaxation rates from Ref. [112], obtained using the traditional Boltzmann collision operator to model this term,

$$\frac{\nu_A}{\bar{\nu}} = \frac{3\sqrt{\pi}}{16}\frac{(1+\frac{2}{3}A)^{3/2}}{\sqrt{\alpha}A^{5/2}}\int_0^\infty d\xi\xi^2 e^{-\alpha\xi^2}\frac{\sigma^{(2)}}{\sigma_0} \times\left[\frac{2}{3}\xi^2\alpha A\mathrm{erf}(\xi\sqrt{\alpha A})-\psi(\xi^2\alpha A)\right]. \tag{6.21}$$

Here, $\sigma_0 \equiv \pi e^4/(2k_BT)^2$, $\xi^2 \equiv u^2/(2v_{T1}^2)$, $A \equiv T_{1\perp}/T_{1\parallel}-1$, $\alpha \equiv \frac{1}{3}(3+2A)/(1+A)$, $\bar{\nu} = 2\sqrt{\pi/m_1}n_1e^4/(k_BT_1)^{3/2}$ is the reference collision frequency, $\sigma^{(2)}$ is the 2$^{\mathrm{nd}}$ momentum scattering cross section obtained using the potential of mean force computed from the HNC approximation for the one component plasma [Eq. (27) in Ref. [112]] and

$$\psi(x) = \mathrm{erf}(\sqrt{x}) - \frac{2}{\sqrt{\pi}}\sqrt{x}e^{-x} \tag{6.22}$$

is the Maxwell integral.

The temperature evolution obtained by integrating Eqs. (6.19) and (6.20)] is shown in Fig. 6.7. The plots are for the attractive $(+-)$ interaction. As the previous section shows, electron-ion collisions lead to different temperature relaxation rates in the perpendicular and parallel directions. Thus, as a warm ion distribution collisionally relaxes with electrons toward the equilibrium temperature, a temperature anisotropy develops. The dashed lines are the results of solving the equations without the ion-ion collisions, and solid lines account for both the ion-electron and ion-ion collisions. Here, the initial ion distribution is an isotropic Maxwellian distribution with a temperature, $T_1/T_2 = 2.1$, and the electrons are assumed to have a coupling strength, $\Gamma_2 = 1$, and magnetization strength, $\beta_2 = 10$. The density ratio of ions to electrons is $n_1/n_2 = 10^{-2}$. Even though the initial distribution is isotropic, the ion-electron collisional relaxation rate differs in the perpendicular and parallel directions, induc-

ing temperature anisotropy during the relaxation process. Since the perpendicular energy equilibration rate is much larger than the parallel, the anisotropy is such that the parallel temperature is larger through the evolution. This anisotropy is slightly relaxed by ion-ion collisions. For a positron density of 6.5×10^7 cm^{-3}, the perpendicular temperature of antiprotons reach the equilibrium value by 3×10^{-5} s and parallel by 4.5×10^{-5} s.

CHAPTER VII

Conclusion

The work presented in this dissertation has developed a generalized Boltzmann kinetic theory that is applicable across coupling magnetization phase space. The theory was used to compute two transport properties - friction and temperature relaxation.

The generalized collision operator is a 5-D integral: 3-D velocity space and 2-D physical space on the surface of a collision volume, inside of which the particles interact via the potential of mean force. The size of the collision volume is determined by the range of the potential of mean force. The theory incorporates the magnetic field into the collisions by including the Lorentz force acting on the colliding particles in the equations of motion describing binary collision. The equations of motion do not have an analytic closed-form solution. Therefore, they are solved numerically to obtain input for the collision operator; in contrast to the pre-calculated cross section of the traditional Boltzmann collision operator. The traditional Boltzmann collision operator for unmagnetized and weakly magnetized plasma and O'Neil's Boltzmann-like collision operator for the extremely magnetized plasma were obtained from the generalized collision operator by simplifying the collision geometry and equations of motion for the interacting particles in the limits of no magnetic field and high magnetic field, respectively.

In chapter III, the generalized collision operator was applied to compute the friction force acting on a massive test charge moving through a weakly coupled magnetized one-component plasma. First, the numerical implementation of the generalized collision operator was verified by comparing results from the unmagnetized and weakly magnetized plasma cases with the accepted results of the traditional Boltzmann kinetic theory. Then the friction force calculation was extended to strongly magnetized plasmas, where it was found that the strong magnetization gave rise to the transverse force component in addition to the stopping power component. These results were in good agreement with previous linear response theory results. The work also extended the computation of the friction force to the extremely magnetized transport regime, which was not attainable using the linear response theory. The transverse force mixes the parallel and perpendicular velocity components of the projectile. Its sign changes if the test charge speed is either faster or slower than approximately the thermal speed of the plasma species with which it predominately interacts. The transverse force acts to increase the gyroradius of fast particles and to decrease the gyroradius of slow particles.

Chapter IV described the extension of generalized Boltzmann kinetic theory to the strongly coupled regime. The utility of the collision operator was shown by calculating the friction force on a test charge moving through a background plasma at conditions that range from weakly to strongly coupled and weakly to strongly magnetized. Good agreement was found between the results from the GCO calculation and previous MD simulations. The combination of strong coupling and strong magnetization introduced a third "gyrofriction" component in the direction of the Lorentz force. Similar to the transverse force, the magnitude and sign of the gyrofriction depend on the speed and orientation of the projectile's velocity with the direction of the magnetic field. It was found to be zero when the projectile moves parallel or antiparallel to the magnetic field and has a maximum magnitude when the test charge's velocity is perpendicular

to the magnetic field. The average trajectory of a projectile slowing down in a strongly magnetized plasma was computed using the friction force data. It showed that the transverse force and the gyrofriction influence the overall evolution of the projectile. The transverse force changes the gyroradius and alters the stopping distance, and the gyrofriction slightly modifies the gyrofrequncy resulting in a phase shift. The effect of the gyrofriction on the trajectory of the projectile was found to be small due to the large Lorentz force term.

In chapter V, the GCO was used to calculate the friction force on an oppositely charged test charge moving through a strongly magnetized plasma. It was found that the friction force strongly depends on the sign of the test charge, breaking the fundamental symmetry of independence of transport properties on the sign of charge that is present in weakly coupled weakly magnetized plasmas. This effect is analogous to the Barkas effect observed in strongly coupled plasmas and charged particle stopping in emulsion experiments. The Barkas effect in strongly magnetized plasmas decreased the magnitude of the Bragg peak of the stopping power component of the friction force and increased the transverse and gyrofriction components compared to the like-charged case. Moreover, the magnitude of the gyrofriction becomes as large as the transverse force in the oppositely-charged case. The stopping power of an oppositely charged test charge is found to be maximum when moving perpendicular to the magnetic field and minimum when moving parallel to the magnetic field. This is opposite to the like-charged case, where the stopping power was maximum when moving parallel to the magnetic field and minimum when moving perpendicular to the magnetic field. The generalized Ohm's law for the strongly magnetized plasmas from the first order moment method showed that the Barkas effect increases the perpendicular resistivity and decreases the parallel resistivity by almost an order of magnitude (at the example $\Gamma = 1$, $\beta = 10$ conditions).

In chapter VI, GCO was used to calculate the ion-electron temperature relaxation

rate. The temperature relaxation rate was obtained from the energy exchange density of a test charge slowing down in a strongly magnetized plasma. It was found that when the plasma is strongly magnetized, the relaxation rates change and also cause the rates in the parallel and perpendicular directions to no longer be equal. Different parallel and perpendicular temperature relaxation rates cause temperature anisotropy to develop when the ions and electrons equilibrate to a common temperature. The relaxation rates were also found to depend on the sign of the charge of the interacting particles, known as the Barkas effect. The Barkas effect increases the difference between the parallel and perpendicular relaxation rates. The parallel relaxation rate in the case of oppositely charged interaction was found to be inversely proportional to the magnetic field strength in the strongly magnetized regime.

By extending the kinetic theory to the transport regimes with the gyroradius smaller than the characteristic scattering length, we now have a theory to understand the fundamental properties of strongly magnetized plasmas. This dissertation has demonstrated that strong magnetization fundamentally alters how momentum and energy are transported, resulting in several non-intuitive physical results. These new results may be observed in many magnetized plasma experiments, including ultra-cold neutral plasmas [8, 24, 26] and antimatter traps [3]. Modeling these experiments requires the computation of macroscopic transport coefficients like diffusion [13, 49, 54, 113], conductivity [114], shear viscosity [115], and other characteristics like the dynamic structure factor [116].

Future works plan to develop the theory further to compute the macroscopic transport properties measured in magnetized ultra-cold neutral plasma experiments. This can be done by developing a magnetohydrodynamic (MHD) theory by solving the generalized kinetic theory using the Chapman-Enskog method. Since the generalized collision operator is quadratically dependent on the distribution function like the traditional Boltzmann collision operator, most of the mathematical structure of the

traditional Chapman-Enskog derivation of the weakly magnetized plasmas will carry over. The main change will be the evaluation of the "bracket integrals" that are solved for the transport coefficients. These are moments (velocity-space integrals) of the collision operator with polynomial coefficients. In a weakly magnetized plasma, these integrals can be done analytically due to the closed-form solution of the cross section. However, for the generalized collision operator, these integrals need to be evaluated numerically by solving particle trajectories. These transport coefficients can be used to model the plasma expansion, and results can be compared directly with the experiments [26].

Future works are also planned to explore the novel plasma physics of antihydrogen synthesis at ALPHA. These works focus on understanding how the strong magnetization and strong coupling modify the temperature anisotropy relaxation rate and the rate at which electrons sympathetically cool antiprotons. The temperature evolution of the antiprotons and electrons (or positrons) can be obtained from a two-fluid description of the plasma. This can be achieved by taking the energy moment of the generalized Boltzmann equation for both the species and modeling the cyclotron cooling of the electrons by including an energy loss term based on the classical cyclotron emission formula. Strong magnetization is also expected to modify the rate at which antihydrogen is produced. The dominant pathway in which antihydrogen is produced in ALPHA is through the three-body recombination process involving two positrons and one antiproton. Future works plan to calculate the recombination rate by studying the three particle collisions in strongly magnetized plasmas.

APPENDIX

APPENDIX A

Numerical Evaluation of the Friction Force Integral

Three components of the friction force are obtained from the friction force density using the following definitions

$$F_v = \frac{\mathbf{R}^{12} \cdot \hat{\mathbf{v}}_0}{n_1}, \tag{A.1a}$$

$$F_\times = \frac{\mathbf{R}^{12} \cdot (\hat{\mathbf{v}}_0 \times \hat{\mathbf{n}})}{n_1}, \tag{A.1b}$$

$$F_n = \frac{\mathbf{R}^{12} \cdot \hat{\mathbf{n}}}{n_1}, \tag{A.1c}$$

where the friction force density is (Eq. 3.5)

$$\mathbf{R}^{12} = \frac{n_1 n_2 m_1}{\pi^{3/2} v_T^3} \int d^3\mathbf{v}_2 \int_{S_-} ds\, |\mathbf{u} \cdot \hat{\mathbf{s}}| (\mathbf{v}_1' - \mathbf{v}_0) \exp\left(\frac{-v_2^2}{v_T^2}\right). \tag{A.2}$$

The unknown quantity here is the postcollision velocity and it is obtained by solving

the equations of motion (Eqs. (3.1) and (3.2)).

$$(m_1+m_2)\frac{d\mathbf{V}}{dt} = e\Big(\frac{\mathbf{V}}{c}\times\mathbf{B}\Big) - \frac{e\,m_{12}}{m_2}\Big(\frac{\mathbf{u}}{c}\times\mathbf{B}\Big) \tag{A.3}$$

$$m_{12}\frac{d\mathbf{u}}{dt} = -\nabla\phi(r) + \frac{e\,m_{12}^2}{m_2^2}\Big(\frac{\mathbf{u}}{c}\times\mathbf{B}\Big) - \frac{e\,m_{12}}{m_2}\Big(\frac{\mathbf{V}}{c}\times\mathbf{B}\Big). \tag{A.4}$$

Since there is no closed-form solution of the equations of motion of the particles, analytic solution of these integrals are not possible. Thus the friction force density integral (Eq. A.2) is solved numerically. For this, the equations are first made dimensionless by normalizing the time with the plasma frequency, distance with the Debye length and velocity with the Debye length times the plasma frequency. Using the scaled variables we get,

$$\mathbf{R}^{12} = \frac{m_r k_B T n_1}{8\sqrt{6}\pi^{5/2}\Gamma^{3/2}\lambda_D}\int \tilde{v}_2^2\sin\theta_{v_2}d\theta_{v_2}d\phi_{v_2}d\tilde{v}_2$$
$$\times\int_{\tilde{S}_-}\tilde{R}_s^2\sin\theta_{R_s}d\theta_{R_s}d\phi_{R_s}|\tilde{\mathbf{u}}\cdot\hat{\mathbf{s}}|(\tilde{\mathbf{v}}_1'-\tilde{\mathbf{v}}_0)\exp\left(\frac{-\tilde{v}_2^2}{2}\right), \tag{A.5}$$

and

$$\frac{d\tilde{\mathbf{V}}}{d\tilde{t}} = \frac{\beta}{m_r+1}(\tilde{\mathbf{V}}\times\hat{\mathbf{z}}) - \frac{\beta m_r}{(m_r+1)^2}(\tilde{\mathbf{u}}\times\hat{\mathbf{z}}), \tag{A.6}$$

$$\frac{d\tilde{\mathbf{u}}}{d\tilde{t}} = \frac{\beta m_r}{m_r+1}(\tilde{\mathbf{u}}\times\hat{\mathbf{z}}) - \beta(\tilde{\mathbf{V}}\times\hat{\mathbf{z}}) + \frac{(m_r+1)\sqrt{3}\Gamma^{3/2}}{m_r}\frac{e^{-\tilde{r}}}{\tilde{r}^3}\Big(1+\tilde{r}\Big)\tilde{\mathbf{r}}. \tag{A.7}$$

Here, the collision volume is taken as a sphere of radius $3.5\lambda_D$ and the friction force density integral is written in spherical polar coordinates for both velocity and space. The variables with tilde ($\tilde{}$) on top represent scaled variables.

The equations of motion (Eq. (A.6) and Eq. (A.7)) are an initial value problem. The initial velocity of the background particle and initial position in the relative

coordinates given by each point in the 5-D integral

$$\tilde{\mathbf{r}}_i = \begin{bmatrix} \tilde{R}_s \sin\theta_{R_s} \cos\phi_{R_s} \\ \tilde{R}_s \sin\theta_{R_s} \sin\phi_{R_s} \\ \tilde{R}_s \cos\theta_{R_s} \end{bmatrix} \tag{A.8}$$

$$\tilde{\mathbf{v}}_{2i} = \begin{bmatrix} \tilde{v}_2 \sin\theta_{v_2} \cos\phi_{v_2} \\ \tilde{v}_2 \sin\theta_{v_2} \sin\phi_{v_2} \\ \tilde{v}_2 \cos\theta_{v_2} \end{bmatrix} \tag{A.9}$$

and the initial velocity of the projectile $\tilde{\mathbf{v}}_{1i}$ is $\tilde{\mathbf{v}}_0$. The unit normal vector is $\hat{\mathbf{s}} = \tilde{\mathbf{r}}_i/\tilde{R}_s$. Using Eq. (2.10), $\tilde{\mathbf{v}}_0$ and $\tilde{\mathbf{v}}_{2i}$ were transformed to the relative and the center of mass coordinates. For initial states that satisfy $\tilde{\mathbf{u}} \cdot \hat{\mathbf{s}} < 0$, the particle trajectories were obtained by solving the equations of motion using the "DOP 853" method. This is an adaptive Runge-Kutta method of order 8 based on method of Dormand & Prince [89] with local error estimation and step size control based on embedded formulas of orders 5 and 3.

The adaptive time stepping method considerably speeds up the trajectory calculations compared to fixed time methods. When the particles are far away, their interactions are weak, and large time steps can easily resolve the trajectories. However, small steps are needed to resolve the interaction when particles are very close. The adaptive time-stepping method would speed through the trajectory calculations with large strides when the particles are far away and tiptoe through with small steps when the particles are very close. In contrast, a fixed time step method is limited to the smallest time step required to resolve collisions when particles are close for the entirety of the trajectory calculation.

The trajectory calculations were stopped when the particle crossed the collision volume, i.e., $|\tilde{\mathbf{r}}| > \tilde{R}_s$. In order to calculate the change of projectile velocity $(\tilde{\mathbf{v}}_1' - \tilde{\mathbf{v}}_0)$ at

the surface of the collision volume, a dense output [89] of order 7 is obtained between the time steps just before crossing the collision volume ($|\tilde{\mathbf{r}}| < \tilde{R}_s$) and just after crossing the collision volume ($|\tilde{\mathbf{r}}| > \tilde{R}_s$) and solved for ($|\tilde{\mathbf{r}}| = \tilde{R}_s$) using Wijngaarden-Dekker-Brent method [85].

The integrals for computing different components of the friction force are five-dimensional: three in the velocity space and two in the coordinate space. Extending the standard one-dimensional integration techniques to evaluate the five-dimensional integral becomes very expensive. To efficiently evaluate this high-dimensional integral, it was solved using the Monte Carlo integration technique. The Monte Carlo integration makes very few assumptions about the integrand and does not require it to be analytic or continuous. It evaluates the integrand at random sample points and estimates the integral based on that. Since the accuracy increases only as the square root of the number of integration points used, a large number of points are required to achieve a modest accuracy.

Simple Monte Carlo integration uses uniform sampling. It is efficient and converges fast only when the integrand does not vary much. When the integrand has sharp peaks, most points sampled contribute almost nothing and are wasted. The simple Monte Carlo integration technique is improved to handle the sharp peaks by using nonuniform sampling. In this method, sampling points are chosen in such a manner that they are more concentrated where the integrand is peaked. This method is commonly known as the importance sampling method [85]. The integral is rewritten in a way such that the points are sampled from a nonuniform probability density (p).

$$I = \int f \, dV = \int \frac{f}{p} \, p \, dV. \tag{A.10}$$

The ideal sampling density is the one that makes f/p a constant, which requires a perfect knowledge of the integrand. Thus, a probability density that closely matches the integrand is used in practice.

Iteration	Result	Weighted average
1	36(20)	36(20)
2	17.0(1.3)	17.1(1.3)
3	16.50(94)	16.71(76)
4	16.97(75)	16.84(53)
5	16.55(84)	16.76(45)
6	16.80(76)	16.77(39)
7	17.01(76)	16.82(34)
8	15.77(76)	16.64(31)
9	16.50(59)	16.61(28)
10	16.35(55)	16.55(25)

Table A.1: VEGAS results for different iterations of the stopping power ($k_BT/\lambda_D \times 10^{-3}$) during the warmup run. Here, $\Gamma = 0.1$, $\beta = 10$, $v = 2.5v_T$ and $\theta = 22.5°$.

VEGAS is an adaptive Monte Carlo integration technique primarily based on importance sampling [86]. It adaptively constructs a separable probability density of the form

$$p \propto h_x(x)h_y(y)h_z(z)... \tag{A.11}$$

At each iteration, VEGAS samples the integrand using the h-functions (starting with a uniform probability density). Along with the estimate for the integral, it also creates a histogram of the integrand. This is then used to define an improved form of the h-functions for the next iteration.

VEGAS is very effective for the integrands that are separable and non-separable integrands with large peaks. However, it is less effective when multiple small peaks are aligned with the diagonals of the integration domain. Recent work [88] fixes this weakness by adding a second adaptive strategy - adaptive stratified sampling. This method divides the integration volume into many subregions, and the integral is evaluated in these subregions separately. It adaptively reduces the overall integration error by concentrating sampling points in the regions where the variance is largest [85].

We use this improved version of VEGAS, provided by Prof. Peter Lepage, as a python module [87]. The module is written in Cython and supports multi-processor evaluation of integrands using MPI. This implementation is as fast as compiled For-

Iteration	Result	Weighted average
1	17.02(54)	17.02(54)
2	17.29(59)	17.14(40)
3	16.85(51)	17.03(32)
4	16.25(44)	16.77(26)
5	16.31(45)	16.66(22)
6	16.97(61)	16.69(21)
7	16.82(52)	16.71(19)
8	16.94(48)	16.75(18)
9	17.10(46)	16.79(17)
10	16.60(42)	16.77(16)

Table A.2: VEGAS results for different iterations of the stopping power ($k_BT/\lambda_D \times 10^{-3}$) during the main run. Here, $\Gamma = 0.1$, $\beta = 10$, $v = 2.5v_T$ and $\theta = 22.5°$.

tran or C. The computational cost of solving the integral comes from computing the particle trajectories at the sampling points. A faster evaluation is achieved by writing the integrand, including the trajectory calculation in Fortran, and compiling it using the f2py package, which is distributed with the Python NumPy library.

Twenty iterations of VEGAS grid adaptation and the integral estimate were made. The first ten iterations are warmup runs that train the VEGAS grid and are discarded. The results of the warmup runs are shown in table A.1. Here, the weight for the weighted average is the inverse of the variance of each iteration. The VEGAS adapts quickly to the integrand taking only two iterations. The final ten iterations are the main run. The results are shown in table A.2. Since it starts on an already trained grid, the results of different iterations are very close and the error is reduced.

BIBLIOGRAPHY

BIBLIOGRAPHY

[1] B. R. Beck, J. Fajans, and J. H. Malmberg, "Measurement of collisional anisotropic temperature relaxation in a strongly magnetized pure electron plasma," *Phys. Rev. Lett.*, vol. 68, pp. 317–320, Jan 1992.

[2] X. L. Zhang, R. S. Fletcher, S. L. Rolston, P. N. Guzdar, and M. Swisdak, "Ultracold plasma expansion in a magnetic field," *Phys. Rev. Lett.*, vol. 100, p. 235002, Jun 2008.

[3] J. Fajans and C. Surko, "Plasma and trap-based techniques for science with antimatter," *Physics of Plasmas*, vol. 27, no. 3, p. 030601, 2020.

[4] H. Thomas, G. E. Morfill, V. Demmel, J. Goree, B. Feuerbacher, and D. Möhlmann, "Plasma crystal: Coulomb crystallization in a dusty plasma," *Phys. Rev. Lett.*, vol. 73, pp. 652–655, Aug 1994.

[5] P. K. Shukla, "A survey of dusty plasma physics," *Physics of Plasmas*, vol. 8, no. 5, pp. 1791–1803, 2001.

[6] A. K. Harding and D. Lai, "Physics of strongly magnetized neutron stars," *Reports on Progress in Physics*, vol. 69, p. 2631, aug 2006.

[7] R. Aymar, P. Barabaschi, and Y. Shimomura, "The ITER design," *Plasma Physics and Controlled Fusion*, vol. 44, pp. 519–565, apr 2002.

[8] J. M. Guthrie and J. L. Roberts, "Finite-amplitude rf heating rates for magnetized electrons in neutral plasma," *Physics of Plasmas*, vol. 28, no. 5, p. 052101, 2021.

[9] E. Thomas, R. L. Merlino, and M. Rosenberg, "Magnetized dusty plasmas: the next frontier for complex plasma research," *Plasma Physics and Controlled Fusion*, vol. 54, p. 124034, nov 2012.

[10] N. Bennett, D. R. Welch, G. Laity, D. V. Rose, and M. E. Cuneo, "Magnetized particle transport in multi-ma accelerators," *Phys. Rev. Accel. Beams*, vol. 24, p. 060401, Jun 2021.

[11] L. I. Men'shikov, "New directions in the theory of electron cooling," *Physics-Uspekhi*, vol. 51, pp. 645–680, jul 2008.

[12] K. K. Khurana, M. G. Kivelson, V. M. Vasyliunas, N. Krupp, J. Woch, A. Lagg, B. H. Mauk, and W. S. Kurth, *The configuration of Jupiter's magnetosphere*, vol. 1, pp. 593–616. 2004.

[13] S. D. Baalrud and J. Daligault, "Transport regimes spanning magnetization-coupling phase space," *Phys. Rev. E*, vol. 96, p. 043202, Oct 2017.

[14] T. C. Killian, S. Kulin, S. D. Bergeson, L. A. Orozco, C. Orzel, and S. L. Rolston, "Creation of an ultracold neutral plasma," *Phys. Rev. Lett.*, vol. 83, pp. 4776–4779, Dec 1999.

[15] T. S. Strickler, T. K. Langin, P. McQuillen, J. Daligault, and T. C. Killian, "Experimental measurement of self-diffusion in a strongly coupled plasma," *Phys. Rev. X*, vol. 6, p. 021021, May 2016.

[16] S. D. Bergeson, A. Denning, M. Lyon, and F. Robicheaux, "Density and temperature scaling of disorder-induced heating in ultracold plasmas," *Phys. Rev. A*, vol. 83, p. 023409, Feb 2011.

[17] M. Lyon and S. D. Bergeson, "The influence of electron screening on disorder-induced heating," *Journal of Physics B: Atomic, Molecular and Optical Physics*, vol. 44, p. 184014, sep 2011.

[18] N. R. Shaffer and S. D. Baalrud, "The barkas effect in plasma transport," *Physics of Plasmas*, vol. 26, no. 3, p. 032110, 2019.

[19] W.-T. Chen, C. Witte, and J. L. Roberts, "Observation of a strong-coupling effect on electron-ion collisions in ultracold plasmas," *Phys. Rev. E*, vol. 96, p. 013203, Jul 2017.

[20] F. Robicheaux and J. D. Hanson, "Simulation of the expansion of an ultracold neutral plasma," *Phys. Rev. Lett.*, vol. 88, p. 055002, Jan 2002.

[21] J.-H. Choi, B. Knuffman, X. H. Zhang, A. P. Povilus, and G. Raithel, "Trapping and evolution dynamics of ultracold two-component plasmas," *Phys. Rev. Lett.*, vol. 100, p. 175002, Apr 2008.

[22] G. Bannasch, J. Castro, P. McQuillen, T. Pohl, and T. C. Killian, "Velocity relaxation in a strongly coupled plasma," *Phys. Rev. Lett.*, vol. 109, p. 185008, Nov 2012.

[23] Y. C. Chen, C. E. Simien, S. Laha, P. Gupta, Y. N. Martinez, P. G. Mickelson, S. B. Nagel, and T. C. Killian, "Electron screening and kinetic-energy oscillations in a strongly coupled plasma," *Phys. Rev. Lett.*, vol. 93, p. 265003, Dec 2004.

[24] G. M. Gorman, M. K. Warrens, S. J. Bradshaw, and T. C. Killian, "Laser-induced-fluorescence imaging of a spin-polarized ultracold neutral plasma in a magnetic field," *Phys. Rev. A*, vol. 105, p. 013108, Jan 2022.

[25] G. M. Gorman, M. K. Warrens, S. J. Bradshaw, and T. C. Killian, "Magnetic confinement of an ultracold neutral plasma," *Phys. Rev. Lett.*, vol. 126, p. 085002, Feb 2021.

[26] R. T. Sprenkle, S. D. Bergeson, L. G. Silvestri, and M. S. Murillo, "Ultracold neutral plasma expansion in a strong uniform magnetic field," *Phys. Rev. E*, vol. 105, p. 045201, Apr 2022.

[27] C. Amole, G. Andresen, M. Ashkezari, M. Baquero-Ruiz, W. Bertsche, P. Bowe, E. Butler, A. Capra, P. Carpenter, C. Cesar, S. Chapman, M. Charlton, A. Deller, S. Eriksson, J. Escallier, J. Fajans, T. Friesen, M. Fujiwara, D. Gill, A. Gutierrez, J. Hangst, W. Hardy, R. Hayano, M. Hayden, A. Humphries, J. Hurt, R. Hydomako, C. Isaac, M. Jenkins, S. Jonsell, L. Jørgensen, S. Kerrigan, L. Kurchaninov, N. Madsen, A. Marone, J. McKenna, S. Menary, P. Nolan, K. Olchanski, A. Olin, B. Parker, A. Povilus, P. Pusa, F. Robicheaux, E. Sarid, D. Seddon, S. Seif El Nasr, D. Silveira, C. So, J. Storey, R. Thompson, J. Thornhill, D. Wells, D. van der Werf, J. Wurtele, and Y. Yamazaki, "The alpha antihydrogen trapping apparatus," *Nuclear Instruments and Methods in Physics Research Section A: Accelerators, Spectrometers, Detectors and Associated Equipment*, vol. 735, pp. 319–340, 2014.

[28] M. Ahmadi, B. X. R. Alves, C. J. Baker, W. Bertsche, E. Butler, A. Capra, C. Carruth, C. L. Cesar, M. Charlton, S. Cohen, R. Collister, S. Eriksson, A. Evans, N. Evetts, J. Fajans, T. Friesen, M. C. Fujiwara, D. R. Gill, A. Gutierrez, J. S. Hangst, W. N. Hardy, M. E. Hayden, C. A. Isaac, A. Ishida, M. A. Johnson, S. A. Jones, S. Jonsell, L. Kurchaninov, N. Madsen, M. Mathers, D. Maxwell, J. T. K. McKenna, S. Menary, J. M. Michan, T. Momose, J. J. Munich, P. Nolan, K. Olchanski, A. Olin, P. Pusa, C. Ø. Rasmussen, F. Robicheaux, R. L. Sacramento, M. Sameed, E. Sarid, D. M. Silveira, S. Stracka, G. Stutter, C. So, T. D. Tharp, J. E. Thompson, R. I. Thompson, D. P. van der Werf, and J. S. Wurtele, "Antihydrogen accumulation for fundamental symmetry tests," *Nature Communications*, vol. 8, p. 681, Sep 2017.

[29] M. Ahmadi, B. X. R. Alves, C. J. Baker, W. Bertsche, A. Capra, C. Carruth, C. L. Cesar, M. Charlton, S. Cohen, R. Collister, S. Eriksson, A. Evans, N. Evetts, J. Fajans, T. Friesen, M. C. Fujiwara, D. R. Gill, J. S. Hangst, W. N. Hardy, M. E. Hayden, C. A. Isaac, M. A. Johnson, S. A. Jones, S. Jonsell, L. Kurchaninov, N. Madsen, M. Mathers, D. Maxwell, J. T. K. McKenna, S. Menary, T. Momose, J. J. Munich, K. Olchanski, A. Olin, P. Pusa, C. O. Rasmussen, F. Robicheaux, R. L. Sacramento, M. Sameed, E. Sarid, D. M. Silveira, C. So, G. Stutter, T. D. Tharp, J. E. Thompson, R. I. Thompson, D. P. van der Werf, and J. S. Wurtele, "Enhanced control and reproducibility of non-neutral plasmas," *Phys. Rev. Lett.*, vol. 120, p. 025001, Jan 2018.

[30] C. J. Baker, W. Bertsche, A. Capra, C. L. Cesar, M. Charlton, A. C. Mathad, S. Eriksson, A. Evans, N. Evetts, S. Fabbri, J. Fajans, T. Friesen, M. C. Fujiwara, P. Grandemange, P. Granum, J. S. Hangst, M. E. Hayden, D. Hodgkinson,

C. A. Isaac, M. A. Johnson, J. M. Jones, S. A. Jones, S. Jonsell, L. Kurchaninov, N. Madsen, D. Maxwell, J. T. K. McKenna, S. Menary, T. Momose, P. Mullan, K. Olchanski, A. Olin, J. Peszka, A. Powell, P. Pusa, C. Ø. Rasmussen, F. Robicheaux, R. L. Sacramento, M. Sameed, E. Sarid, D. M. Silveira, G. Stutter, C. So, T. D. Tharp, R. I. Thompson, D. P. van der Werf, and J. S. Wurtele, "Sympathetic cooling of positrons to cryogenic temperatures for antihydrogen production," *Nature Communications*, vol. 12, p. 6139, Oct 2021.

[31] G. B. Andresen, M. D. Ashkezari, M. Baquero-Ruiz, W. Bertsche, P. D. Bowe, E. Butler, C. L. Cesar, S. Chapman, M. Charlton, A. Deller, and et al., "Trapped antihydrogen," *Nature*, vol. 468, no. 7324, p. 673–676, 2010.

[32] G. Gabrielse, X. Fei, L. A. Orozco, R. L. Tjoelker, J. Haas, H. Kalinowsky, T. A. Trainor, and W. Kells, "Cooling and slowing of trapped antiprotons below 100 mev," *Phys. Rev. Lett.*, vol. 63, pp. 1360–1363, Sep 1989.

[33] W. A. Bertsche, E. Butler, M. Charlton, and N. Madsen, "Physics with antihydrogen," *Journal of Physics B: Atomic, Molecular and Optical Physics*, vol. 48, p. 232001, oct 2015.

[34] J. H. Ferziger and H. G. Kaper, *Mathematical theory of transport processes in gases*. North-Holland, 1972.

[35] T. O'Neil, "Collision operator for a strongly magnetized pure electron plasma," *Physics of Fluids*, vol. 26, no. 8, pp. 2128–2135, 1983.

[36] M. E. Glinsky, T. M. O'Neil, M. N. Rosenbluth, K. Tsuruta, and S. Ichimaru, "Collisional equipartition rate for a magnetized pure electron plasma," *Physics of Fluids B: Plasma Physics*, vol. 4, no. 5, pp. 1156–1166, 1992.

[37] A. Lenard, "On bogoliubov's kinetic equation for a spatially homogeneous plasma," *Annals of Physics*, vol. 10, no. 3, pp. 390–400, 1960.

[38] R. Balescu, "Irreversible processes in ionized gases," *The Physics of Fluids*, vol. 3, no. 1, pp. 52–63, 1960.

[39] N. Rostoker, "Kinetic equation with a constant magnetic field," *Physics of Fluids*, vol. 3, no. 6, pp. 922–927, 1960.

[40] M. N. Rosenbluth, W. M. MacDonald, and D. L. Judd, "Fokker-planck equation for an inverse-square force," *Phys. Rev.*, vol. 107, pp. 1–6, Jul 1957.

[41] S. Cohen, E. Sarid, and M. Gedalin, "Fokker-planck coefficients for a magnetized ion-electron plasma," *Physics of Plasmas*, vol. 25, no. 1, p. 012311, 2018.

[42] S. Cohen, E. Sarid, and M. Gedalin, "Collisional relaxation of a strongly magnetized ion-electron plasma," *Physics of Plasmas*, vol. 26, no. 8, p. 082105, 2019.

[43] C. Dong, W. Zhang, and D. Li, "Fokker-planck equation in the presence of a uniform magnetic field," *Physics of Plasmas*, vol. 23, no. 8, p. 082105, 2016.

[44] A. A. Ware, "Electron fokker-planck equation for collisions with ions in a magnetized plasma," *Phys. Rev. Lett.*, vol. 62, pp. 51–54, Jan 1989.

[45] L. Pitaevskii and E. Lifshitz, *Physical Kinetics*. Butterworth-Heinemann, 2012.

[46] S. Ichimaru and M. N. Rosenbluth, "Relaxation processes in plasmas with magnetic field. temperature relaxations," *The Physics of Fluids*, vol. 13, no. 11, pp. 2778–2789, 1970.

[47] D. Montgomery, G. Joyce, and L. Turner, "Magnetic field dependence of plasma relaxation times," *Physics of Fluids*, vol. 17, no. 12, pp. 2201–2204, 1974.

[48] D. Montgomery, L. Turner, and G. Joyce, "Fokker-planck equation for a plasma in a magnetic field," *Physics of Fluids*, vol. 17, no. 5, pp. 954–960, 1974.

[49] D. H. Dubin, "Parallel velocity diffusion and slowing-down rate from long-range collisions in a magnetized plasma," *Physics of Plasmas*, vol. 21, no. 5, p. 052108, 2014.

[50] H. Nersisyan, C. Toepffer, and G. Zwicknagel, *Interactions between charged particles in a magnetic field*. Springer-Verlag Berlin Heidelberg, 2007.

[51] C. Dong, H. Ren, H. Cai, and D. Li, "Effects of magnetic field on anisotropic temperature relaxation," *Physics of Plasmas*, vol. 20, no. 3, p. 032512, 2013.

[52] C. Dong, H. Ren, H. Cai, and D. Li, "Temperature relaxation in a magnetized plasma," *Physics of Plasmas*, vol. 20, no. 10, p. 102518, 2013.

[53] T. Kihara, "Ion-electron relaxation of plasmas in a strong magnetic field. i," *Journal of the Physical Society of Japan*, vol. 14, no. 12, pp. 1751–1754, 1959.

[54] D. H. E. Dubin, "Test particle diffusion and the failure of integration along unperturbed orbits," *Phys. Rev. Lett.*, vol. 79, pp. 2678–2681, Oct 1997.

[55] H. B. Nersisyan, C. Deutsch, and A. K. Das, "Number-conserving linear-response study of low-velocity ion stopping in a collisional magnetized classical plasma," *Phys. Rev. E*, vol. 83, p. 036403, Mar 2011.

[56] T. Lafleur and S. D. Baalrud, "Transverse force induced by a magnetized wake," *Plasma Physics and Controlled Fusion*, vol. 61, no. 12, p. 125004, 2019.

[57] T. Kihara, Y. Midzuno, K. Sakuma, and T. Shizume, "Ion-electron relaxation of plasmas in a magnetic field, ii.," *Journal of the Physical Society of Japan*, vol. 15, no. 4, pp. 684–687, 1960.

[58] T. Kihara and Y. Midzuno, "Irreversible processes in plasmas in a strong magnetic field," *Rev. Mod. Phys.*, vol. 32, pp. 722–730, Oct 1960.

[59] V. Silin, "On relaxation of electron and ion temperatures of fully ionized plasma in a strong magnetic field," *Sov. Phys. JETP*, vol. 16, no. 5, p. 1281, 1963.

[60] S. D. Baalrud and J. Daligault, "Extending plasma transport theory to strong coupling through the concept of an effective interaction potential," *Physics of Plasmas*, vol. 21, no. 5, p. 055707, 2014.

[61] C. Paquette, C. Pelletier, G. Fontaine, and G. Michaud, "Diffusion Coefficients for Stellar Plasmas," *Astrophys. J. Suppl.*, vol. 61, p. 177, May 1986.

[62] S. A. Khrapak, A. V. Ivlev, G. E. Morfill, and S. K. Zhdanov, "Scattering in the attractive yukawa potential in the limit of strong interaction," *Phys. Rev. Lett.*, vol. 90, p. 225002, Jun 2003.

[63] S. D. Baalrud and J. Daligault, "Effective potential theory for transport coefficients across coupling regimes," *Phys. Rev. Lett.*, vol. 110, p. 235001, Jun 2013.

[64] S. D. Baalrud and J. Daligault, "Mean force kinetic theory: A convergent kinetic theory for weakly and strongly coupled plasmas," *Physics of Plasmas*, vol. 26, no. 8, p. 082106, 2019.

[65] L. G. Stanton and M. S. Murillo, "Ionic transport in high-energy-density matter," *Phys. Rev. E*, vol. 93, p. 043203, Apr 2016.

[66] J. Daligault, K. O. Rasmussen, and S. D. Baalrud, "Determination of the shear viscosity of the one-component plasma," *Phys. Rev. E*, vol. 90, p. 033105, Sep 2014.

[67] N. R. Shaffer, S. D. Baalrud, and J. Daligault, "Effective potential theory for diffusion in binary ionic mixtures," *Phys. Rev. E*, vol. 95, p. 013206, Jan 2017.

[68] B. Scheiner and S. D. Baalrud, "Testing thermal conductivity models with equilibrium molecular dynamics simulations of the one-component plasma," *Phys. Rev. E*, vol. 100, p. 043206, Oct 2019.

[69] J. Daligault, "Liquid-state properties of a one-component plasma," *Phys. Rev. Lett.*, vol. 96, p. 065003, Feb 2006.

[70] L. Jose and S. D. Baalrud, "A generalized boltzmann kinetic theory for strongly magnetized plasmas with application to friction," *Physics of Plasmas*, vol. 27, no. 11, p. 112101, 2020.

[71] L. Jose and S. D. Baalrud, "A kinetic model of friction in strongly coupled strongly magnetized plasmas," *Physics of Plasmas*, vol. 28, no. 7, p. 072107, 2021.

[72] L. Jose, D. J. Bernstein, and S. D. Baalrud, "Barkas effect in strongly magnetized plasmas," *Physics of Plasmas*, vol. 29, no. 11, p. 112103, 2022.

[73] S. Harris, *An introduction to the theory of the Boltzmann equation*. Courier Corporation, 2004.

[74] H. Grad, "Principles of the kinetic theory of gases," in *Thermodynamik der Gase/Thermodynamics of Gases*, pp. 205–294, Springer, 1958.

[75] C. Cercignani, R. Illner, and M. Pulvirenti, *The mathematical theory of dilute gases*, vol. 106. Springer-Verlag New York, 1994.

[76] T. O'Neil and P. Hjorth, "Collisional dynamics of a strongly magnetized pure electron plasma," *Physics of fluids*, vol. 28, no. 11, pp. 3241–3252, 1985.

[77] S. D. Baalrud and J. Daligault, "Effective potential kinetic theory for strongly coupled plasmas," *AIP Conference Proceedings*, vol. 1786, no. 1, p. 130001, 2016.

[78] D. J. Bernstein, T. Lafleur, J. Daligault, and S. D. Baalrud, "Friction force in strongly magnetized plasmas," *Phys. Rev. E*, vol. 102, p. 041201, Oct 2020.

[79] H. B. Nersisyan, M. Walter, and G. Zwicknagel, "Stopping power of ions in a magnetized two-temperature plasma," *Phys. Rev. E*, vol. 61, pp. 7022–7033, Jun 2000.

[80] H. B. Nersisyan, G. Zwicknagel, and C. Toepffer, "Energy loss of ions in a magnetized plasma: Conformity between linear response and binary collision treatments," *Phys. Rev. E*, vol. 67, p. 026411, Feb 2003.

[81] H. B. Nersisyan and G. Zwicknagel, "Binary collisions of charged particles in a magnetic field," *Phys. Rev. E*, vol. 79, p. 066405, Jun 2009.

[82] C. Cereceda, M. de Peretti, and C. Deutsch, "Stopping power for arbitrary angle between test particle velocity and magnetic field," *Physics of plasmas*, vol. 12, no. 2, p. 022102, 2005.

[83] F. Reif, *Fundamentals of statistical and thermal physics*. Waveland Press, 2009.

[84] C. Cercignani and M. Lampis, "On the h-theorem for polyatomic gases," *Journal of Statistical Physics*, vol. 26, no. 4, pp. 795–801, 1981.

[85] W. H. Press, S. A. Teukolsky, W. T. Vetterling, and B. P. Flannery, *Numerical recipes 3rd edition: The art of scientific computing*. Cambridge University Press, 2007.

[86] G. Peter Lepage, "A new algorithm for adaptive multidimensional integration," *Journal of Computational Physics*, vol. 27, no. 2, pp. 192 – 203, 1978.

[87] P. Lepage, "gplepage/vegas: vegas version 3.4.2," Feb. 2020.

[88] G. P. Lepage, "Adaptive multidimensional integration: vegas enhanced," *Journal of Computational Physics*, vol. 439, p. 110386, 2021.

[89] E. Hairer, S. P. Norsett, and G. Wanner, *Runge-Kutta and Extrapolation Methods*, pp. 129–353. Springer Berlin Heidelberg, 1993.

[90] B. D. Fried and S. D. Conte, *The plasma dispersion function: the Hilbert transform of the Gaussian*. Academic Press, 1961.

[91] D. R. Nicholson, *Introduction to plasma theory*. Wiley, 1983.

[92] S. Ichimaru, *Statistical Plasma Physics, Volume I: Basic Principles*. CRC Press, 2004.

[93] D. J. Bernstein, S. D. Baalrud, and J. Daligault, "Effects of coulomb coupling on stopping power and a link to macroscopic transport," *Physics of Plasmas*, vol. 26, no. 8, p. 082705, 2019.

[94] P. E. Grabowski, M. P. Surh, D. F. Richards, F. R. Graziani, and M. S. Murillo, "Molecular dynamics simulations of classical stopping power," *Physical review letters*, vol. 111, no. 21, p. 215002, 2013.

[95] D. J. Bernstein and S. D. Baalrud, "Effects of coulomb coupling on friction in strongly magnetized plasmas," *Physics of Plasmas*, vol. 28, no. 6, p. 062101, 2021.

[96] J. P. Hansen and I. R. McDonald, *Theory of simple liquids: with applications to soft matter*. Academic Press, 2013.

[97] S. D. Baalrud and J. Daligault, "Modified enskog kinetic theory for strongly coupled plasmas," *Phys. Rev. E*, vol. 91, p. 063107, Jun 2015.

[98] T. Lafleur and S. D. Baalrud, "Friction in a strongly magnetized neutral plasma," *Plasma Physics and Controlled Fusion*, vol. 62, p. 095003, jul 2020.

[99] K. R. Vidal and S. D. Baalrud, "Extended space and time correlations in strongly magnetized plasmas," *Physics of Plasmas*, vol. 28, no. 4, p. 042103, 2021.

[100] L. Spitzer, *Physics of fully ionized gases*. John Wiley and Sons, 1956.

[101] W. H. Barkas, J. N. Dyer, and H. H. Heckman, "Resolution of the Σ^--mass anomaly," *Phys. Rev. Lett.*, vol. 11, pp. 26–28, Jul 1963.

[102] J. Ashley, R. Ritchie, and W. Brandt, "Z 1 3 effect in the stopping power of matter for charged particles," *Physical Review B*, vol. 5, no. 7, p. 2393, 1972.

[103] J. Jackson and R. McCarthy, "z 3 corrections to energy loss and range," *Physical Review B*, vol. 6, no. 11, p. 4131, 1972.

[104] J. Lindhard, "The barkas effect-or z13, z14-corrections to stopping of swift charged particles," *Nuclear Instruments and Methods*, vol. 132, pp. 1–5, 1976.

[105] G. Zwicknagel, "Nonlinear energy loss of heavy ions in plasma," *Nuclear Instruments and Methods in Physics Research Section B: Beam Interactions with Materials and Atoms*, vol. 197, no. 1, pp. 22–38, 2002.

[106] S. D. Baalrud and T. Lafleur, "dc electrical conductivity in strongly magnetized plasmas," *Physics of Plasmas*, vol. 28, no. 10, p. 102107, 2021.

[107] Y. S. Derbenev and A. N. Skrinsky, "The Effect of an Accompanying Magnetic Field on Electron Cooling," *Part. Accel.*, vol. 8, pp. 235–243, 1978.

[108] V. Parkhomchuk, "Study of fast electron cooling," in *Proceedings of the Workshop on Electron Cooling and Related Applications (ECOOL84, 1984)* (H. Poth, ed.), pp. 71–84, Karlsruhe: Kernforschungszentrum Karlsruhe GmbH, 1984.

[109] N. Dikanskii, N. K. Kot, V. Kudelainen, V. Lebedev, and V. Parkhomchuk, "Influence of the sign of the charge of an ion on the friction force in electron cooling," *Zh. Eksp. Teor. Fiz*, vol. 37, pp. 65–73, 1988.

[110] C. Dong, W. Hu, D. Li, and W. Zhang, "Impact of magnetic field on the parallel resistivity," *Phys. Rev. E*, vol. 105, p. 055204, May 2022.

[111] D. J. Bernstein and S. D. Baalrud, "Method to determine the electron–ion temperature relaxation rate from test particle distributions," *Physics of Plasmas*, vol. 29, no. 7, p. 072705, 2022.

[112] S. D. Baalrud and J. Daligault, "Temperature anisotropy relaxation of the one-component plasma," *Contributions to Plasma Physics*, vol. 57, no. 6-7, pp. 238–251, 2017.

[113] T. Ott and M. Bonitz, "Diffusion in a strongly coupled magnetized plasma," *Physical review letters*, vol. 107, no. 13, p. 135003, 2011.

[114] T. Ott, M. Bonitz, P. Hartmann, and Z. Donkó, "Spontaneous generation of temperature anisotropy in a strongly coupled magnetized plasma," *Phys. Rev. E*, vol. 95, p. 013209, Jan 2017.

[115] B. Scheiner and S. D. Baalrud, "Viscosity of the magnetized strongly coupled one-component plasma," *Phys. Rev. E*, vol. 102, p. 063202, Dec 2020.

[116] H. Kählert and M. Bonitz, "Dynamic structure factor of the magnetized one-component plasma: Crossover from weak to strong coupling," *Phys. Rev. Res.*, vol. 4, p. 013197, Mar 2022.